

Air Force Institute of Technology AFIT Scholar

Theses and Dissertations

Student Graduate Works

9-10-2010

Statistical Image Recovery from Laser Speckle Patterns with Polarization Diversity

Donald B. Dixon

Follow this and additional works at: <https://scholar.afit.edu/etd>

Part of the [Applied Statistics Commons](#), and the [Graphics and Human Computer Interfaces Commons](#)

Recommended Citation

Dixon, Donald B., "Statistical Image Recovery from Laser Speckle Patterns with Polarization Diversity" (2010). *Theses and Dissertations*. 1973.
<https://scholar.afit.edu/etd/1973>

This Dissertation is brought to you for free and open access by the Student Graduate Works at AFIT Scholar. It has been accepted for inclusion in Theses and Dissertations by an authorized administrator of AFIT Scholar. For more information, please contact richard.mansfield@afit.edu.



STATISTICAL IMAGE RECOVERY
FROM LASER SPECKLE PATTERNS
WITH POLARIZATION DIVERSITY

DISSERTATION

Donald B. Dixon, Lieutenant Colonel, USAF

AFIT/DEO/ENG/10-11

DEPARTMENT OF THE AIR FORCE
AIR UNIVERSITY

AIR FORCE INSTITUTE OF TECHNOLOGY

Wright-Patterson Air Force Base, Ohio

APPROVED FOR PUBLIC RELEASE; DISTRIBUTION UNLIMITED.

The views expressed in this dissertation are those of the author and do not reflect the official policy or position of the United States Air Force, Department of Defense, or the United States Government. This material is declared a work of the U.S. Government and is not subject to copyright protection in the United States.

AFIT/DEO/ENG/10-11

STATISTICAL IMAGE RECOVERY FROM LASER SPECKLE PATTERNS
WITH POLARIZATION DIVERSITY

DISSERTATION

Presented to the Faculty
Graduate School of Engineering and Management
Air Force Institute of Technology
Air University
Air Education and Training Command
in Partial Fulfillment of the Requirements for the
Degree of Doctor of Philosophy

Donald B. Dixon, B.S.E.E., M.S.E.E.
Lieutenant Colonel, USAF

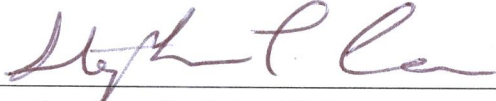
September 2010

APPROVED FOR PUBLIC RELEASE; DISTRIBUTION UNLIMITED.

STATISTICAL IMAGE RECOVERY FROM LASER SPECKLE PATTERNS
WITH POLARIZATION DIVERSITY


Donald B. Dixon, B.S.E.E., M.S.E.E.
Lieutenant Colonel, USAF

Approved:




Stephen C. Cain, PhD
Chairman

17 Aug 2010
Date



Richard K. Martin, PhD
Member


17 Aug 2010
Date



Matthew C. Fickus, PhD
Member

17 Aug 2010
Date

Accepted:



M. U. Thomas
Dean, Graduate School of Engineering and Management

24 Aug 2010
Date

Abstract

This research extends the theory and understanding of the laser speckle imaging technique. This non-traditional imaging technique may be employed to improve space situational awareness and image deep space objects from a ground-based sensor system. The use of this technique is motivated by the ability to overcome aperture size limitations and the distortion effects from Earth's atmosphere.

Laser speckle imaging is a lensless, coherent method for forming two-dimensional images from their autocorrelation functions. Phase retrieval from autocorrelation data is an ill-posed problem where multiple solutions exist. This research introduces polarization diversity as a method for obtaining additional information so the structure of the object being reconstructed can be improved. Results show that in some cases the images restored using polarization diversity are superior to those reconstructed without it.

This research presents statistical analysis of the observed data, two distinct image recovery algorithms, and a Cramer-Rao Lower Bound on resolution. A mathematical proof is provided to demonstrate the statistical properties of the observed, noisy autocorrelation data. The algorithms are constructed using the Expectation-Maximization approach and a polarization parameter that relates two independently observed data channels. The algorithms are validated with computer simulation and laboratory experiment. Comparison is made to an existing phase-retrieval technique. The theoretical lower bound is developed for comparing theoretical performance with and without polarization diversity. The results demonstrate the laser speckle imaging technique is improved with polarization diversity.

For my Lord, my wife and my three children.

Acknowledgements

I would like to thank Dr Steve Cain for all of his help in this research as well as my academic program. He provided a tremendous amount of guidance and mentoring.

Donald B. Dixon

Table of Contents

	Page
Abstract	iv
Acknowledgements	vi
List of Figures	x
List of Symbols	xii
List of Abbreviations	xiv
I. Introduction	1
1.1 Operational Motivation	2
1.2 Technical Motivation	3
1.2.1 Basic Mathematical Model	6
1.2.2 Atmospheric Effects on Laser Speckle Imaging	10
1.3 Research Contributions	15
1.4 Dissertation Overview	15
II. Background	17
2.1 Averaging Laser Speckle Patterns	17
2.2 Object Autocorrelation from Intensity Data	18
2.3 Phase Retrieval	19
2.4 Phase Retrieval Algorithms	19
2.4.1 Gerchberg-Saxton Algorithm	19
2.4.2 Fienup's Algorithms	20
2.4.3 Schulz-Snyder Algorithm	21
2.4.4 Phillips' Algorithm	23
2.5 Additional Image Recovery Efforts	24
2.5.1 Phillips Joint Algorithm	24
2.5.2 Sparse Arrays of Detectors	25
2.5.3 Other Novel Ideas	25
III. Research Foundations	30
3.1 Sensor Model	30
3.1.1 Proposed Sensor Hardware	30
3.1.2 Object Illumination	33
3.2 Mathematical Model	34
3.3 Polarimetric Model	36

	Page	
3.4	Statistical Model	37
3.5	Maximum Likelihood Approach	40
3.6	Expectation-Maximization Approach	42
3.6.1	Expectation Step	45
3.7	Poisson Statistics	47
IV.	Polarimetric Algorithms	49
4.1	Two-Channel Algorithm	49
4.1.1	Incomplete Data Model	49
4.1.2	Complete Data Model	50
4.1.3	Expectation Step	53
4.1.4	Maximization Step	54
4.2	Dual-Channel Algorithm	57
4.2.1	Incomplete Data Model	57
4.2.2	Complete Data Model	57
4.2.3	Expectation Step	59
4.2.4	Maximization Step	60
4.3	Algorithm Computation	63
4.4	Stopping Criteria	64
V.	Cramer-Rao Lower Bound on Spatial Resolution	66
5.1	Object Model	67
5.2	Resolution Criterion	70
5.3	Bound for Single, Unpolarized Channel	70
5.4	Bound for Two-Channel, Polarimetric Estimator	74
5.5	Bound for Dual-Channel, Polarimetric Estimator	80
5.6	Bound Results and Comparison	86
5.6.1	Single-Channel, Unpolarized System	88
5.6.2	Two-Channel, Polarimetric System	90
5.6.3	Dual-Channel, Polarimetric System	92
VI.	Results and Analysis	94
6.1	Simulation Results	94
6.2	Experimental Results	101
VII.	Conclusion	106
7.1	Research Summary	106
7.2	Recommendations for Future Research	109
7.3	Sponsor Acknowledgement	109

	Page
Appendix A. Proof of Equation 2.1	110
Appendix B. Proof of Equation 2.2	115
Appendix C. Proof of Exponential Statistics for the Processed Data .	129
Appendix D. Single Channel, EM Phase Retrieval Algorithm	133
Bibliography	138

List of Figures

Figure		Page
1.1	Diagram of Laser-Speckle Imaging	4
1.2	Diagram of Lensless Laser-Speckle Imaging	4
1.3	Example Imaged and Non-imaged Speckle	5
1.4	Laser Speckle Geometry	6
1.5	Geometry for Propagating Through Turbulence	13
2.1	Block Diagram of Fienup’s Error Reduction Method	21
3.1	Hardware Sub-element for Polarimetric Correlography System .	31
3.2	Alternative Sub-element for Polarimetric Correlography System	32
3.3	Geometry for Considering Spatial Coherence	33
5.1	Two Point Source Object Model Geometry	67
5.2	Resolution Bound vs. Separation for Single Channel Case . . .	89
5.3	Resolution Bound vs. Separation for Various Aperture Sizes . .	90
5.4	Resolution Bound vs. Separation for One and Two Channel Cases	91
5.5	Resolution Bound vs. Separation for Dual Channel with Various Polarization States	92
5.6	Resolution Bound vs. Separation for Two Channel and Dual Channel Cases	93
6.1	Simulated Object Polarization	95
6.2	Example Simulation Data	96
6.3	Error Results for Two Algorithms per Iteration Number	98
6.4	Error Results for Two Algorithms per Frame Number	99
6.5	Error Results for Three Algorithms per Iteration Number . . .	100
6.6	Error Results for Three Algorithms per Frame Number	101
6.7	Diagram of Laboratory Setup	102
6.8	Image of Back Illuminated Bar Target Set	104

Figure		Page
6.9	Recovered Image From Experimental Data; Two-Channel Algorithm, 28 Iterations	105
6.10	Recovered Image From Experimental Data; Single-Channel Algorithm, 28 Iterations	105

List of Symbols

Symbol		Page
S	Oscillator Amplitude	6
ν	Optical Frequency	6
t	Time	6
φ	Laser Phase	6
α_k	Phasor Random Amplitude	7
θ_k	Phasor Random Phase	7
j	Imaginary Unit, $\sqrt{-1}$	7
$f(\mathbf{x})$	Complex Object Field	7
\mathbf{x}	Two Dimensional Coordinate Vector	7
$a(\mathbf{x})$	Object Field Amplitude	7
$\phi(\mathbf{x})$	Phase of Object Field	7
$E[\cdot]$	Expected Value Operator	8
$o(\mathbf{x})$	Incoherent Object Intensity Function	8
$\delta(\mathbf{x})$	Dirac's Delta Function	8
z	Perpendicular Propagation Distance	9
$\mathcal{F}^{\lambda z}$	2-D Scaled Fourier Transform (Fraunhofer propagation)	9
$R_f(\mathbf{x}_0)$	Field Autocorrelation	9
$I_o(\mathbf{u})$	Observed, Speckled Intensity	9
$n(\mathbf{u})$	Photon Noise	10
$A(\mathbf{u})$	Aperture Function	10
$\psi(\mathbf{u})$	Phase Aberration From Atmosphere	11
$\chi(\mathbf{x}, \mathbf{u})$	Propagation Distance (as a function of spatial position)	13
C	Ensemble Average of Nonimaged Laser Speckle	17
K	Number of Independent Speckle Realizations	18
$R_o(\mathbf{x})$	Autocorrelation of Object Intensity	18

Symbol		Page
$ h(\mathbf{x}) ^2$	Incoherent, Intensity Impulse Response	18
$d_k(\mathbf{x})$	Noisy Object Autocorrelation Data	34
$\tilde{R}_o(\mathbf{x})$	Measured Autocorrelation	35
p	Polarization Ratio	36
T	Finite Integration Time	38
R_o	Expected Value of Exponential Distribution	40
L	Log-Likelihood Function	41
$D(\mathbf{x})$	Average of Observed Data	41
L_{CD}	Complete Data Log Likelihood Function	44
Q	Q-Function	45
μ	Conditional Expectation of Complete Data	45
β	Dampening Parameter	64
Δ	Separation Distance	67
J	Fisher Information Matrix	71

List of Abbreviations

Abbreviation		Page
LADAR	Laser Detection and Ranging	1
SSA	Space Situational Awareness	2
FFT	Fast Fourier Transform	25
EM	Expectation-Maximization	28
ML	Maximum Likelihood	30
PBS	Polarizing Beam Splitter	31
APD	Avalanche Photodiode	31
GHz	Gigahertz	33
DFT	Digital Fourier Transform	34
SNR	Signal-to-Noise Ratio	39
pdf	Probability Density Function	40
RL	Richardson-Lucy	41
DLR	Dempster, Laird and Rubin	42
pmf	Probability Mass Function	46
MAP	maximum a posteriori	49
E-Step	Expectation Step	53
M-Step	Maximization Step	54
CRLB	Cramer-Rao Lower Bound	66
PSF	Point Spread Function	67
FI	Fisher Information	68
rect	Rectangular Function	68
MSE	Mean-Squared Error	96
CCD	Charge-Coupled Device	101
CW	Continuous Wave	102
μm	micrometer	102
nm	nanometer	102

STATISTICAL IMAGE RECOVERY FROM LASER SPECKLE PATTERNS WITH POLARIZATION DIVERSITY

I. Introduction

Synthetic aperture Laser Detection and Ranging (LADAR) imaging is investigated in this research. This research provides an improved phase retrieval algorithm for recovering remotely sensed objects from non-imaged, laser-speckle, intensity data. The innovative aspects investigated as part of this effort include the addition of polarization diversity and a statistical approach to object recovery that improves upon existing techniques. Improvement is demonstrated via computer simulation, laboratory experiment, and a theoretical bound on resolution. This work is a continuation of previous research efforts [3, 31–33].

Fundamentally, the Department of Defense desires cost savings and improved image resolution beyond what can be achieved with existing optical reconnaissance systems. In general, with larger apertures, greater diffraction-limited, resolution is achieved. There are applications, such as space-borne sensors, where optical imaging is preferred; however, the size of the optic is limited by weight and cost constraints. Practically, for a satellite system, weight and cost savings can be achieved at the expense of power and computer processing. Weight and cost savings can potentially be achieved with large, synthetic apertures without a focusing lens. Large, synthetic apertures designed with many light-weight and relatively inexpensive detector elements save production expense and weight compared with large, monolithic optical elements found in traditional optical systems. Ideally, an even larger overall aperture can be synthesized with many small elements as compared to a cost equivalent optical system.

Along with cost savings, the goal is to improve upon available image resolution and overcome detection and atmospheric noise. For ground-based sensors looking skyward, large optical systems are developed; however, the Earth's atmosphere severely limits performance. It will be shown in this dissertation that laser speckle imaging without optics in ground systems avoids the effect of imaging through atmospheric turbulence at the aperture. Turbulence effects are not observed because the perturbed phase information is completely destroyed in the collection process [3, 44]. Only scintillation effects due to layered atmosphere above the aperture plane need be considered [44]. However, without the object phase information we must estimate the phase leading to the classical phase retrieval problem discussed later in this document.

This chapter introduces the dissertation research and its documentation. The operational motivation for conducting the research is first provided in Section 1.1. Technical motivation for this research is provided in Section 1.2. This is followed by a summary of Research Contributions in Section 1.3. The chapter concludes with a Dissertation Overview in Section 1.4.

1.1 Operational Motivation

Accurate and reliable Space Situational Awareness (SSA) is an important requirement for the United States Air Force. General C. Robert Kehler, Commander, Air Force Space Command, in a speech to the Air Force Association in November 2007 said,

“...a critical important thing for us and that is to get better at space situational awareness. That's one of our top priorities in the command. It's going to remain one of our top priorities on my watch. And leaders flat simply have got to get better about knowing what's up there, tracking what's up there, understanding the intent of things that are up there, and knowing those pieces in real time.” [27]

The space environment continues to be more complex due to increased on-orbit systems as well as debris. The United States must monitor all on-orbit systems and debris for safeguarding and positive control. The SSA mission demands timely knowledge

of debris and orbiting systems over a vast region of space. SSA dictates highly sensitive systems track small objects at high orbit round the clock. With ground based systems, large telescopes are often limited by weather and atmospheric conditions. The fielding of large optical systems with sensitive pointing control mechanisms are extremely costly. It would be beneficial to augment existing assets with less expensive apertures that provide equivalent or better resolution. If less expensive systems could be fielded, additional coverage and surveillance capability can be deployed with limited defense budgets.

In addition to SSA, persistent surveillance from space continues to be an emerging area of need. A broad range of military and non-military applications dictate persistent, on-going image collection with large service times. Atmospheric turbulence is not a limiting factor for space-borne sensors. However, aperture size and service time limit capability. Applications ranging from reconnaissance to geological, environmental, and agricultural surveys require persistent coverage. Improvement in satellite imagery resolution is demanded and this could theoretically be achieved at higher orbits to include geostationary orbit. It is proposed that large, light-weight, synthetic apertures hosted on multiple micro-satellites can bring about improved resolution at higher orbits with less cost and launch weight. Because of these proposals, laser speckle non-optical imaging is revisited for this research. The next section provides an technical overview of speckle formation with an idealized scenario.

1.2 Technical Motivation

The following idealized scenario is considered: A monochromatic laser uniformly illuminates a distant object producing a reflected field at the observation plane. The illuminating field is assumed to be either constant or Gaussian in amplitude and may be perturbed and attenuated by propagation effects. The reflected field is observed with either a lens system (Fig. 1.1) or a detector array without a focusing lens (Fig. 1.2). The technique of detecting the reflected laser light with a detector array without a lens has been referred to by several names throughout the literature. It

has been described as pupil plane imaging, lensless coherent imaging, non-imaged laser-speckle, and image correlography. The last term refers to the correlogram (or object autocorrelation) that can be formed from the speckle pattern [44].

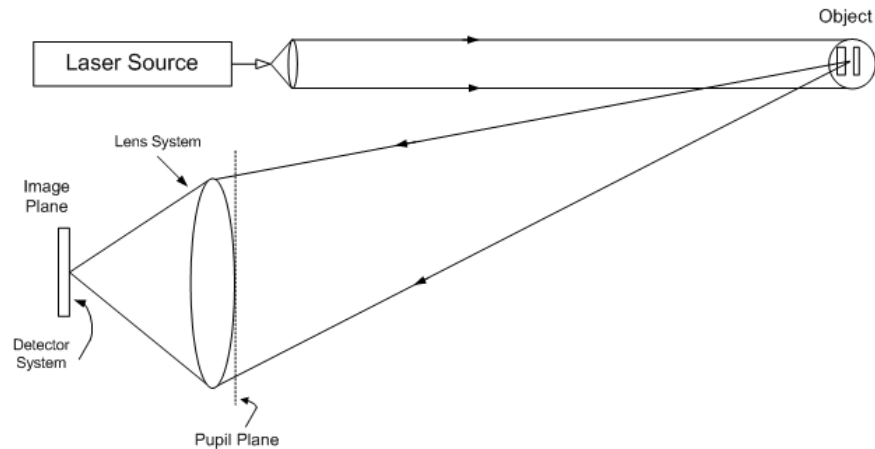


Figure 1.1: Diagram of Laser-Speckle Imaging

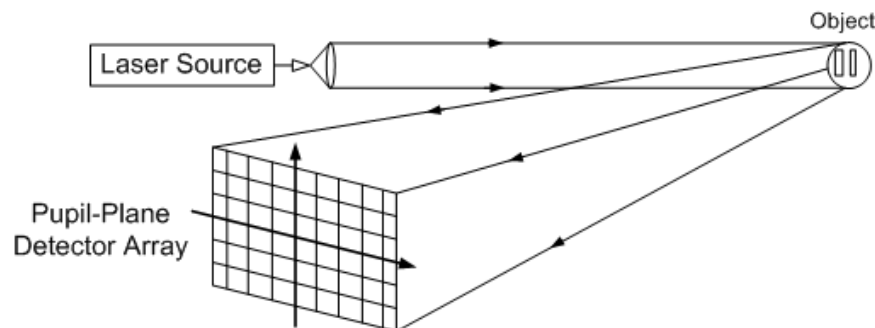


Figure 1.2: Diagram of Lensless Laser-Speckle Imaging [44]

This scenario involves illumination with a coherent source. The reflected laser light, when observed, produces a high-contrast, granular, “speckle” pattern directly related to the roughness of the object surface. Speckle formation is observed in many applications to include synthetic-aperture radar, ultrasound medical imaging, and coherent, visible light imaging [19]. Figure 1.3 demonstrates an example speckled image (A) and an example non-imaged, laser speckle pattern (B). The observed speckle intensity pattern is different for observations with lens and lensless systems. The laser speckle observed by a lens system is essentially a noisy, grainy image as demonstrated

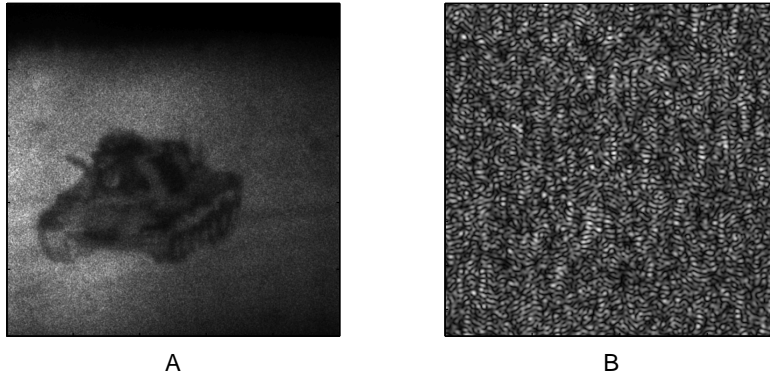


Figure 1.3: Example Speckle: [A] Image Formed with Coherent Illumination, [B] Non-imaged Laser Speckle Pattern

by Fig. 1.3A. However, the laser speckle pattern produced by a lensless system has no visible connection to the object and just appears as a random pattern as demonstrated by Fig. 1.3B. This random pattern, while not an image of the original object, does contain information about the object embedded in the statistical nature of the speckle pattern. This speckle effect is not observed when the illumination source is incoherent. With incoherent illumination, speckle is not observed because the very nature of incoherent light removes the constructive and destructive interference effects. Often, speckle is a nuisance and must be suppressed or removed; however, this research further investigates the use of laser speckle patterns for object recovery in LADAR remote sensing applications.

In this research, we consider the coherent illumination and free-space propagation geometry depicted in Fig. 1.4. The lensless detector array is placed at the observation plane (or pupil plane). The observed speckle pattern occurs when the reflecting surface roughness is on the order of the illuminating wavelength. We can consider the *Huygens-Fresnel principle* to explain this phenomenon. Every point on the reflecting surface is a unique point source contributing to or interfering with the overall wavefront. Due to the relative reflectivity and path differences, each reflecting point source produces random, additive phase contributions to the reflected wavefront. These random contributions serve to create constructive and destructive

interference leading to the observed speckle pattern. The statistical properties of the speckle depend upon the coherence of the illuminating light and the random properties of the surface and transmission medium [6]. Therefore, the observed intensity of the reflected field is directly related to the reflecting object.

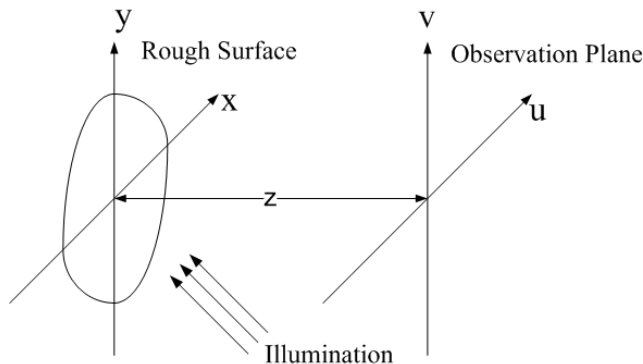


Figure 1.4: Laser Speckle Geometry [16]

A primary technical motivation for considering the correlography technique is the ability to collect object information without the blurring effects of the atmosphere. This will be further discussed in Section 1.2.2. Next we detail the mathematical model under consideration for the idealized scenario.

1.2.1 Basic Mathematical Model. The electric field at the object is excited by an ideal, single-mode laser with a purely monochromatic oscillator with known amplitude S , known frequency ν , time t , and unknown but absolute phase φ . We will assume the laser beam is linearly polarized. This single-mode laser light scenario, detailed by Goodman [17], is modeled as a random process that is both stationary and ergodic. The signal in this ideal scenario is represented by

$$u(t) = S \cos[2\pi\nu t - \varphi]. \quad (1.1)$$

The starting point with this simple model assumes a constant amplitude during the duration of the pulse and a constant phase associated with a sufficiently long coherence time of the laser.

Using scalar theory and complex notation, we consider random contributions from a large number, N , of independent scattering sources. Specifically, at a point on the observation plane, the complex field is the result of a random phasor sum. The mathematics of the random phasor sum found in optics is covered extensively by Goodman [17]. Equation 1.2 describes the random phasor sum where α_k is the random amplitude and θ_k is the random phase of the k th phasor:

$$ae^{j\phi} = \frac{1}{\sqrt{N}} \sum_{k=1}^N \alpha_k e^{j\theta_k}. \quad (1.2)$$

The monochromatic illumination produces a field distribution dependent upon the laser beam distribution and object reflectivity. The reflected object field, $f(\mathbf{x})$, at the object plane is described with complex notation as:

$$f(\mathbf{x}, t) = a(\mathbf{x}, t) \cdot e^{j\phi(\mathbf{x})}, \quad (1.3)$$

where $\mathbf{x} = (x, y)$ is a two dimensional coordinate vector in the object plane, $a(\mathbf{x})$ is the object field amplitude related to the object surface reflectivity, and $\phi(\mathbf{x})$ is the phase directly related to the object surface height profile. Because of object surface roughness, the reflected phase is modeled as uniformly distributed, $\sim U[-\pi, \pi]$; $\phi(\mathbf{x}_1)$ and $\phi(\mathbf{x}_2)$ are independent. This produces a random phasor sum at the detector plane [17,19]. For the proposed LADAR system, it is assumed the reflected laser pulse is integrated (summed) at the detector system for the entire pulse width. Possible pulse width changes and effects due to oblique reflection angles are ignored.

If slight changes to the geometry and environment for each laser pulse are considered, the object field $f(\mathbf{x}, t)$ becomes a random process. The illuminating laser may move slightly, the atmosphere may change the illuminating laser light propagation from pulse to pulse, and the object may move slightly. Slight geometry and environment changes produce a unique reflected field for each laser pulse. Therefore,

the reflected field can be described in statistical terms. Eqn. 1.4 demonstrates the expected value of the reflected field is zero, where $E[\cdot]$ is the Expected Value operator.

$$\begin{aligned}
E[f(\mathbf{x}, t)] &= E[a(\mathbf{x}, t)e^{j\phi(\mathbf{x})}] \\
&= a(\mathbf{x}, t) \cdot E[e^{j\phi(\mathbf{x})}] \\
&= a(\mathbf{x}, t) \cdot \int_{-\pi}^{\pi} \frac{1}{2\pi} [\cos \phi(\mathbf{x}) + j \sin \phi(\mathbf{x})] d\phi \\
&= a(\mathbf{x}, t) \cdot 0 \\
&= 0
\end{aligned} \tag{1.4}$$

The autocorrelation of the object field is detailed in Eqn. 1.5 where $a^2(\mathbf{x}) = o(\mathbf{x})$ is the incoherent object intensity or brightness function and $\delta(\mathbf{x})$ is Dirac's delta function. The expected value operator in Eqn. 1.5 is zero everywhere except when $\phi(\mathbf{x}_1) = \phi(\mathbf{x}_2)$ because statistical independence in the phase at each spatial point on the object surface is assumed. The reflected field is described as a circular Gaussian process which provides some unique properties when studying the laser speckle patterns in the observation plane.

$$\begin{aligned}
E[f(\mathbf{x}_1, t)f^*(\mathbf{x}_2, t)] &= E[a(\mathbf{x}_1, t)e^{j\phi(\mathbf{x}_1)}a(\mathbf{x}_2, t)e^{-j\phi(\mathbf{x}_2)}] \\
&= a(\mathbf{x}_1, t)a(\mathbf{x}_2, t) \cdot E[e^{j\phi(\mathbf{x}_1)}e^{-j\phi(\mathbf{x}_2)}] \\
&= a(\mathbf{x}_1, t)a(\mathbf{x}_2, t) \cdot \delta(\mathbf{x}_1 - \mathbf{x}_2) \\
&= o(\mathbf{x}_1) \cdot \delta(\mathbf{x}_1 - \mathbf{x}_2)
\end{aligned} \tag{1.5}$$

The reflected field at the observation plane, $F(u, v)$, in the far field or Fraunhofer region is related to the object field by the scaled Fourier Transform [18]. This is described in Eqn. 1.6 where $k = 2\pi/\lambda$ is the wave number, λ represents the optical

wavelength of the monochromatic laser and z represents the propagation distance between the object and the observation plane.

$$F(u, v) = \frac{e^{jkz} e^{j\frac{k}{2z}(u^2+v^2)}}{j\lambda z} \int_{-\infty}^{\infty} \int_{-\infty}^{\infty} f(x, y) \exp\{-j\frac{2\pi}{\lambda z}(xu + yv)\} dx dy \quad (1.6)$$

At optical wavelengths the electric field cannot be observed directly; however, the optical power or intensity can be measured via optical detectors. Following Goodman's framework, the intensity is defined as the squared modulus of the analytic signal representation of the field [17, 18]. The intensity at the observation plane is described by

$$I(\mathbf{u}) = |\mathcal{F}^{\lambda z}\{f(\mathbf{x})\}|^2 \quad (1.7)$$

where $\mathcal{F}^{\lambda z}$ is the two-dimensional, scaled Fourier Transform detailed in Eqn. 1.6. $I(\mathbf{u})$ is corrupted by speckle noise due to the random phasor sum produced by the object surface roughness. Note that Eqn. 1.7 describes the modulus squared of the Fourier Transform of the field distribution which is related to the field autocorrelation, $R_f(\mathbf{x}_0)$, via the Fourier Transform due to the Autocorrelation Theorem [18]:

$$|\mathcal{F}\{f(\mathbf{x})\}|^2 = \mathcal{F}\{R_f(\mathbf{x}_0)\}. \quad (1.8)$$

Unfortunately, the complete spectrum cannot be observed due to noise and the finite extent of our detection systems. The observed, speckled intensity data, $I_o(\mathbf{u})$, is modeled as

$$I_o(\mathbf{u}) = [I(\mathbf{u}) + n(\mathbf{u})] \cdot A(\mathbf{u}) \quad (1.9)$$

where $n(\mathbf{u})$, photon or shot noise, is a zero mean noise such that the observed intensity (conditioned on the average photon values) has a Poisson distribution with a mean equal to the intensity without photon noise. This noise is introduced by the random arrival time of the photons emerging from the electric field onto the detector. The mean intensity, observed in photon counts, is itself a random process with an exponential distribution [17]. $A(\mathbf{u})$ is the aperture function denoting the region where the speckle pattern is physically recorded; $A(\mathbf{u}) = 1$ for the points within the measurement aperture and $A(\mathbf{u}) = 0$ elsewhere. Without a traditional lens aperture, the detector array is itself the limiting aperture capturing a finite portion of the reflected field. For systems designed to recover an image of the original object from the observed laser speckle, it is important the laser speckle images are statistically independent. Practically, this condition is easily achieved.

To complete the description of the idealized scenario, a few additional assumptions and limitations must be explored. This non-imaged laser speckle scenario can be considered without atmospheric disturbance or where the atmospheric turbulence is modeled as a phase screen directly over the remote object. Each pupil plane detector observes a beam limited scenario with the array producing a single laser speckle image per pulse. This non-imaged pupil plane intensity is observed over a large number of laser pulses. The observation period for each laser pulse is assumed to be within the coherence time of the laser. In addition, background light is assumed to be completely filtered out and only the reflected laser light is observed. The detector array is sufficiently in the far-field for the Fraunhofer approximation to hold. The pupil plane array is considered perpendicular to the object plane. The pupil plane and the object is fixed during the observation period with sufficiently minor changes pulse to pulse to create statistically independent laser speckle patterns.

1.2.2 Atmospheric Effects on Laser Speckle Imaging. Imaging and optical propagation through turbulent medium has been extensively studied [1, 35]. Atmospheric turbulence effects on laser speckle imaging or imaging correlography are

briefly reviewed here. As previously stated, a single layer of atmospheric turbulence encountered at the observation plane has little effect on non-imaged laser speckle, only layered atmosphere need be considered. Also, a thin layer of atmosphere at the object plane has little effect on nonimaged, speckle intensity measurements. This is explored mathematically along with an extended, thick atmosphere.

1.2.2.1 An Atmospheric Layer at the Observation Plane. If the scenario of a mountaintop observation system looking skyward at zenith is considered, a single, thin layer of atmosphere at the pupil plane is a reasonable and often used model [1]. For mathematical and experimental convenience, extensive research has been detailed on how to analytically replace a turbulent region with an equivalent thin, random screen [35]. For a satellite at geostationary orbit, the ratio of the turbulent layer thickness to the overall propagation distance is very small. For this case, the turbulent layer is considered a “thin” phase screen. In this model, only the phase of the optical wave is distorted by the turbulent region and not the amplitude [1]. Amplitude effects are predominantly observed from propagation distance. For this scenario, phase aberration effects are modeled as a single additive phase parameter, $\psi(\mathbf{u})$. The phase aberrated field, $G(\mathbf{u})$ at the observation plane is described as

$$G(\mathbf{u}) = F(\mathbf{u})e^{j\psi(\mathbf{u})}, \quad (1.10)$$

where $F(\mathbf{u})$ is the reflected field after Fraunhofer propagation. The intensity (without noise) is

$$\begin{aligned} I(\mathbf{u}) &= |G(\mathbf{u})|^2 \\ &= |F(\mathbf{u})e^{j\psi(\mathbf{u})}|^2 \\ &= |F(\mathbf{u})|^2 \cdot e^{j\psi(\mathbf{u})} \cdot e^{-j\psi(\mathbf{u})} \\ &= |F(\mathbf{u})|^2. \end{aligned} \quad (1.11)$$

In simple terms, Eqn. 1.11 describes why the phase aberration due to atmospheric turbulence at the observation plane has no effect on the observed intensity. Speckle noise, detector array effects, system noise, and scintillation due to layered atmosphere are not overcome in a single laser speckle observation.

1.2.2.2 An Atmospheric Layer at the Object Plane. Consider the scenario of a satellite-based sensing system observing the Earth's surface. In this case, a single thin layer of atmosphere at the object plane is a simplified, yet realistic model. This is the same model as the previous section; however, the sensing system and the remote target are reversed. Again, the relatively lengthy propagation distance above the atmosphere as compared to the short propagation distance through the atmosphere is encountered. Much of the atmospheric turbulence effects is due to the dense atmosphere close to the Earth's surface. In considering the Earth's atmosphere as a thin phase screen at the object plane, the phase aberrated field is denoted by $g(\mathbf{x})$.

$$\begin{aligned}
 g(\mathbf{x}) &= f(\mathbf{x})e^{j\psi(\mathbf{x})} \\
 &= a(\mathbf{x})e^{j\phi(\mathbf{x})}e^{j\psi(\mathbf{x})} \\
 &= a(\mathbf{x})e^{j(\phi+\psi)(\mathbf{x})} \\
 &= a(\mathbf{x})e^{j\phi'(\mathbf{x})}
 \end{aligned} \tag{1.12}$$

From Eqn. 1.12 the additive phase aberration only adds another random number to the random phase of the object field, $f(\mathbf{x})$, due to the rough object surface. The object phase is a random variable uniformly distributed between $[-\pi, \pi]$. Adding a zero mean, random number to a uniformly distributed random number, $\{\phi \in [-\pi, \pi]\}$, yields another uniformly distributed number $\phi \in [-\pi, \pi]$ due to phase wrapping. Therefore, the result is identical to the case without atmosphere.

1.2.2.3 *An Extended Atmosphere.* Rayleigh-Sommerfeld Propagation theory [18] is used to address the more complicated extended atmosphere scenario. The geometry for this propagation is depicted in Fig. 1.5. The Rayleigh-Sommerfeld diffraction equation is:

$$F(\mathbf{u}) = \frac{1}{j\lambda} \int_{\Sigma} \frac{f(\mathbf{x})}{\chi(\mathbf{x}, \mathbf{u})} \exp\left(\frac{-j2\pi\chi(\mathbf{x}, \mathbf{u})}{\lambda}\right) \Upsilon d\mathbf{x}. \quad (1.13)$$

Here, $\chi(\mathbf{x}, \mathbf{u})$ is the propagation distance between any two points on the object and observation planes, Σ is the finite object plane, spatial area (or aperture in diffraction theory terms) and Υ is the obliquity factor. Υ goes to unity as the geometry angles are small or the observing plane is far from the diffracting aperture. The primary emphasis for exploring Rayleigh-Sommerfeld, Eqn. 1.13 does not have the simplifying assumptions of the Fraunhofer propagation.

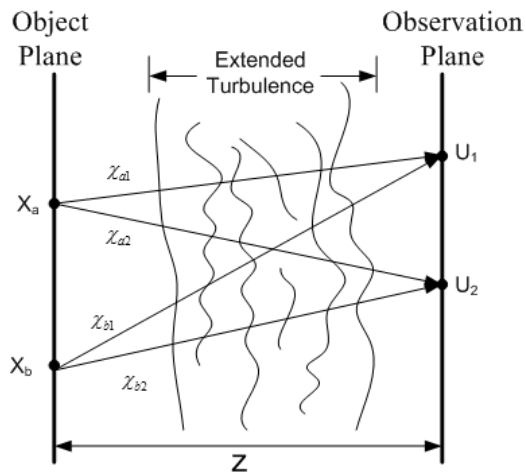


Figure 1.5: Geometry for Propagating Through Turbulence

Treating each point on the object plane as an individual point source emitting an optical wave, the wavefront undergoes a propagation path length, $\chi(\mathbf{x}, \mathbf{u})$ dependent upon spatial position in both the object and observation planes. $\chi(\mathbf{x}, \mathbf{u})$ is calculated according to:

$$\chi(x, y, u, v) = \sqrt{z^2 + (x - u)^2 + (y - v)^2}. \quad (1.14)$$

Note when z is large (the Fraunhofer region) and two simplifying approximation are made, the Rayleigh-Sommerfeld diffraction equation simplifies to the Fraunhofer propagation model [18]. These are (1) $\chi \approx z$ for the term not found in the exponent and (2) for the χ found in the exponent, the binomial expansion to Eqn. 1.14 is approximated with only the first two terms. Returning to Rayleigh-Sommerfeld propagation, the atmospheric effects on the propagation path, $\chi(\mathbf{x}, \mathbf{u})$, must be included.

The extended atmospheric turbulence produces rapid and random changes in the refractive index [1]. Using the first order, Rytov approximation (and weak fluctuation conditions), the turbulence produces a complex phase perturbation on the optical wave [1]. This effectively delays propagation or produces phase aberrations for the propagating wavefront. The phase aberration, $\psi(\mathbf{x}, \mathbf{u}, z)$, essentially changes the path length by the relationship

$$\psi(\mathbf{x}, \mathbf{u}, z) = \frac{\nu\chi_{\Delta}(\mathbf{x}, \mathbf{u})}{c(\mathbf{x}, \mathbf{u}, z)} \quad (1.15)$$

where ν is the frequency of the light, c is the speed of light for a given refractive index, and χ_{Δ} is the change in path length. Adding the path length change due to the phase aberration to Eqn. 1.13 yields Eqn. 1.16.

$$F(\mathbf{u}) = \frac{1}{j\lambda} \int_{\Sigma} \frac{f(\mathbf{x})}{(\chi(\mathbf{x}, \mathbf{u}) + \chi_{\Delta}(\mathbf{x}, \mathbf{u}))} \exp\left(\frac{-j2\pi(\chi(\mathbf{x}, \mathbf{u}) + \chi_{\Delta}(\mathbf{x}, \mathbf{u}))}{\lambda}\right) d\mathbf{x} \quad (1.16)$$

The path length change, due to the phase aberration caused by turbulence, is a function of both object plane and observation plane coordinates. The random perturbations cause path dependent changes to the optical wavefront. From this it is reasoned, Eqn. 1.16 can not be simplified to a scaled Fourier Transform. The layered atmosphere causing scintillation is a much more difficult problem. Propagation through extended turbulence corrupts the Fourier magnitude of the object field. Extended atmosphere and scintillation effects on laser correlography were explored analytically and exper-

imentally by Elbaum *et al.* [10]. The authors concluded under certain conditions the random apodization effect will be negligibly small for a ground-based receiver observing a near-zenith exoatmospheric target. This research will only consider the simple, atmospheric model of a thin phase screen either at the object or observation planes. Although previous researchers in this area acknowledge effects due to high altitude turbulence and scintillation, a thin atmosphere or screen is often assumed for simplification or implied with the data model [11, 23, 25, 39, 44]. The thin screen assumption is continued throughout this dissertation.

1.3 Research Contributions

This dissertation provides three primary research contributions:

- *Statistical Analysis of Correlography Data.* The observed laser speckle is transformed via a post-processing technique that produces noisy autocorrelations. The randomness of the transformed data can be closely modeled by the negative exponential distribution.
- *Two Iterative Algorithms Using Polarimetric Data.* Iterative solutions for maximum likelihood and maximum a posteriori estimators are developed using the Expectation Maximization technique.
- *A Theoretical Bound on Resolution for Correlography.* A Cramer-Rao Lower Bound for resolving two closely spaced point sources is presented using the negative exponential noise model and polarimetric data models.

1.4 Dissertation Overview

This document is divided into seven chapters and contains three appendices. Chapter 2 presents relevant technical background information as the theoretical basis for this research. Previous research in phase retrieval and non-imaging laser speckle is highlighted.

Chapter 3 provides the relevant mathematical models and theory that form a foundation for this research. Although most of this material may be found elsewhere, it provides foundational elements behind the later chapters to include proposed sensor models and statistical framework.

Chapter 4 provides new theoretical work associated with computational algorithms for solving the phase retrieval problem using polarization diversity. Two polarimetric algorithms are presented differentiated by data collection schemes.

Chapter 5 details a theoretical resolution bound for correlography using polarization diversity. The bound itself is not predictive of specific algorithm performance; however, it demonstrates theoretical improvement provided by adding polarization diversity. A Cramer-Rao Lower Bound is presented for both unpolarized and polarized data scenarios. The comparison of theoretical bounds demonstrates relative improvement provided by polarization diversity.

Chapter 6 presents results and analysis from computer simulation and laboratory experiments. A representative subset of simulation and experimental results are presented to support key research findings and contributions. This chapter provides comparative results between polarimetric and non-polarimetric algorithms.

Chapter 7 concludes the main document by providing an overall summary of research activities, a summary of key findings, and recommendations for subsequent research. This is followed by the appendices that provide some of the detailed mathematical proofs.

II. Background

This chapter describes the theoretical background and previous research work for object recovery from laser speckle images. The ultimate goal of object recovery is the synthesis of the best possible object image from a limited data set. With intensity measurements, the phase of the original object field is unknown. In fact, the phase information is lost during the detection process, presenting an ill-posed problem. In the LADAR application considered in this research, an estimate of the object autocorrelation is recorded. The Autocorrelation Theorem relates the autocorrelation to the object's Fourier Magnitude via the Fourier Transform [18]. Unfortunately, complete information about the original object is not observed. However, with iterative computing techniques, it has been shown that an image solution relatively similar the original may be produced. This technique is often described as phase retrieval and is employed in several applications found in image and signal processing. The goal of this research is to provide improvement for this specific phase retrieval problem with laser speckle images.

2.1 Averaging Laser Speckle Patterns

Often with signals corrupted by random noise, the first course of action is to average a large number of independent signal realizations in hopes of minimizing the noise effects. In fact, with laser speckled images (formed with a lens), averaging a large number of registered, independent, speckled images does reduce speckle effects. There are several techniques for speckle suppression in optical imaging [19]. However, averaging nonimaged laser speckle patterns does not yield the same result. The ensemble average of independent, nonimaged laser speckle intensity patterns converges to a constant, C ,

$$\lim_{K \rightarrow \infty} K^{-1} \sum_{k=1}^K I_{o_k}(\mathbf{u}) = C, \quad (\text{a constant}), \quad (2.1)$$

where K is the number of observed frames and I_{o_k} is the k th frame of observed, speckled intensity data. This is proven in Appendix A. Because of this result, we must look to another post processing method to recover the object.

2.2 Object Autocorrelation from Intensity Data

Due to speckle, photon noise, and detector array effects, a single laser speckle image is not useful for object recovery. The random speckle pattern contains statistical information about the object surface, though insufficient for human perception. However, Idell *et al.* pointed out the ensemble average of the magnitude squared of the Fourier transform of the intensity data converges to a result directly related to the object autocorrelation [25]. We will call this operation the Idell function and describe the results in Eqn. 2.2.

$$\lim_{K \rightarrow \infty} K^{-1} \sum_{k=1}^K [|\mathcal{F}^{-1}\{I_{o_k}(\mathbf{u})\}|^2] = b |h(\mathbf{x})|^2 + c [R_o(\mathbf{x})] * |h(\mathbf{x})|^2 \quad (2.2)$$

where b and c are constants, K is the number of independent speckle realizations, $R_o(\mathbf{x})$ is the autocorrelation of the object intensity, $|h(\mathbf{x})|^2$ is the incoherent, intensity impulse response of the detector array and $*$ represents convolution operation. The object autocorrelation is blurred by the impulse response of the detector array in a similar fashion as an optical system blurs an image via diffraction effects. Because of this, the resulting autocorrelation is considered diffraction-limited [13]. The impulse response of the detector array should be known providing the ability to produce a very good estimate of the object autocorrelation. The result in Eqn. 2.2 ignores photon noise added during the detection process. The proof of this result is found in Appendix B.

Through the Wiener-Khinchin Theorem, the object autocorrelation is related to the power spectral density via a Fourier Transform relationship. Here, the phase retrieval problem is presented as only the Fourier magnitude is estimated. In the

next section of this chapter, methods for recovering the Fourier phase of the unknown object are discussed.

2.3 Phase Retrieval

The problem of phase retrieval comes about when measured data presents only the magnitude of the signal's Fourier Transform. In the LADAR application presented in this paper, the intensity or magnitude squared is collected. Without constraints or knowledge of the signal, the loss of the phase is irreversible [21]. However, from the body of research available on phase retrieval problems, with certain constraints and *a priori* knowledge of the signal, a recovery is possible.

The idea of synthesizing images from non-imaged laser-speckle is not new. In 1987, Idell *et al.* proposed a method for recovering unspeckled images and demonstrated this technique possible with computer simulation [25]. It is this seminal paper where the starting point of our research is found. An estimate of the object auto-correlation is formed from many laser speckle images. From this, a phase retrieval algorithm is employed to produce an estimate of the object. Several phase retrieval algorithms have been proposed in published literature that support our LADAR remote sensing application. A review of these algorithms is presented next.

2.4 Phase Retrieval Algorithms

Dainty and Fienup detail a thorough review of several phase retrieval methods to include Newton-Raphson, gradient search, and iterative methods [7,12]. The phase retrieval problem presents itself in many applications to include optical images formed with incoherent illumination. For the application considered here, a short review of applicable phase retrieval algorithms is presented.

2.4.1 Gerchberg-Saxton Algorithm. Gerchberg and Saxton suggested iterating between two sets of data that are related by the Fourier Transform [15]. They suggest simultaneously recording intensity measurements in both the image and pupil

planes. The algorithm starts with an initial phase guess generated by a uniform random number generator ($-\pi$ to π). The guessed phase is multiplied to the measured amplitude in the image plane and the Fourier Transform is taken mapping the data to the pupil plane. The computed phase from this operation is multiplied to the amplitude of the pupil plane data. Again, a Fourier transform is performed mapping the manipulated data set back to the image plane. The computed phase in this operation is applied to the amplitude of the image plane data. This iterative operation continues until operator intervention or the desired level of error is reached. Gerchberg and Saxton demonstrated the estimate error decreases or remains constant for each iteration. This is an attractive property of the algorithm; it avoids a diverging solution.

2.4.2 Fienup's Algorithms. Fienup details two phase retrieval algorithms descending from the work of Gerchberg and Saxton. The first, Fienup's Error Reduction method is essentially a generalized form of the Gerchberg-Saxton phase retrieval algorithm [11, 12] and is often quoted in literature. The algorithm essentially iterates between object and Fourier domains where known constraints are applied to the data before continuing with the next iteration. For the object domain, the object is assumed to be positive and within a known observation region, called object support. In the beam-limited, LADAR application, the support region is provided by the extent of the illuminating laser beam. For the Fourier domain, the modulus of the Fourier Transform of the object field is known from the observed data. For the LADAR application considered here, this results from the square root of the Fourier Transform of the noisy (estimated) autocorrelation data. Figure 2.1 depicts a block diagram of Fienup's Error Reduction algorithm [11].

An initial guess of the object is required for the algorithm. Without any knowledge of the object, the guess can be from an infinite number of choices. However, the extent of the object or support region may be known or assumed. Often, the initial guess is chosen to be the support region itself perturbed with random noise. In a

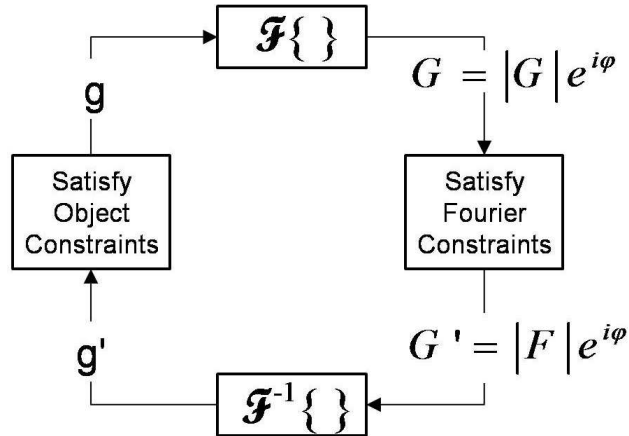


Figure 2.1: Block Diagram of Fienup's Error Reduction Method [11]

later paper [12], Fienup proposes stopping criteria to be the squared error between the Fourier constraint and the computed Fourier Transform (similar in the object domain for successive iterations). This algorithm is a single frame algorithm; it operates on a single autocorrelation estimate. Without stopping criteria, the algorithm runs until operator intervention or the number of chosen iterations has been exceeded.

Fienup also presents the input-output algorithm to speed convergence [11, 12]. Fienup adapts the error reduction algorithm to produce a non-linear approach where the input does not necessarily satisfy the object domain constraints. Also, the input to the algorithm at each iteration is not considered the current best estimate and can be modified. Fienup suggests multiple methods for selecting a new estimate of the object input and recommends periodically changing the selection method after several iterations. Fienup also suggests a hybrid approach where the error reduction algorithm is combined with the input-output algorithm. Although Fienup reports this as a very powerful approach, it appears ad hoc through arbitrary user intervention.

2.4.3 Schulz-Snyder Algorithm. Schulz and Snyder present a unique image recovery algorithm that operates on n th order correlations [38]. A phase retrieval algorithm is presented with $n = 2$. Schulz and Snyder choose to maximize a log-likelihood function of the data where a Poisson model is selected. Schulz and Snyder

acknowledge that few applications present autocorrelation data corrupted by Poisson noise; however, he states this model does enforce positivity and is similar to cases where the noise is signal dependent. For applications with signal dependent noise but unknown distribution this algorithm may be a good choice. For the application considered in this paper, the autocorrelation does not exhibit Poisson noise as discussed in Chapter III. Equation 2.3 depicts the Schulz-Snyder iterative algorithm:

$$o_{k+1}(x) = \frac{o_k(x)}{2 \sum_x o_k(x)} \sum_y \left[o_k(x+y) + o_k(x-y) \right] \frac{\tilde{R}_o(y)}{R_o(y)}, \quad (2.3)$$

where o_{k+1} is the new estimate of the object, o_k is the old estimate of the object from the previous iteration, $\tilde{R}_o(y)$ is the measured autocorrelation (observed data), and $R_o(y)$ is the autocorrelation formed from the old object estimate. Using notation found within this document, the Schulz-Snyder algorithm is re-written to be

$$o^{\text{new}}(\mathbf{x}) = \frac{o^{\text{old}}(\mathbf{x})}{2S_o^{\text{old}}} \left[o^{\text{old}} \star \frac{\tilde{R}_o}{R_o^{\text{old}}} + o^{\text{old}} * \frac{\tilde{R}_o}{R_o^{\text{old}}} \right](\mathbf{x}), \quad (2.4)$$

where \star is correlation, $*$ is convolution, o^{new} is the new object estimate, o^{old} is the object estimate from a previous iteration, \tilde{R}_o is the measured autocorrelation, R_o^{old} is the autocorrelation formed from the old estimate of the object, and S_o^{old} is the two-dimensional sum of the old object estimate.

The Schulz-Snyder algorithm also requires a support region where the object is known to exist and an initial guess. Schulz and Snyder caution against using a smooth, uniform image as the initial guess and suggest an asymmetric starting image [38]. The initial guess for the Schulz-Snyder algorithm can also be a gross starting point such as the support region perturbed with independent random variables distributed uniformly over the interval [0.99,1.01]. The Schulz-Snyder algorithm is also a single frame algorithm and no stopping criteria is provided. The Schulz-Snyder iterative

algorithm can be characterized as a gradient search method with object constraints used to aid in convergence. The initial guess (positive with support) enforces a solution only within the support region as well as object positivity.

2.4.4 Phillips' Algorithm. Phillips presents a statistical approach to the phase retrieval problem claiming Gaussian statistics when the number of independent laser speckle patterns, K , is large [32]. While the Central Limit Theorem suggests this is true under the right conditions, Chapter III suggests this is a poor approximation for our LADAR application. From the Gaussian assumption, the log-likelihood is:

$$L(o) = -\frac{1}{2\sigma^2(\mathbf{y})} \sum_{\mathbf{y}} \left(d(\mathbf{y}) - \sum_{\mathbf{x}} o(\mathbf{x})o(\mathbf{x} + \mathbf{y}) \right)^2, \quad (2.5)$$

where $o(x)$ is the true object, $d(y)$ is the average speckled autocorrelation, and $\sigma^2(y)$ is the variance. An iterative maximization approach is accomplished with the k th frame data model detailed in Eqn. 2.6. Averaging the data over K number of frames is assumed to be Gaussian with a mean equal to the Idell function (Eqn. 2.2). A sample variance is computed from the K observed frames.

$$d^k(\mathbf{y}) = \left| \mathcal{F}^{-1} \left\{ \left| \mathcal{F}^{\lambda z} \{o(\mathbf{x})\} \right|^2 + n^k(\mathbf{u}) \right\} \right|^2 \quad (2.6)$$

Phillips suggests a low-resolution image as the starting point. The author found the Phillips algorithm to converge with a random guess as the starting image identical to Fienup and Schulz-Snyder. The Phillips algorithm may be implemented as a multi-frame algorithm iteratively operating on each noisy autocorrelation realization obtained after each laser pulse. Lastly, Phillips suggests a statistical based stopping criteria.

2.5 Additional Image Recovery Efforts

In addition to the above phase retrieval algorithms, additional methods for object recovery have been suggested for identical or similar applications.

2.5.1 Phillips Joint Algorithm. Originally proposed by Cain [3], Phillips and Cain describe a joint algorithm using both image and pupil plane data together to aid image recovery [33]. The application considered is identical to the application in this research: a coherent LADAR scenario with both image and pupil plane data available. The Phillips and Cain technique essentially combines blind deconvolution of laser imaging and phase retrieval of laser speckle pattern data to produce the reconstructed image. A Bayesian method is presented that assumes a statistical model for the image and pupil plane data sets. A combined joint probability density function is developed and subsequently a joint log likelihood function. The log likelihood function is then maximized through an iterative technique as a solution for the object estimate. Two primary assumptions are taken to develop this algorithm. First, the image and pupil plane data sets, though collected simultaneously, are statistically independent. Second, the average speckle autocorrelation (from the pupil plane data) is approximated as Gaussian. While the first assumption is presented without proof, it is reasonable if the image and pupil plane data are collected at angular or range offsets. With a slight change in angle, the random phase contributions from the rough surface produce a different speckle realization at the image and pupil plane collections. The second assumption is provided from the Central Limit Theorem as a result of averaging a large number of laser speckle autocorrelations in the processed data. This assumption is questioned for this research and discussed further in Chapter III.

The Phillips Joint algorithm provides an important method as many remote sensing applications use an optical imaging system or have an imaging capability available. However, the image recovery result depends upon the resolution of the imaging system and the number of laser speckle patterns collected. The better resolution of the imaging system and the more laser speckle patterns collected, the better

this algorithm performs. Often, optical resolution and data collection time are premium quantities. This research hopes to decouple the need for the optical imaging system and reduce the number of laser speckle patterns required through better statistical models.

2.5.2 Sparse Arrays of Detectors. Fienup and Idell proposed nonimaged laser speckle pattern collection with large, yet sparse or partially filled detection arrays [14]. This research extends the previous work by the same authors to a large array developed from a synthetic array of subapertures. This partially filled array does distort the recovered image via a transfer function. However, Fienup and Idell demonstrate with sufficient post-processing the transfer function effects can be largely removed. This result is important for applications where a very large aperture is required; however, is synthesized with smaller subaperture hosted on multiple vehicles or geographically dispersed. It is important to note the synthetic array is not developed by translating a single subaperture in time as in Synthetic Aperture RADAR. For the application considered in this research, multiple subapertures collect data at the same time.

2.5.3 Other Novel Ideas. Additional ideas are presented throughout literature and are too numerous to summarize in this document. Many of the published phase retrieval algorithms and methods do not apply to the application considered in this research. However, a few applicable techniques are worthy of mention.

Guizar-Sicairos and Fienup address the effects of a finite sized detector array on the iterative reconstruction algorithms using Fast Fourier Transforms (FFTs) [20]. In any physical system implemented to measure backscatter energy from coherent illumination, the reflected field extends beyond the width of the detector array. The authors suggest this discontinuity in the truncated intensity data causes aliasing or non-physical effects during computer simulation. Also, a finite object will have an infinite spectrum causing computational problems with iterative techniques. The authors propose a weighted projection in the Fourier domain to compensate. Guizar-

Sicairos and Fienup state this technique improves image quality without sacrificing resolution and is robust in the presence of noise. For the research considered in this paper, the proposed physical system will involve a beam-limited scenario. The laser beam illuminating any real object will normally have significant roll-off in power at the edges of the beam. Therefore, a “hard object edge” from the object or assumed support region as described by Guizar-Sicairos and Fienup is not encountered. The finite support in our research is considered to be the extent of the illuminating beam without further assumption of the object extent. This research will ensure aliasing due to computation is eliminated through proper sampling in the observation plane.

In another research effort, Seldin and Fienup showed the use of the Ayers-Dainty two-dimensional Blind Deconvolution Algorithm applied to phase retrieval [40]. The Ayers-Dainty algorithm is an important result with broad implications throughout remote sensing and image processing. Blind deconvolution is attempted when one seeks to solve for two unknown functions from a single noisy measurement (see Eqn. 2.7). This is often the case in imaging where the point spread function, $g(\mathbf{x})$, of the system is unknown due to atmospheric distortion. In the blind deconvolution problem for imaging, one hopes to recover the image, $f(\mathbf{x})$, through iterative computation where the point spread function must be estimated.

$$d(\mathbf{x}) = f(\mathbf{x}) * g(\mathbf{x}) + n(\mathbf{x}) \tag{2.7}$$

Seldin and Fienup point out that phase retrieval is a special case of blind deconvolution when $n(\mathbf{x}) = 0$ and $g(\mathbf{x}) = f^*(-\mathbf{x})$ because of the relationship of the autocorrelation, $R(\mathbf{x})$, to the modulus squared of the Fourier Transform.

$$\begin{aligned}
R(\mathbf{x}) &= f(\mathbf{x}) * f^*(-\mathbf{x}) \\
&= \mathcal{F}^{-1}\{ F(\mathbf{u})F^*(\mathbf{u}) \} \\
&= \mathcal{F}^{-1}\{ |F(\mathbf{u})|^2 \}
\end{aligned} \tag{2.8}$$

Note that autocorrelation is a special case of the convolution theorem when $f(\mathbf{x})$ is convolved with $f^*(-\mathbf{x})$ [18]. Seldin and Fienup applied the Ayers-Dainty algorithm and assumed, f and n are independent, zero-mean, Gaussian random processes for the Wiener filter. The authors acknowledge most images do not satisfy this assumption. However, they show the filter is effective with the end result equivalent to the Fienup error reduction algorithm in zero or low noise cases. While this approach is not a significant improvement over other techniques, it does further demonstrate the mathematical importance of the phase retrieval problem. Correct statistical models are significant for improving upon existing phase retrieval algorithms.

This research investigated polarization diversity for improving the phase retrieval problem. Multi-channel diversity is not a new concept. Holmes *et al.* applied several iterative methods to intensity data formed from two illuminating sources separated in frequency [23, 24]. For this specific detection scheme, the Expectation-Maximization algorithm approach is further motivated and detailed mathematically by Schulz and Voelz [39]. Essentially, two fields, E_1 and E_2 , separated by frequency illuminate the distant object and the fields are reflected to an array of detectors such that the individual field component magnitudes and a field cross product is measured. The measured intensity in the pupil plane at time t is

$$I(\mathbf{x}, t) = |E_1(\mathbf{x}) \exp(jw_1t) + E_2(\mathbf{x}) \exp(jw_2t)|^2, \tag{2.9}$$

where w_1 and w_2 are slightly different frequencies. Holmes *et al.* state the speckle field intensities $|E_1(\mathbf{x})|^2$ and $|E_2(\mathbf{x})|^2$ must be measured separately in order to solve four equations for the two unknown fields E_1 and E_2 from noisy data I_1, I_2, I_r, I_i related by:

$$I_1(\mathbf{x}) = |E_1(\mathbf{x})|^2 + n_1(\mathbf{x}), \quad (2.10)$$

$$I_2(\mathbf{x}) = |E_2(\mathbf{x})|^2 + n_2(\mathbf{x}), \quad (2.11)$$

$$I_r(\mathbf{x}) = \text{Re}[E_1(\mathbf{x})E_2^*(\mathbf{x})] + n_r(\mathbf{x}), \quad (2.12)$$

$$I_i(\mathbf{x}) = \text{Im}[E_1(\mathbf{x})E_2^*(\mathbf{x})] + n_i(\mathbf{x}), \quad (2.13)$$

where n_1, n_2, n_r, n_i represent noise and $*$ represents conjugation. Holmes *et al.* view this as a phase retrieval problem solving for both reflected fields with a cross-phase constraint provided by $E_1(\mathbf{x})E_2^*(\mathbf{x})$. In companion papers, the authors review several algorithms for this problem in both the root-matching method and iterative algorithm method [23, 24]. The two separate field intensities, $|E_1(\mathbf{x})|^2$ and $|E_2(\mathbf{x})|^2$ are unrelated; they are two distinct measurements of the target. Only with the difficultly obtained field cross product can this problem be attempted. The simulated results are attractive; however, the practical implementation with optical hardware appears to be extremely difficult as the field cross product must be isolated from the combined intensity measurement. The field cross product is easily obtained at RADAR frequencies but is problematic at optical frequencies requiring complex interferometric hardware. Obtaining the field cross product, $E_1(\mathbf{x})E_2^*(\mathbf{x})$ introduces an additional processing and estimation problem avoided in this research.

For the Holmes *et al.* two field mixing approach discussed above, Schulz and Voelz detail the theory and algorithm for the generalized expectation-maximization (EM) method. A Poisson probability mass function for the data is assumed similar to the Schulz-Snyder phase retrieval algorithm from cross-correlations. The Schulz

and Voelz result is of interest to this research as an EM algorithm is presented in this dissertation. This is further discussed in Chapters III and IV.

III. Research Foundations

This chapter provides the sensor and mathematical models used for this research as well as some preliminary developments for the task of object recovery. In addition to the basic mathematical model of the observed and processed data, a statistical framework is presented as a basis for the new research. A case is made for the exponential probability density function describing the random nature of the processed data. This probability description is used throughout the remaining document, supporting object recovery and a theoretical resolution bound. Lastly, maximum likelihood (ML) and EM algorithms are explored using the exponential distribution.

3.1 Sensor Model

All of the optical detection technology required to perform the LADAR task described in Chapters I and II exist as commercially available hardware components. With proper engineering and system integration, a cost effective correlography and phase retrieval sensor system can be built with commercially available hardware components. Laser engineering and power considerations must be included based on the target size and distance. This section provides the proposed sensor model used to develop this research. Individual hardware component contributions to noise as well as calibration issues are not considered. Adding polarization sensitivity to the correlography system requires additional considerations detailed below.

3.1.1 Proposed Sensor Hardware. A large detection array may be “synthesized” using many individual detection elements without a large focusing lens. The array may be built to be quite large without the limitation of a single mounting frame but only limited by pointing and integration requirements. The individual detector elements must be pointed in the same direction to eliminate non-linear array effects. A square, uniform detection array is considered for simplicity. With the use of commercial off the shelf hardware and the avoidance of a large, monolithic optical

lens and refractive mirror, system developers can obtain significant cost savings over traditional optical systems.

A proposed scheme consists of employing polarizing beam splitters (PBSs) to produce two orthogonally polarized channels of observed data. A single detection element consists of a PBS followed by a small lenslet to focus the optical waveform and an optical detection element such as an avalanche photodiode (APD). Although not a required element, the lenslet is extremely small and cost efficient for focusing the optical energy onto the detection element. The lenslet does not aid in forming a traditional image. The APD would be followed by an analog-to-digital (A-D) converter. The digital data would be stored and processed using a computer processor. Figure 3.1 depicts a single hardware sub-element of the proposed array hardware. In this manner, a single array can be built for detecting two orthogonal channels.

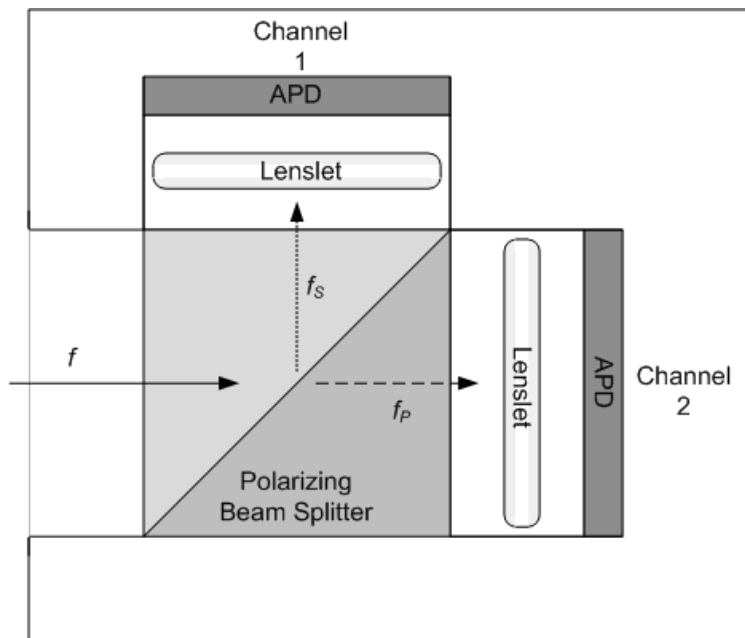


Figure 3.1: Single Hardware Sub-element for Polarimetric Correlography System

The PBS produces two orthogonally polarized data channels, normally referred to as S and P polarized channels. The S and P channels are attenuated by the effect of the polarization and degree of transmission through the PBS. Commercially available PBSs may be obtained with transmission efficiencies greater than 90 percent.

Computer simulations presented in Chapter VI assume transmission rates of 100 percent without significant departure from true hardware performance.

The two orthogonally polarized channels allow for unpolarized data collection as well (e.g. $S + P$); however, statistical independence between the polarized and unpolarized data sets is a consideration for system designers. Normally, $S + P$ will not be statistically independent from either S or P channels; therefore, an alternative design must be considered.

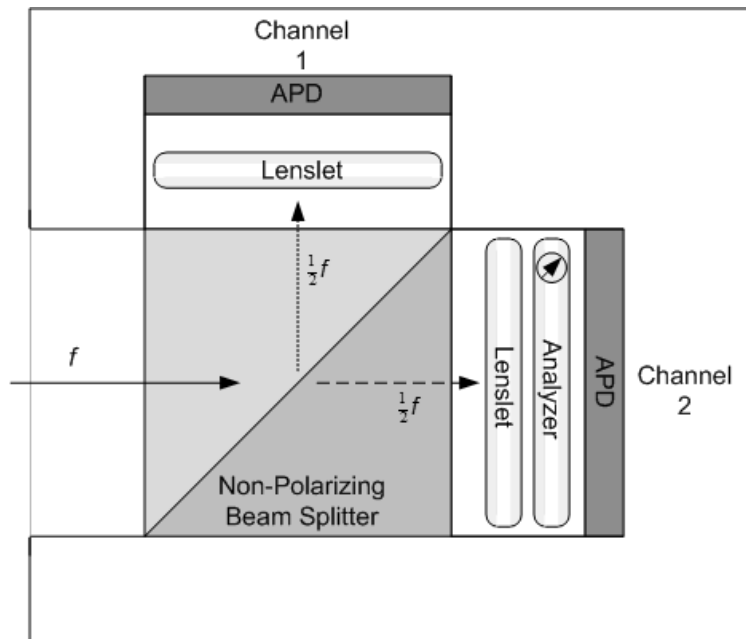


Figure 3.2: Alternative Sub-element for Polarimetric Correlography System

Use of a traditional beam splitter followed by polarizing film (or polarization analyzer) for the polarized channel may be employed but at a loss of light levels due to the nature of the beam splitter. A traditional, non-polarizing beam splitter will create two channels but only half the original light is transmitted to each channel. The polarized channel is further attenuated by the effect of the analyzer. Figure 3.2 demonstrates this system design using a traditional beam splitter. It is assumed here the PBS or non-polarizing beam splitter provides only linear polarization effects and transmission efficiencies are identical for the two output channels.

3.1.2 *Object Illumination.* In order to obtain an estimate of the object autocorrelation (or equivalently an estimate of the object’s Fourier magnitude), the correlography technique requires the object to be coherently illuminated. In the application considered here, the object is either spatially limited (e.g. satellite in orbit) or the the illuminating beam itself provides a spatial limit. Therefore, the illuminating beam must be spatially coherent across the entire extent of the beam or object surface. This is achievable with currently available technology. A reasonable scenario is considered with the geometry shown in Fig. 3.3: A satellite with $d_2 = 50$ meters extent is orbiting at $z = 36,000$ kilometers and the illuminating source has a finite extent of less than $d_1 = 1$ meter. The light originating at the edges of the source undergo different time delays, r_1/c and r_2/c . If the time difference $(r_2 - r_1)/c$ is much less than the coherence time, τ_c , of the source, then the spatial coherence (in the object plane) is observed [17]. With the proposed scenario and the remote object at such distances, the time difference is on the order of 10^{-16} seconds. Because the coherence time, τ_c , of a conventional laser is inversely proportional to the laser bandwidth [17], a coherent illumination across the extent of the object is easily achieved with a laser with bandwidth less than 1GHz. This laser bandwidth is easily achieved with available technology and does not present cost or design concerns for a proposed system.

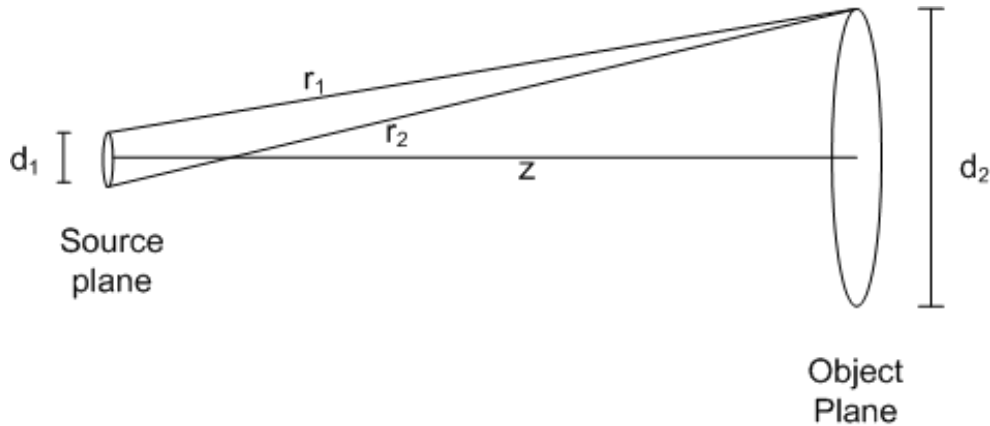


Figure 3.3: Geometry for Considering Spatial Coherence

Because polarization sensitivity is to be added, laser illumination characteristics should be considered during system design. We desire statistically independent

speckle realizations in the two observed channels. Reflectivity as a function of polarization may, depending on the object surface, provide statistical independence between polarimetric data sets. However, further system design should be adopted to ensure this effect is more readily observed. Simultaneous illumination with two laser beams with orthogonal polarizations and phase front difference (e.g. tilt) will also produce different speckle realizations within the two channels. Certainly, with sufficient phase differences in the two illuminating beams, different realizations of reflected phase are created at the object surface. Also, at low light levels, photo-detection noise will dominate the detection process providing statistically independent noise realizations in the two channels because of separate photo detectors.

3.2 Mathematical Model

The illuminated field at the target plane, $f(\mathbf{u})$, is spatially coherent across the extent of the target (or beam extent). The reflected field is observed repeatedly over many laser pulses in the far-field by a synthetic array of optical, “light-bucket” detectors without the aid of an optical lens. K statistically independent, laser speckle patterns are transformed through post-processing to produce noisy object autocorrelations, $d_k(\mathbf{x})$.

$$d_k(\mathbf{x}) = |\mathcal{F}^{-1}\{I_k(\mathbf{v})\}|^2, \quad (3.1)$$

where $I_k(\mathbf{v})$ is the k th frame of observed laser speckle data and \mathcal{F}^{-1} is the inverse Fourier transform performed digitally in a computer via a Digital Fourier Transform (DFT). The, k th frame of nonimaged laser speckle data, $I_k(\mathbf{v})$, is modeled by a Fraunhofer propagation ($\mathcal{F}^{\lambda z}$) with a mean wavelength λ and propagation distance z ,

$$I_k(\mathbf{v}) = |\mathcal{F}^{\lambda z}\{f_k(\mathbf{u})\}|^2 \cdot A(\mathbf{v}) + n_k(\mathbf{v}), \quad (3.2)$$

where $A(\mathbf{v})$ is the aperture function denoting the region the speckle pattern is observed and $n_k(\mathbf{v})$ is noise encountered in the detection process that includes photon noise, read-out noise, and noise due to background light. Speckle noise is inherent and occurs prior to detection due to coherent illumination and the random phase imparted on the reflected wavefront by the rough surface of the target (e.g. $f(\mathbf{u}) = |f(\mathbf{u})| \exp\{j\theta(\mathbf{u})\}$; $\theta(\mathbf{u})$ is modeled as uniformly random $\sim U[-\pi, \pi]$ and independent). Normally, a laser line filter is used to minimize background light.

Recalling Eqn. 2.2, the mean of the noisy object autocorrelations is related to the true object autocorrelation, $R_o(\mathbf{x})$,

$$E[d_k(\mathbf{x})] = b|h(\mathbf{x})|^2 + c[R_o(\mathbf{x}) * |h(\mathbf{x})|^2], \quad (3.3)$$

where b and c are constants, $|h(\mathbf{x})|^2$ is the known, incoherent point spread function (PSF) of the detector array, $R_o(\mathbf{x})$ is the true autocorrelation of the object intensity ($o = |f|^2$), and $*$ denotes convolution. If the detector array is uniform and no zero-padding is used in the DFT, the PSF is a weighted Dirac delta function, $\delta(\mathbf{x})$, and the mean of the transformed data simplifies to

$$E[d_k(\mathbf{x})] = b\delta(\mathbf{x}) + cR_o(\mathbf{x}). \quad (3.4)$$

The strength, b of the delta function in Eqn. 3.4 is related to the detector array and the intensity of the object scene (see Appendix B). To avoid estimation complexity for a single pixel of the data image, this pixel value is removed prior to any computation and replaced with the peak of the estimated object autocorrelation from the initial guess or old object estimate, o^{old} , from the previous iteration. With these simplifications, a measured object autocorrelation, $\tilde{R}_o(\mathbf{x})$ is obtained. The measured autocorrelation, $\tilde{R}_o(\mathbf{x})$, is defined by:

$$\tilde{R}_o(\mathbf{x}) = K^{-1} \sum_{k=1}^K d_k(\mathbf{x})[1 - \delta(\mathbf{x})] + \sum_{\mathbf{y}} [o^{\text{old}}(\mathbf{y})]^2 \delta(\mathbf{x}). \quad (3.5)$$

The measured autocorrelation is the average of the observed data, $d_k(\mathbf{x})$, with the central image pixel modified as discussed above.

3.3 Polarimetric Model

The polarimetric data in this research is obtained via a two-channel system: one channel is polarization insensitive and the second channel is observed through polarizing film or via a polarization beam splitter as detailed in Sec. 3.1.1. Originally proposed by Strong [43], a lumped parameter, p , is introduced that is the polarization ratio. The polarization ratio is the ratio of the intensity observed in the polarized channel to the intensity observed in the unpolarized channel,

$$p = \frac{I_{pc}}{I_{upc}}, \quad (3.6)$$

where $0 \leq p \leq 1$. The polarization ratio is essentially the projection of the object intensity, o , as viewed through the polarizer, or, the fraction of light transmitted through the polarizer,

$$o_p(\mathbf{y}) = p(\mathbf{y})o(\mathbf{y}). \quad (3.7)$$

For this development, the polarization of the object scene (or degree of polarization) is not estimated nor is an assumption made regarding the decomposition of the reflected light into polarized and unpolarized components as found in [28]. The lumped parameter p is not useful for determining the scene's degree of polarization; however, this parameter enables us to relate polarized and unpolarized data elements. The polarization ratio, p is only used to solve for the unknown object, o .

Normally, this phase retrieval problem can be characterized by one equation and two unknowns (Fourier magnitude and phase). By adding a second measurement that is related to the first, the problem is characterized by two equations and three unknowns (magnitude, phase, and polarization ratio). The second, but related measurement, further constrains the problem, improving search performance. Using Eqn. 3.4, suppressing the energy at the central pixel, $b\delta(\mathbf{x})$, and applying the polarimetric model, the Expected Values of the data in the two channels are

$$E[d_k^{(1)}(\mathbf{x})] = [1 - \delta(\mathbf{x})] \sum_{\mathbf{y}} o(\mathbf{y})o(\mathbf{y} + \mathbf{x}), \quad (3.8)$$

$$E[d_k^{(2)}(\mathbf{x})] = [1 - \delta(\mathbf{x})] \sum_{\mathbf{y}} o_p(\mathbf{y})o_p(\mathbf{y} + \mathbf{x}). \quad (3.9)$$

Equations 3.8 and 3.9 are used in Chapter IV to develop an algorithm to solve for the unknown object.

3.4 Statistical Model

An accurate statistical model is important for any statistical-based estimator, the focus of this research. Previous research in correlography similar to the application considered here has not explored the statistics of the processed data. Much of the image-recovery via phase-retrieval research area involves gradient search, root-finding or Fourier transform-based algorithms where a “best-fit” solution is found through iterative search techniques [12]. Often, assumptions about the remote object are used to make the computation tractable (e.g. positivity and spatial bound). These approaches do not employ a statistical model for the data (e.g. [11, 24]). Other research efforts provide an assumption of the noise statistics for the processed data (e.g. Gaussian [23, 33]). This research endeavors to better characterize the noise statistics of the processed data. First, the underlying assumptions of the object are stated and assumed similar to those found in previous research.

The statistics of laser speckle due to polarized thermal light are well known [16, 17, 19]. The probability distribution function (pdf) of instantaneous intensity for speckle caused by object phase with a uniform distribution is known to be negative exponential. The intensity captured by any real detector will be an integrated intensity for a finite integration time, T , and measured in photocounts. The resulting density function is the negative binomial distribution [17]. This assumes perfectly polarized light. Partially polarized or unpolarized light will have a different result.

However, with three key assumptions, the statistics of the observed laser speckle intensity may be analyzed:

1. The amplitude and phase of the reflected field are statistically independent. This assumption is reasonable since the amplitude is a function of the object reflectivity and the phase is a function of the surface roughness or height profile. These two physical elements are unrelated.
2. The phase is spatially independent and identically distributed. This assumption is essentially that the sample size is not small enough to produce statistical dependence due to nearness of the sampled points being related by similar roughness.
3. The object surface roughness is modeled as a uniform random variable distributed between $(-\pi, \pi)$ and statistically independent. This assumption is valid for most surfaces (other than mirrored surfaces) as the surface is considered “rough” if the surface height profile is much greater than the wavelength of the illuminating field.

Even if the distribution of the observed laser speckle intensity deviates from the negative binomial due to partial polarization of the illuminating beam, a key result is observed. If these three assumptions are valid, the expected value of the laser speckle intensity is easily shown to be a constant (see Appendix A).

Knowledge of the average value of the laser speckle intensity patterns will enable the exploration of the statistics of the processed or transformed laser speckle data.

Largely due to this expected value result, Appendix C demonstrates the statistics of the transformed data is well approximated by the exponential distribution. Because of this result, an ML solution was investigated for solving this particular phase retrieval problem.

It will be assumed that each frame of collected laser speckle intensity data is statistically independent. This is accomplished if the phase at the object surface is statistically independent from pulse to pulse. This is reasonably observed if minute geometry changes occur from pulse to pulse that produce this effect. These pulse-to-pulse geometry changes may include target jitter due to movement, target surface deformation due to compliant structures, laser (source) jitter, etc. Certainly, this effect is a system design consideration as each frame of laser speckle must be statistically independent for the result detailed in Appendix B to be observed. Additionally, it is assumed the simultaneously observed data in the two channels (same pulse or frame) as collected via a PBS (S and P channels) are statistically independent due to surface reflectivity as a function of polarization and/or system design with dual illumination. Simultaneous illumination with two laser beams with orthogonal polarizations and phase front difference (e.g. tilt) will also produce different speckle realizations within the two channels. Also, at low light levels, photo-detection noise will dominate the detection process providing statistically independent noise realizations in the two channels because of separate photo detectors.

It will be further assumed the processed data frames are also statistically independent. It is assumed the mathematical transformation (magnitude squared of the Fourier transform) operating on each frame does not create statistical dependence between data frames.

With exponential statistics, the Signal-to-Noise Ratio (SNR) is easily described. The exponential distribution is completely described by the first moment or the expected value. Also, the expected value equals the standard deviation. For this reason, the SNR of the data set is a function of the number of frames collected, K . Because

the K noisy, exponentially distributed autocorrelations are summed together, the final distribution of the average autocorrelation is distributed as a gamma random variable with expected value equal to K/R_o and standard deviation equal to \sqrt{K}/R_o . Therefore, the SNR for the averaged autocorrelation computed from K frames of data is equal to \sqrt{K} .

3.5 Maximum Likelihood Approach

With laser speckle intensity data transformed to noisy autocorrelations and the noise modeled with an exponential probability density function, an ML solution is investigated. Only a single channel of unpolarized data is considered.

The observed data is the autocorrelation of the unknown object corrupted by exponential noise. Many statistically independent realizations are observed and collected. It is assumed the noise at each sampled point in the data image is statistically independent from all other points. The joint probability density function (pdf) for a single frame of data is

$$p_D(d(\mathbf{x})) = \prod_{\mathbf{x}} \frac{1}{R_o(\mathbf{x})} e^{-\frac{d(\mathbf{x})}{R_o(\mathbf{x})}}. \quad (3.10)$$

The expected value, R_o , is defined by

$$R_o(\mathbf{x}) = \sum_{\mathbf{t}} o(\mathbf{y})o(\mathbf{y} + \mathbf{x}), \quad (3.11)$$

where $o(\mathbf{t})$ is the unknown object intensity and \mathbf{y} and \mathbf{x} are two dimensional coordinate vectors. We will also assume each frame of observed data is statistically independent from all other collected data frames. For K frames of data, the joint pdf is

$$p_D(d_1(\mathbf{x}), \dots, d_K(\mathbf{x})) = \prod_k \prod_{\mathbf{x}} \frac{1}{R_o(\mathbf{x})} e^{-\frac{d_k(\mathbf{x})}{R_o(\mathbf{x})}}. \quad (3.12)$$

Forming the log-likelihood function, L , by taking the natural logarithm of the joint pdf yields

$$L = -K \sum_{\mathbf{x}} \ln R_o(\mathbf{x}) - \sum_k \sum_{\mathbf{x}} \frac{d_k(\mathbf{x})}{R_o(\mathbf{x})}. \quad (3.13)$$

Taking the partial derivative of L with respect to the object produces the next equation.

$$\frac{\partial L}{\partial o(\mathbf{y})} = -K \sum_{\mathbf{x}} \frac{1}{R_o(\mathbf{x})} \frac{\partial R_o(\mathbf{x})}{\partial o(\mathbf{y})} + \sum_k \sum_{\mathbf{x}} \frac{d_k(\mathbf{x})}{R_o^2(\mathbf{x})} \frac{\partial R_o(\mathbf{x})}{\partial o(\mathbf{y})} \quad (3.14)$$

Next, the partial derivative of $R_o(\mathbf{x})$ with respect to the object, $o(\mathbf{y})$, is computed.

$$\frac{\partial R_o(\mathbf{x})}{\partial o(\mathbf{y})} = o(\mathbf{y} + \mathbf{x}) + o(\mathbf{y} - \mathbf{x}) \quad (3.15)$$

Substituting this result into $\partial L/\partial o$ yields

$$\begin{aligned} \frac{\partial L}{\partial o(\mathbf{y})} &= -K \sum_{\mathbf{x}} R_o^{-1}(\mathbf{x}) [o(\mathbf{y} + \mathbf{u}) + o(\mathbf{y} - \mathbf{u})] \\ &\quad + \sum_k \sum_{\mathbf{x}} R_o^{-2}(\mathbf{x}) d_k(\mathbf{x}) [o(\mathbf{y} + \mathbf{u}) + o(\mathbf{y} - \mathbf{u})]. \end{aligned} \quad (3.16)$$

Setting this equal to zero and solving for o maximizes the function L with respect to the object, o . Since a closed form solution for o is not feasible, an approach similar to the Richardson-Lucy (RL) algorithm used in deconvolution [29, 34] is employed. The ratio of the negative to positive parts of this function is formed and o is solved iteratively from an initial guess. First, define the average value of the observed data, $D(\mathbf{x})$, as

$$D(\mathbf{x}) = \frac{1}{K} \sum_k d_k(\mathbf{x}). \quad (3.17)$$

The RL approach to iteratively solve for o is then given to be:

$$o^{new}(\mathbf{y}) = o^{old}(\mathbf{y}) \cdot \frac{\frac{D(\mathbf{x})}{R_o^2(\mathbf{x})} \star o(\mathbf{x}) + \frac{D(\mathbf{x})}{R_o^2(\mathbf{x})} * o(\mathbf{x})}{\frac{1}{R_o(\mathbf{x})} \star o(\mathbf{x}) + \frac{1}{R_o(\mathbf{x})} * o(\mathbf{x})}, \quad (3.18)$$

where \star is correlation and $*$ is convolution. This algorithm is problematic in two respects: (1) The algorithm does not naturally constrain the object magnitude, and allows for o to grow without bound each iteration, and (2) the algorithm presents numeric challenges due to division by the squared term R_o which is the current estimate of the object autocorrelation. This ML approach utilizes a more correct statistical model than previously published algorithms; however, it does not provide a useable algorithm as evidenced by analysis with computer simulation. The generalized expectation-maximization technique provides a broader and more powerful ML estimate compared to the ML technique described above.

3.6 *Expectation-Maximization Approach*

The EM algorithm was systematically defined and convergence proved in the seminal paper by Dempster, Laird and Rubin (DLR) [9]. The DLR paper coalesced previous research and journal papers treating this generalized approach to developing ML estimates. The EM technique has wide applicability with desirable convergence properties. This approach provides a powerful tool for solving problems involving missing or incomplete data or direct access to the data necessary to estimate the required parameters is impossible [30]. Although convergence properties have been revisited since the original paper [45], the EM algorithm does guarantee convergence to a local maximum as the likelihood function is increased at every iteration. The EM algorithm is guaranteed to be stable and converges to an ML estimate [30]. The EM approach is well-suited for the phase retrieval problem presented in this research. The EM approach has been used in a related phase retrieval problem [39].

We wish to estimate an object, $o(\mathbf{x})$, from many statistically independent realizations of observed data produced by a random process. However, the observed data

are corrupted by noise. From observed data, noisy autocorrelation data are produced via a post-processing transformation operation. Each point in the resulting autocorrelation data is an identically distributed and statistically independent exponential random variable. This processed data provides an incomplete view of the parameter to be estimated and is called incomplete data. The unobserved data containing the required information is called the complete data, $\tilde{d}_k(\mathbf{y}, \mathbf{x})$. The complete data is related to the incomplete data, $d_k(\mathbf{x})$ by

$$d_k(\mathbf{x}) = \left| \sum_{\mathbf{y}} \tilde{d}_k(\mathbf{y}, \mathbf{x}) e^{j\theta(\mathbf{y})} \right|^2, \quad (3.19)$$

where the complete data is multiplied by a uniformly distributed phasor, $\theta(\mathbf{y})$, summed over all values of \mathbf{y} , and then a magnitude squared operation is performed. The subscript k denotes the data frame and \mathbf{x} and \mathbf{y} are each two-dimensional spatial variables. This operation: random phasor sum, magnitude squared operation results in a quantity with an exponential distribution. The incomplete data is known to be exponentially distributed with mean equal to the autocorrelation of the desired object. The random phasor sum, magnitude squared seems to be a natural choice of complete data that leads to exponentially distributed incomplete data.

$$E[d_k(\mathbf{x})] = \sum_{\mathbf{y}} o(\mathbf{y})o(\mathbf{y} + \mathbf{x}) \quad (3.20)$$

Because the the mean of the incomplete data is known, the complete data is chosen to have the following property:

$$E[\tilde{d}_k^2(\mathbf{y}, \mathbf{x})] = o(\mathbf{y})o(\mathbf{y} + \mathbf{x}). \quad (3.21)$$

The complete data is selected in this manner due to the following:

$$\begin{aligned}
E[d_k(\mathbf{x})] &= E \left[\sum_y \sum_{y_1} \tilde{d}_k(\mathbf{y}, \mathbf{x}) \tilde{d}_k(\mathbf{y}_1 + \mathbf{x}) \exp\{j[\theta(\mathbf{y}) - \theta(\mathbf{y}_1)]\} \right] \\
&= \sum_y \sum_{y_1} E[\tilde{d}_k(\mathbf{y}, \mathbf{x}) \tilde{d}_k(\mathbf{y}_1 + \mathbf{x})] E[\exp\{j[\theta(\mathbf{y}) - \theta(\mathbf{y}_1)]\}] \\
&= \sum_y \sum_{y_1} E[\tilde{d}_k(\mathbf{y}, \mathbf{x}) \tilde{d}_k(\mathbf{y}_1 + \mathbf{x})] \delta(\mathbf{y} - \mathbf{y}_1) \\
&= \sum_y E[\tilde{d}_k^2(\mathbf{y}, \mathbf{x})] \\
&= \sum_y o(\mathbf{y})o(\mathbf{y} + \mathbf{x}) \tag{3.22}
\end{aligned}$$

Because the phase term, $\theta(\mathbf{y})$ is uniformly distributed $[-\pi, \pi]$ and independent, the complete data can be of any distribution or non-random and yield the correct mean for the incomplete data. The distribution of the complete data can then be chosen in the most advantageous manner. The square of the original complete data is chosen to be the new complete data of interest and a Poisson random variable.

$$\tilde{\tilde{d}}_k(\mathbf{y}, \mathbf{x}) \stackrel{\text{def}}{=} \tilde{d}_k^2(\mathbf{y}, \mathbf{x}) \tag{3.23}$$

$$P \left[\tilde{\tilde{d}}_1(\mathbf{y}, \mathbf{x}), \dots, \tilde{\tilde{d}}_K(\mathbf{y}, \mathbf{x}) \right] = \prod_k \prod_x \prod_y \frac{[o(\mathbf{y})o(\mathbf{y} + \mathbf{x})]^{\tilde{\tilde{d}}_k(\mathbf{y}, \mathbf{x})}}{\tilde{\tilde{d}}_k(\mathbf{y}, \mathbf{x})!} \exp \left[-o(\mathbf{y})o(\mathbf{y} + \mathbf{x}) \right] \tag{3.24}$$

The log-likelihood function of the complete data, L_{CD} , is found by taking the natural log of the probability mass function in Eqn. 3.24.

$$L_{CD}(o) = \sum_k \sum_x \sum_y \left\{ \tilde{d}_k(\mathbf{y}, \mathbf{x}) \log[o(\mathbf{y})o(\mathbf{y} + \mathbf{x})] - [o(\mathbf{y})o(\mathbf{y} + \mathbf{x})] - \log[\tilde{d}_k(\mathbf{y}, \mathbf{x})!] \right\} \quad (3.25)$$

3.6.1 Expectation Step. The expectation step of the EM algorithm, or Q-Function (Q), is defined as the expectation of the complete data log-likelihood function conditioned on the old estimate of the object from the previous iteration, $o^{\text{old}}(\mathbf{y})$, and the incomplete data, $d_k(\mathbf{x})$,

$$Q(o|o^{\text{old}}, d_k(\mathbf{x})) \stackrel{\text{def}}{=} E[L_{CD}(o) | o^{\text{old}}, d_k(\mathbf{x})]. \quad (3.26)$$

$$Q(o|o^{\text{old}}) = \sum_k \sum_x \sum_y E[\tilde{d}_k(\mathbf{y}, \mathbf{x}) | o^{\text{old}}, d_k(\mathbf{x})] \cdot \log [o(\mathbf{y})o(\mathbf{y} + \mathbf{x})] - K \sum_x \sum_y [o(\mathbf{y})o(\mathbf{y} + \mathbf{x})] - \text{A.T.} \quad (3.27)$$

where K is the total number of frames and A.T. denotes another term not a function of the object, o . Next, the conditional expectation of the complete data given the incomplete data, μ , is computed:

$$\mu(o^{\text{old}}, d_k(\mathbf{x})) = E[\tilde{d}_k(\mathbf{y}, \mathbf{x}) | o^{\text{old}}, d_k(\mathbf{x})]. \quad (3.28)$$

This is often the most difficult step in computing the EM algorithm. It may be difficult to solve for the mean of the conditional density function. This was attempted for Eqn. 3.28. Using Bayes' rule, we define the conditional probability mass function

(pmf) of the complete data given the incomplete data (for a specific frame k , and specific spatial variables y and x) as

$$P[\tilde{d}_k(\mathbf{y}, \mathbf{x}) \mid d_k(\mathbf{x})] = \frac{p[d_k(\mathbf{x}) \mid \tilde{d}_k(\mathbf{y}, \mathbf{x})]P[\tilde{d}_k(\mathbf{y}, \mathbf{x})]}{p[d_k(\mathbf{x})]} \quad (3.29)$$

The probability mass function of the complete data is specified and the probability density function of the incomplete data is known. The probability density function of the incomplete data given the complete data can be assumed to be exponentially distributed; therefore can be specified by only its mean. The mean of this conditional density is found by

$$\begin{aligned} E[d_k(\mathbf{x}) \mid \tilde{d}_k(\mathbf{y}_0, \mathbf{x})] &= \sum_{\mathbf{y}} \sum_{\mathbf{y}_1} E[\tilde{d}_k(\mathbf{y}, \mathbf{x})\tilde{d}_k(\mathbf{y}_1 + \mathbf{x}) \mid \tilde{d}_k(\mathbf{y}_0, \mathbf{x})] E[\exp\{j[\theta(\mathbf{y}) - \theta(\mathbf{y}_1)]\}] \\ &= \sum_{\mathbf{y}} \sum_{\mathbf{y}_1} E[\tilde{d}_k(\mathbf{y}, \mathbf{x})\tilde{d}_k(\mathbf{y}_1 + \mathbf{x}) \mid \tilde{d}_k(\mathbf{y}_0, \mathbf{x})] \delta(\mathbf{y} - \mathbf{y}_1) \\ &= \sum_{\mathbf{y}} E[\tilde{d}_k(\mathbf{y}, \mathbf{x}) \mid \tilde{d}_k(\mathbf{y}_0, \mathbf{x})] \\ &= \sum_{\mathbf{y}} o(\mathbf{y})o(\mathbf{y} + \mathbf{x}) - o(\mathbf{y}_0)o(\mathbf{y}_0 + \mathbf{x}) + \tilde{d}_k(\mathbf{y}_0, \mathbf{x}). \end{aligned} \quad (3.30)$$

From this result the probability density function, p_D , of the incomplete data conditioned on the complete data is given as

$$p_D[d_k(\mathbf{x}) \mid \tilde{d}_k(\mathbf{y}, \mathbf{x})] = \frac{\exp\left[\frac{-d_k(\mathbf{x})}{\sum_{\mathbf{y}} o(\mathbf{y})o(\mathbf{y} + \mathbf{x}) - o(\mathbf{y}_0)o(\mathbf{y}_0 + \mathbf{x}) + \tilde{d}_k(\mathbf{y}_0, \mathbf{x})}\right]}{\sum_{\mathbf{y}} o(\mathbf{y})o(\mathbf{y} + \mathbf{x}) - o(\mathbf{y}_0)o(\mathbf{y}_0 + \mathbf{x}) + \tilde{d}_k(\mathbf{y}_0, \mathbf{x})}. \quad (3.31)$$

Returning to Bayes' rule, this specifies the probability mass function of the incomplete data given complete data.

$$\begin{aligned}
P[\tilde{d}_k(\mathbf{y}, \mathbf{x}) \mid d_k(\mathbf{x})] = & \left[\frac{\sum_y o(\mathbf{y})o(\mathbf{y} + \mathbf{x})}{\sum_y o(\mathbf{y})o(\mathbf{y} + \mathbf{x}) - o(\mathbf{y}_0)o(\mathbf{y}_0 + \mathbf{x}) + \tilde{d}_k(\mathbf{y}_0, \mathbf{x})} \right] \\
& \cdot \exp \left[\frac{-d_k(\mathbf{x})}{\sum_y o(\mathbf{y})o(\mathbf{y} + \mathbf{x}) - o(\mathbf{y}_0)o(\mathbf{y}_0 + \mathbf{x}) + \tilde{d}_k(\mathbf{y}_0, \mathbf{x})} \right] \\
& \cdot \exp \left[\frac{d_k(\mathbf{x})}{\sum_y o(\mathbf{y})o(\mathbf{y} + \mathbf{x})} \right] \\
& \cdot \frac{\exp[-o(\mathbf{y}_0)o(\mathbf{y}_0 + \mathbf{x})]}{\tilde{d}_k(\mathbf{y}_0, \mathbf{x})!} \left[o(\mathbf{y}_0)o(\mathbf{y}_0 + \mathbf{x}) \right]^{\tilde{d}_k(\mathbf{y}_0, \mathbf{x})} \quad (3.32)
\end{aligned}$$

This pmf is difficult to integrate in order to determine the mean. However, approximations were attempted in order to find functions easily integrable. With some reasonable approximations, this pmf may be simplified into a recognizable form where the mean may be surmised. However, these approximations led to an algorithm solution that did not properly converge. Adding a second, but related polarimetric channel, only makes this more difficult. Without a good solution for the conditional expectation of the complete data, $\mu(o^{\text{old}}, d_k(\mathbf{x}))$, the EM approach using the exponential noise model was not pursued further.

3.7 Poisson Statistics

The exponential model was unsuccessfully explored as detailed above. Therefore, a different statistical model was explored. It is known the measured autocorrelation is not corrupted by Poisson noise; however, successful algorithms have been developed based on the Poisson model for this specific problem [38, 39]. Algorithms based on the Poisson model for this type problem are reasoned to minimize the I-divergence measure for data with signal-dependent noise [38]. Both the Schulz and Snyder [38] algorithm and the Schulz and Voelz algorithm [39] demonstrate attractive properties and meaningful results. Also, the Poisson distribution is characterized only by its mean, similar to the exponential distribution. The Poisson model is again

chosen for this research. The ML phase retrieval algorithm using Poisson statistics described by Schulz and Snyder [38] is re-derived in Appendix D using an EM approach. The resulting iterative estimator for the unknown object is

$$o^{\text{new}}(\mathbf{y}_0) = \frac{o^{\text{old}}}{2S_o^{\text{new}}} \cdot \left[o^{\text{old}} \star \frac{\tilde{R}_o}{R_o^{\text{old}}} + o^{\text{old}} * \frac{\tilde{R}_o}{R_o^{\text{old}}} \right] (\mathbf{y}_0), \quad (3.33)$$

where \star is correlation, $*$ is convolution, o^{new} is the new object estimate, o^{old} is the old object estimate from the previous iteration, \tilde{R}_o is the measured autocorrelation, R_o^{old} is the autocorrelation formed from the old estimate of the object from the previous iteration, and S_o^{new} is the two-dimensional sum of the new object estimate computed by Eqn. D.15 in Appendix D.

This iterative algorithm derived via EM technique should be similar or exactly equal to the Schulz and Snyder ML algorithm [38] (see Eqn. 2.3). By inspection, the EM derived algorithm only differs from the Schulz and Snyder ML algorithm by a scale factor (see Appendix D). This result is provided here for comparison to a multi-channel approach detailed in Chapter IV.

IV. Polarimetric Algorithms

This chapter describes two EM algorithms for use with polarimetric data. A maximum likelihood estimator is formed to process polarimetric data related to the unknown object's autocorrelation. Two different system models are explored: (1) a two-channel system and (2) a dual-channel system. The difference in the system models is the polarization configuration for the two data channels. The EM technique employed here follows closely with the clear development of the generalized EM algorithm found in [37, 39].

The EM algorithm technique allows for generalized developments such as an extension to maximum a posteriori (MAP) estimators as shown by Dempster, Laird and Rubin [9]. In this chapter, the EM method is extended to a MAP approach for the two-channel system with the introduction of a prior distribution on the polarization parameter, p . Lastly, a statistical-based stopping criteria is provided for timely stopping of the iterative algorithms.

4.1 Two-Channel Algorithm

A two-channel system observes unpolarized and polarized data in two channels. Channel one produces the unpolarized data set and channel two produces the polarized data set. As presented in Chapter III, there are multiple approaches to system design to produce the polarized and unpolarized data sets. However, this correlography method requires statistical independence in the two channels, an important design consideration. The following development delineates an EM algorithm.

4.1.1 Incomplete Data Model. The incomplete data, $d_k(\mathbf{x})$, is a series of statistically independent, noisy autocorrelations of the original object transformed from laser speckle observations. With an assumption about the target scene's surface roughness, the observed laser speckle data is known to be statistically distributed as Negative Binomial due to the doubly stochastic process of speckle generation and

photoelectric detection [17]. However, the transformation of the laser speckle data into noisy autocorrelations (see Eqn. 3.1) produces entirely different statistics and can be approximated by an exponential distribution with mean equal to the true object autocorrelation (see Appendix A). The exponential model was unsuccessfully explored as detailed in Chapter III. The Poisson model is chosen for the development of a multi-channel polarimetric algorithm. This development is a polarimetric extension to the Schulz and Snyder algorithm for recovering images from correlation data [38] developed with the EM technique. The single channel, non-polarimetric variant is developed for completeness in Appendix D.

4.1.2 Complete Data Model. The complete data is postulated to be statistically independent variates, $\tilde{d}_k(\mathbf{y}, \mathbf{x})$, distributed as Poisson, related to the incomplete data and with expected values:

$$d_k^{(1)}(\mathbf{x}) = \sum_y \tilde{d}_k^{(1)}(\mathbf{y}, \mathbf{x}), \quad (4.1)$$

$$E[\tilde{d}_k^{(1)}(\mathbf{y}, \mathbf{x})] = o(\mathbf{y})o(\mathbf{y} + \mathbf{x}), \quad (4.2)$$

$$d_k^{(2)}(\mathbf{x}) = \sum_y \tilde{d}_k^{(2)}(\mathbf{y}, \mathbf{x}), \quad (4.3)$$

$$E[\tilde{d}_k^{(2)}(\mathbf{y}, \mathbf{x})] = o_p(\mathbf{y})o_p(\mathbf{y} + \mathbf{x}), \quad (4.4)$$

where $E[\cdot]$ is the expected value operator, \mathbf{x} and \mathbf{y} are two-dimensional spatial variables, o is the unknown object, o_p is the unknown polarized object as viewed through the polarization analyzer, and (1) and (2) indicate channel number. Assuming statistical independence between the two channels and each frame, the complete data log-likelihood, L_{CD} , is

$$\begin{aligned}
L_{CD}(o) = & \sum_{k=1}^K \sum_{l=1}^K \sum_x \sum_y \left\{ \tilde{d}_k^{(1)}(\mathbf{y}, \mathbf{x}) \log[o(\mathbf{y})o(\mathbf{y} + \mathbf{x})] + \tilde{d}_l^{(2)}(\mathbf{y}, \mathbf{x}) \log[o_p(\mathbf{y})o_p(\mathbf{y} + \mathbf{x})] \right. \\
& \left. - o(\mathbf{y})o(\mathbf{y} + \mathbf{x}) - o_p(\mathbf{y})o_p(\mathbf{y} + \mathbf{x}) + \text{O.T.} \right\}, \tag{4.5}
\end{aligned}$$

where k and l are independently indexed frame numbers and O.T. represents other terms not a function of o or p . These terms are eliminated in the maximization step; therefore, they are ignored.

With this formulation of the log-likelihood function, the EM solution for the unknown object o degenerates into a solution as function of the data observed only in the unpolarized channel (e.g. o^{new} is not a function of p^{new}). This degeneration of the two-channel polarimetric system also occurs in the imaging case as detailed by Strong [43]. To overcome this degenerative solution and use all of the data from both channels, Strong proposed a departure from the EM technique by using an old estimate of the polarization ratio, p^{old} , for calculating o^{new} . Strong successfully used this substitution with reasonable results but produced an algorithm no longer characterized as EM. This research explored a similar approach with satisfactory results for o ; however, the estimated values for p become non-physical and are often estimated to be much larger than one. To overcome this difficulty and maintain the EM algorithm technique, it is proposed to include a prior distribution on the polarization ratio, p , similar to the imaging case found in [26]. The introduction of the prior distribution extends the EM algorithm to a MAP estimator vice an ML estimator.

The polarization ratio is known to be positive but also less than or equal to one; however, a uniform density function (e.g. $p \sim U[0, 1]$) is not helpful. It can be reasoned that the polarization ratio of a random scene is less likely, on average, to produce a p equal to zero or one and more likely, on average, to produce a p near 0.5.

Therefore, a normal distribution, with density function $f(p)$, centered at 0.5, is an ideal prior,

$$f(p) = s \exp \left[- \left(\frac{p - 0.5}{\sigma} \right)^n \right], \quad (4.6)$$

where s is a scaling parameter, σ is an arbitrary shape parameter, and n is a positive, even integer. However, this n th order distribution adds unwanted computational complexity to the estimator. Consequently, the selection of a meaningful prior distribution must be as simple as possible to keep the problem tractable. Additionally, any algorithm development must enforce positivity for both o and p . Therefore, the simple exponential distribution with a mean, $\lambda = 1/2$, is chosen. This choice of λ is arbitrary but found to perform reasonably well. The exponential distribution with density function, $f(p)$, constrains $p > 1$ as less likely compared to $0 \leq p \leq 1$,

$$f(p; \bar{p} = \frac{1}{2}) = 2 \exp[-2p(\mathbf{y})]. \quad (4.7)$$

This distribution, while not entirely informative, does enforce positivity, and constrains large values of p to be less likely. This simple selection provides these two properties and enables analytic solutions for o and p estimates using both data channels. With this selection of a prior constraining p , the complete data log-likelihood function becomes,

$$L_{CD}(o, p) = \sum_{k=1}^K \sum_{l=1}^K \sum_x \sum_y \left\{ \tilde{d}_k^{(1)}(\mathbf{y}, \mathbf{x}) \log[o(\mathbf{y})o(\mathbf{y} + \mathbf{x})] + \tilde{d}_l^{(2)}(\mathbf{y}, \mathbf{x}) \log[o_p(\mathbf{y})o_p(\mathbf{y} + \mathbf{x})] \right. \\ \left. - o(\mathbf{y})o(\mathbf{y} + \mathbf{x}) - o_p(\mathbf{y})o_p(\mathbf{y} + \mathbf{x}) - 2p(\mathbf{y}) + \text{O.T.} \right\}. \quad (4.8)$$

4.1.3 *Expectation Step.* For the Expectation Step (E-Step), the conditional expectation of the complete log-likelihood is taken:

$$\begin{aligned}
Q(o, p) &= E[L_{CD} | d_k(\mathbf{x}), o = o^{\text{old}}, p = p^{\text{old}}] = E^{\text{old}}[L_{CD}] \\
&= \sum_{k=1}^K \sum_{l=1}^K \sum_x \sum_y \left\{ E^{\text{old}}[\tilde{d}_k^{(1)}(\mathbf{y}, \mathbf{x})] \log[o(\mathbf{y})o(\mathbf{y} + \mathbf{x})] \right. \\
&\quad + E^{\text{old}}[\tilde{d}_l^{(2)}(\mathbf{y}, \mathbf{x})] \log[o_p(\mathbf{y})o_p(\mathbf{y} + \mathbf{x})] \\
&\quad \left. - o(\mathbf{y})o(\mathbf{y} + \mathbf{x}) + o_p(\mathbf{y})o_p(\mathbf{y} + \mathbf{x}) - 2p(\mathbf{y}) \right\}. \tag{4.9}
\end{aligned}$$

The conditional expectation, E^{old} , is conditioned on the incomplete data and old estimates of the object, o , and parameter, p . The conditional expectation of the complete data is often the most difficult step of the EM process. Fortunately, by choosing the Poisson model, the form of the conditional expectation is provided by Shepp and Vardi [42],

$$\mu_1(\mathbf{y}_0, \mathbf{x}) = E^{\text{old}}[\tilde{d}_k^{(1)}(\mathbf{y}_0, \mathbf{x})] = o^{\text{old}}(\mathbf{y}_0)o^{\text{old}}(\mathbf{y}_0 + \mathbf{x}) \frac{d_k^{(1)}(\mathbf{x})}{R_o^{\text{old}}(\mathbf{x})}, \tag{4.10}$$

$$\mu_2(\mathbf{y}_0, \mathbf{x}) = E^{\text{old}}[\tilde{d}_l^{(2)}(\mathbf{y}_0, \mathbf{x})] = o_p^{\text{old}}(\mathbf{y}_0)o_p^{\text{old}}(\mathbf{y}_0 + \mathbf{x}) \frac{d_l^{(2)}(\mathbf{x})}{R_{po}^{\text{old}}(\mathbf{x})}, \tag{4.11}$$

where the autocorrelations formed by the old estimate of the objects o and o_p are

$$R_o^{\text{old}}(\mathbf{x}) = \sum_y o^{\text{old}}(\mathbf{y}) o^{\text{old}}(\mathbf{y} + \mathbf{x}), \quad (4.12)$$

$$R_{po}^{\text{old}}(\mathbf{x}) = \sum_y o_p^{\text{old}}(\mathbf{y}) o_p^{\text{old}}(\mathbf{y} + \mathbf{x}). \quad (4.13)$$

4.1.4 *Maximization Step.* The Maximization Step (M-Step) is performed by maximizing $Q(o, p)$ of Eqn. 4.9 for the unknown variates, o and p . The Q-function is maximized by finding the zero of the first partial derivatives.

$$\begin{aligned} \frac{\partial Q}{\partial o(\mathbf{y}_0)} &= \sum_{k=1}^K \sum_{l=1}^K \sum_x \left\{ \frac{\mu_1(\mathbf{y}_0, \mathbf{x})}{o(\mathbf{y}_0)} + \frac{\mu_1(\mathbf{y}_0 - \mathbf{x}, \mathbf{x})}{o(\mathbf{y}_0, \mathbf{x})} + \frac{\mu_2(\mathbf{y}_0, \mathbf{x})}{o(\mathbf{y}_0)} + \frac{\mu_2(\mathbf{y}_0 - \mathbf{x}, \mathbf{x})}{o(\mathbf{y}_0)} \right. \\ &\quad \left. - o(\mathbf{y}_0 + \mathbf{x}) - o(\mathbf{y}_0 - \mathbf{x}) - p(\mathbf{y}_0) o_p(\mathbf{y}_0 + \mathbf{x}) - p(\mathbf{y}_0) o_p(\mathbf{y}_0 - \mathbf{x}) \right\} \\ &= 0. \end{aligned} \quad (4.14)$$

Solving for $o(\mathbf{y}_0)$ yields the new estimate for o ,

$$\begin{aligned} o^{\text{new}}(\mathbf{y}_0) &= \frac{1}{2K^2 [S_o^{\text{new}} + S_{po}^{\text{new}} p^{\text{new}}(\mathbf{y}_0)]} \sum_{k=1}^K \sum_{l=1}^K \sum_x \left\{ \mu_1(\mathbf{y}_0, \mathbf{x}) + \mu_1(\mathbf{y}_0 - \mathbf{x}, \mathbf{x}) \right. \\ &\quad \left. + \mu_2(\mathbf{y}_0, \mathbf{x}) + \mu_2(\mathbf{y}_0 - \mathbf{x}, \mathbf{x}) \right\}, \end{aligned} \quad (4.15)$$

where

$$S_o^{\text{new}} = \sum_x o^{\text{new}}(\mathbf{x}), \quad (4.16)$$

$$S_{po}^{\text{new}} = \sum_x o_p^{\text{new}}(\mathbf{x}). \quad (4.17)$$

Equation 4.15 can be simplified by evaluating the summation terms:

$$o^{\text{new}}(\mathbf{y}_0) = \frac{\Psi_1(\mathbf{y}_0) + \Psi_2(\mathbf{y}_0)}{2[S_o^{\text{new}} + S_{p_o}^{\text{new}} p^{\text{new}}(\mathbf{y}_0)]}, \quad (4.18)$$

where

$$\Psi_1(\mathbf{y}_0) = o^{\text{old}} \left[o^{\text{old}} \star \frac{\tilde{R}_o}{R_o^{\text{old}}} \right] (\mathbf{y}_0) + o^{\text{old}} \left[o^{\text{old}} \star \frac{\tilde{R}_o}{R_o^{\text{old}}} \right] (\mathbf{y}_0), \quad (4.19)$$

$$\Psi_2(\mathbf{y}_0) = o_p^{\text{old}} \left[o_p^{\text{old}} \star \frac{\tilde{R}_{p_o}}{R_{p_o}^{\text{old}}} \right] (\mathbf{y}_0) + o_p^{\text{old}} \left[o_p^{\text{old}} \star \frac{\tilde{R}_{p_o}}{R_{p_o}^{\text{old}}} \right] (\mathbf{y}_0), \quad (4.20)$$

\star denotes correlation, and $*$ denotes convolution. Note, if $p = 0$ everywhere, the second channel vanishes and the above solution is equivalent to the single channel solution [38] solved via ML technique. However, if $p > 0$ for any point in the scene, the new terms assert themselves to yield the proposed multi-channel algorithm.

The solution for o^{new} is a function of the polarization ratio, p^{new} , also to be estimated. Therefore, the Q-function will be maximized for the parameter, p . This is accomplished by also finding the zero of the first partial derivative,

$$\begin{aligned} \frac{\partial Q}{\partial p(\mathbf{y}_0)} &= \sum_{k=1}^K \sum_{l=1}^K \sum_x \left\{ \frac{\mu_2(\mathbf{y}_0, \mathbf{x})}{p(\mathbf{y}_0)} + \frac{\mu_2(\mathbf{y}_0 - \mathbf{x}, \mathbf{x})}{p(\mathbf{y}_0)} - o(\mathbf{y}_0) o_p(\mathbf{y}_0 + \mathbf{x}) - o(\mathbf{y}_0) o_p(\mathbf{y}_0 - \mathbf{x}) - 2 \right\} \\ &= 0 \end{aligned} \quad (4.21)$$

Solving for $p(\mathbf{y}_0)$ yields the new estimate for p ,

$$p^{\text{new}}(\mathbf{y}_0) = \frac{\Psi_2(\mathbf{y}_0)}{2[o^{\text{new}}(\mathbf{y}_0) S_{p_o}^{\text{new}} + N]}, \quad (4.22)$$

where N is the total number of pixels in the two-dimensional spatial vector, \mathbf{x} . Plugging Eqn. 4.22 back into Eq. 4.18 yields a quadratic equation from which the positive root is selected. This provides the final equation for estimating o^{new} ,

$$o^{\text{new}}(\mathbf{y}_0) = \frac{S_{po}^{\text{new}}\Psi_1 - 2NS_o^{\text{new}} + [(2NS_o^{\text{new}} - S_{po}^{\text{new}}\Psi_1)^2 + 8NS_o^{\text{new}}S_{po}^{\text{new}}(\Psi_1 + \Psi_2)]^{1/2}}{4S_o^{\text{new}}S_{po}^{\text{new}}}. \quad (4.23)$$

The estimate for o^{new} is a function of old estimates and the data in both polarized and unpolarized channels. To form this estimate, both the scaling constants S_o^{new} and S_{po}^{new} must be computed. First, $Q(o, p)$ is maximized for o_p in order to find the sum of the new polarized object estimate, S_{po}^{new} ,

$$\begin{aligned} \frac{\partial Q}{\partial o_p(\mathbf{y}_0)} &= \sum_{k=1}^K \sum_{l=1}^K \sum_x \left\{ \frac{\mu_2(\mathbf{y}_0, \mathbf{x})}{o_p(\mathbf{y}_0)} + \frac{\mu_2(\mathbf{y}_0 - \mathbf{x}, \mathbf{x})}{o_p(\mathbf{y}_0)} - o_p(\mathbf{y}_0 + \mathbf{x}) - o_p(\mathbf{y}_0 - \mathbf{x}) \right\} \\ &= 0. \end{aligned} \quad (4.24)$$

Solving this equation for S_{po}^{new} and summing both sides of the equation yields a solution for the scaling factor as a function of old estimates and the data in the polarized channel,

$$S_{po}^{\text{new}} = \left[\frac{1}{2} \sum_{y_0} \Psi_2(\mathbf{y}_0) \right]^{1/2}. \quad (4.25)$$

Finally, the sum of the new object estimate, S_o^{new} , is solved for by summing both sides of Eqn. 4.18,

$$S_o^{\text{new}} = \left[\frac{1}{2} \sum_{y_0} [\Psi_1(\mathbf{y}_0) + \Psi_2(\mathbf{y}_0)] - (S_{po}^{\text{new}})^2 \right]^{1/2}. \quad (4.26)$$

4.2 Dual-Channel Algorithm

In this section, a dual-channel, EM algorithm is considered. A dual-channel system observes polarized data in two orthogonal channels. Employing a PBS in a non-imaging LADAR system provides two channels of orthogonally polarized data. A PBS may provide polarized data with minimal light loss as compared to traditional polarizers. Also, this correlography method requires statistical independence in the two data channels to be completely effective; a requirement aided by engineering a system with a PBS.

4.2.1 Incomplete Data Model. The incomplete data is the observed data with the object obscured by noise and detection limitations. The incomplete data, $d_k^{(1)}(\mathbf{x})$ and $d_l^{(2)}(\mathbf{x})$, is a set of statistically independent, noisy autocorrelations of the polarized object transformed from laser speckle observations. The Poisson noise model is again chosen; identical to the two-channel algorithm with the same rationale. The expected value of the incomplete data is modeled as autocorrelation of the polarized object.

$$E[d_k^{(1)}(\mathbf{x})] = \sum_y o_{p1}(\mathbf{y})o_{p1}(\mathbf{y} + \mathbf{x}) \quad (4.27)$$

$$E[d_l^{(2)}(\mathbf{x})] = \sum_y o_{p2}(\mathbf{y})o_{p2}(\mathbf{y} + \mathbf{x}) \quad (4.28)$$

4.2.2 Complete Data Model. The complete data is postulated to be statistically independent variates, $\tilde{d}_k(\mathbf{y}, \mathbf{x})$, distributed as Poisson, related to the incomplete data and with expected values:

$$d_k^{(1)}(\mathbf{x}) = \sum_y \tilde{d}_k^{(1)}(\mathbf{y}, \mathbf{x}), \quad (4.29)$$

$$E[\tilde{d}_k^{(1)}(\mathbf{y}, \mathbf{x})] = o_{p1}(\mathbf{y})o_{p1}(\mathbf{y} + \mathbf{x}), \quad (4.30)$$

$$d_l^{(2)}(\mathbf{x}) = \sum_y \tilde{d}_l^{(2)}(\mathbf{y}, \mathbf{x}), \quad (4.31)$$

$$E[\tilde{d}_l^{(2)}(\mathbf{y}, \mathbf{x})] = o_{p2}(\mathbf{y})o_{p2}(\mathbf{y} + \mathbf{x}). \quad (4.32)$$

Assuming statistical independence between the two channels and each frame, the complete data log-likelihood, L_{CD} , is

$$\begin{aligned} L_{CD}(o) = & \sum_{k=1}^K \sum_{l=1}^K \sum_x \sum_y \{ \tilde{d}_k^{(1)}(\mathbf{y}, \mathbf{x}) \log[o_{p1}(\mathbf{y})o_{p1}(\mathbf{y} + \mathbf{x})] + \tilde{d}_l^{(2)}(\mathbf{y}, \mathbf{x}) \log[o_{p2}(\mathbf{y})o_{p2}(\mathbf{y} + \mathbf{x})] \\ & - o_{p1}(\mathbf{y})o_{p1}(\mathbf{y} + \mathbf{x}) - o_{p2}(\mathbf{y})o_{p2}(\mathbf{y} + \mathbf{x}) + \text{O.T.} \}, \end{aligned} \quad (4.33)$$

where O.T. represents other terms not a function of o or p . These terms are eliminated in the M-Step; therefore, are ignored.

In the two-channel case, a prior distribution on p was introduced to avoid a degenerate solution. However, with the dual-channel case, a prior distribution is not required. A closed-form solution for o and p is calculated without deviating from the EM methodology. Considering orthogonality of the two channel data, the development simplifies the number of unknowns. Because the polarization response in channel one is orthogonal to the polarization response in channel two, the polarization ratios of the two channels are related by:

$$p_2(\mathbf{y}) = 1 - p_1(\mathbf{y}). \quad (4.34)$$

This permits the dropping of the channel subscript for the polarization ratio in subsequent equations and simplifies the polarized object model:

$$o_{p1}(\mathbf{y}) = p(\mathbf{y})o(\mathbf{y}), \quad (4.35)$$

$$o_{p2}(\mathbf{y}) = [1 - p(\mathbf{y})]o(\mathbf{y}). \quad (4.36)$$

4.2.3 Expectation Step. For the Expectation Step, the conditional expectation of the complete log-likelihood is taken:

$$\begin{aligned} Q(o, p) &= E[L_{CD} | d_k(\mathbf{x}), o = o^{\text{old}}, p = p^{\text{old}}] = E^{\text{old}}[L_{CD}] \\ &= \sum_{k=1}^K \sum_{l=1}^K \sum_x \sum_y \left\{ E^{\text{old}}[\tilde{d}_k^{(1)}(\mathbf{y}, \mathbf{x})] \log[o_{p1}(\mathbf{y})o_{p1}(\mathbf{y} + \mathbf{x})] \right. \\ &\quad + E^{\text{old}}[\tilde{d}_l^{(2)}(\mathbf{y}, \mathbf{x})] \log[o_{p2}(\mathbf{y})o_{p2}(\mathbf{y} + \mathbf{x})] \\ &\quad \left. - o_{p1}(\mathbf{y})o_{p1}(\mathbf{y} + \mathbf{x}) + o_{p2}(\mathbf{y})o_{p2}(\mathbf{y} + \mathbf{x}) \right\}. \end{aligned} \quad (4.37)$$

The conditional expectation, E^{old} , is conditioned on the incomplete data and old estimates of the object, o , and parameter, p . By choosing the Poisson model, the form of the conditional expectation is known,

$$\mu_1(\mathbf{y}_0, \mathbf{x}) = E^{\text{old}}[\tilde{d}_k^{(1)}(\mathbf{y}_0, \mathbf{x})] = o_{p1}^{\text{old}}(\mathbf{y}_0)o_{p1}^{\text{old}}(\mathbf{y}_0 + \mathbf{x}) \frac{d_k^{(1)}(\mathbf{x})}{R_{op1}^{\text{old}}(\mathbf{x})}, \quad (4.38)$$

$$\mu_2(\mathbf{y}_0, \mathbf{x}) = E^{\text{old}}[\tilde{d}_l^{(2)}(\mathbf{y}_0, \mathbf{x})] = o_{p2}^{\text{old}}(\mathbf{y}_0) o_{p2}^{\text{old}}(\mathbf{y}_0 + \mathbf{x}) \frac{d_l^{(2)}(\mathbf{x})}{R_{op2}^{\text{old}}(\mathbf{x})}, \quad (4.39)$$

where the autocorrelations formed by the old estimate of the polarized objects, o_{p1} and o_{p2} , are

$$R_{op1}^{\text{old}}(\mathbf{x}) = \sum_y o_{p1}^{\text{old}}(\mathbf{y}) o_{p2}^{\text{old}}(\mathbf{y} + \mathbf{x}), \quad (4.40)$$

$$R_{op2}^{\text{old}}(\mathbf{x}) = \sum_y o_{p2}^{\text{old}}(\mathbf{y}) o_{p2}^{\text{old}}(\mathbf{y} + \mathbf{x}). \quad (4.41)$$

4.2.4 Maximization Step. Again, the Maximization Step is performed by maximizing $Q(o, p)$ of Eqn. 4.37 for the unknown variates, o and p . The Q-function is maximized by finding the zero of the first partial derivatives.

$$\begin{aligned} \frac{\partial Q}{\partial o(\mathbf{y}_0)} &= \sum_{k=1}^K \sum_{l=1}^K \sum_x \left\{ \frac{\mu_1(\mathbf{y}_0, \mathbf{x})}{o(\mathbf{y}_0)} + \frac{\mu_1(\mathbf{y}_0 - \mathbf{x}, \mathbf{x})}{o(\mathbf{y}_0)} + \frac{\mu_2(\mathbf{y}_0, \mathbf{x})}{o(\mathbf{y}_0)} + \frac{\mu_2(\mathbf{y}_0 - \mathbf{x}, \mathbf{x})}{o(\mathbf{y}_0)} \right. \\ &\quad \left. - 2p(\mathbf{y}_0)p(\mathbf{y}_0 + \mathbf{x})o(\mathbf{y}_0 + \mathbf{x}) - 2[1 - p(\mathbf{y}_0)][1 - p(\mathbf{y}_0 + \mathbf{x})]o(\mathbf{y}_0 + \mathbf{x}) \right\} \\ &= 0. \end{aligned} \quad (4.42)$$

Solving for $o(\mathbf{y}_0)$ yields the new estimate for o ,

$$\begin{aligned} o^{\text{new}}(\mathbf{y}_0) &= \frac{1}{2K^2 [p^{\text{new}}(\mathbf{y}_0) S_{op1}^{\text{new}} + [1 - p^{\text{new}}(\mathbf{y}_0)] S_{op2}^{\text{new}}]} \sum_{k=1}^K \sum_{l=1}^K \sum_x \left\{ \mu_1(\mathbf{y}_0, \mathbf{x}) + \mu_1(\mathbf{y}_0 - \mathbf{x}, \mathbf{x}) \right. \\ &\quad \left. + \mu_2(\mathbf{y}_0, \mathbf{x}) + \mu_2(\mathbf{y}_0 - \mathbf{x}, \mathbf{x}) \right\}, \end{aligned} \quad (4.43)$$

where

$$S_{op1}^{\text{new}} = \sum_x o_{p1}^{\text{new}}(\mathbf{y}), \quad (4.44)$$

$$S_{op2}^{\text{new}} = \sum_x o_{p2}^{\text{new}}(\mathbf{y}). \quad (4.45)$$

Equation 4.43 can be simplified by evaluating the summation terms:

$$o^{\text{new}}(\mathbf{y}_0) = \frac{\Psi_1(\mathbf{y}_0) + \Psi_2(\mathbf{y}_0)}{2[p^{\text{new}}(\mathbf{y}_0)S_{op1}^{\text{new}} + [1 - p^{\text{new}}(\mathbf{y}_0)]S_{op2}^{\text{new}}]}, \quad (4.46)$$

where

$$\Psi_1(\mathbf{y}_0) = o_{p1}^{\text{old}} \left[o_{p1}^{\text{old}} \star \frac{\tilde{R}_{op1}}{R_{op1}^{\text{old}}} \right] (\mathbf{y}_0) + o_{p1}^{\text{old}} \left[o_{p1}^{\text{old}} \star \frac{\tilde{R}_{op1}}{R_{op1}^{\text{old}}} \right] (\mathbf{y}_0), \quad (4.47)$$

$$\Psi_2(\mathbf{y}_0) = o_{p2}^{\text{old}} \left[o_{p2}^{\text{old}} \star \frac{\tilde{R}_{op2}}{R_{op2}^{\text{old}}} \right] (\mathbf{y}_0) + o_{p2}^{\text{old}} \left[o_{p2}^{\text{old}} \star \frac{\tilde{R}_{op2}}{R_{op2}^{\text{old}}} \right] (\mathbf{y}_0). \quad (4.48)$$

\tilde{R}_{op1} and \tilde{R}_{op2} are the measured autocorrelations obtained from the observed data in channels one and two, respectively, This definition was first described in Chapter III.

$$\tilde{R}_{op1} = K^{-1} \sum_{k=1}^K d_k^{(1)}(\mathbf{x}) [1 - \delta(\mathbf{x})] + \sum_{y=1}^N [o_{p1}^{\text{old}}(\mathbf{y})]^2 \delta(\mathbf{x}) \quad (4.49)$$

$$\tilde{R}_{op2} = K^{-1} \sum_{l=1}^K d_l^{(2)}(\mathbf{x}) [1 - \delta(\mathbf{x})] + \sum_{y=1}^N [o_{p2}^{\text{old}}(\mathbf{y})]^2 \delta(\mathbf{x}) \quad (4.50)$$

$p^{\text{new}}(\mathbf{y})$ is estimated by maximizing the Q-function with respect to the p parameter.

$$\begin{aligned}
\frac{\partial Q}{\partial p(\mathbf{y}_0)} &= \sum_{k=1}^K \sum_{l=1}^K \sum_x \left\{ \frac{\mu_1(\mathbf{y}_0, \mathbf{x})}{p(\mathbf{y}_0)} + \frac{\mu_1(\mathbf{y}_0 - \mathbf{x}, \mathbf{x})}{p(\mathbf{y}_0)} + \frac{\mu_2(\mathbf{y}_0, \mathbf{x})}{1 - p(\mathbf{y}_0)} + \frac{\mu_2(\mathbf{y}_0 - \mathbf{x}, \mathbf{x})}{1 - p(\mathbf{y}_0)} \right. \\
&\quad \left. - 2o(\mathbf{y}_0)o_{p1}(\mathbf{y}_0 + \mathbf{x}) + 2o(\mathbf{y}_0)o_{p2}(\mathbf{y}_0) \right\} \\
&= 0.
\end{aligned} \tag{4.51}$$

Substituting in the solution for o^{new} from Eqn. 4.46 and solving for p^{new} produces a quadratic equation with the following roots:

$$p^{\text{new}}(\mathbf{y}_0) = \frac{B(\mathbf{y}_0) + \Psi_1 + \Psi_2 \pm \sqrt{[\Psi_1 + \Psi_2 + B(\mathbf{y}_0)]^2 - 4B(\mathbf{y}_0)\Psi_1}}{2B(\mathbf{y}_0)}, \tag{4.52}$$

where

$$B(\mathbf{y}_0) = 2[S_{op1}^{\text{new}} - S_{op2}^{\text{new}}]o^{\text{new}}(\mathbf{y}_0). \tag{4.53}$$

The smallest (or positive) root is chosen when computing the estimate for p^{new} . The sum of the estimated polarized objects, S_{op1}^{new} and S_{op2}^{new} (see Eqns. 4.44 and 4.45) are unknown but easily computed by the same maximization method:

$$S_{op1}^{\text{new}} = \left[\frac{1}{2} \sum_{y_0} \Psi_1(\mathbf{y}_0) \right]^{1/2}, \tag{4.54}$$

$$S_{op2}^{\text{new}} = \left[\frac{1}{2} \sum_{y_0} \Psi_2(\mathbf{y}_0) \right]^{1/2}. \tag{4.55}$$

Finally, a solution is found for o^{new} using the above expressions for p^{new} , S_{op1}^{new} , and S_{op2}^{new} and plugging them into Eqn 4.46. While this is a complex equation, it is

easily reduced using symbolic mathematical solver software such as Mathematica[®] or MATLAB[®]. The resulting estimate for the object is surprisingly familiar:

$$o^{\text{new}}(\mathbf{y}_0) = \frac{\Psi_1(\mathbf{y}_0)}{2S_{op1}} + \frac{\Psi_2(\mathbf{y}_0)}{2S_{op2}}. \quad (4.56)$$

Note the estimator is the average of two separate estimates formed from each channel. The estimator for each channel is of identical form of the single channel, unpolarized algorithm (see Appendix D). Essentially, two phase retrieval estimates are formed and averaged or fused together with equal weighting. Because autocorrelations are symmetric (e.g. $R_f(\mathbf{x}) = R_f(-\mathbf{x})$), solutions include estimates related by translation and 180° rotation. Therefore, fusion of two similar estimates may require additional registration or alignment steps.

4.3 Algorithm Computation

In order to initialize this iterative algorithm, an initial guess for the unknown object and polarization ratio is chosen. Normally, the spatial bound of the object is known *a priori* or estimated from the spatial extent of the illuminating beam. Also, the object is positive and the LADAR system produces a measured autocorrelation. Therefore, the initial object guess is chosen with the following conditions: (1) known support region or spatial bound $[\Omega : o^{\text{old}}(\mathbf{x}) = 0 \forall \mathbf{x} \ni \Omega]$, (2) strictly positive, $[o^{\text{old}}(\mathbf{x}) > 0 \forall \mathbf{x} \in \Omega]$, and (3) average value, A , computed from the measured autocorrelation,

$$A = N^{-1} \left[\sum_{x=1}^N \tilde{R}_o(\mathbf{x}) \right]^{1/2}. \quad (4.57)$$

Therefore, the initial object guess $[o^{\text{old}}(\mathbf{x}) : \mathbf{x} \in \Omega]$ is selected as independent random variables distributed uniformly over the interval $[A - 0.1, A + 0.1]$. The initial guess

for the polarization ratio is chosen to be uniformly equal to $1/2$ within the support region; [$p^{\text{old}}(\mathbf{x}) = 0.5 \forall \mathbf{x} \in \Omega$].

4.4 Stopping Criteria

With all iterative algorithms, knowing when to stop is an operationally compelling capability. Often, algorithms are allowed to run for a specified number of iterations or as long as operational time permits if for each successive iteration, the subsequent estimate error is known to be less than the previous estimate error. In some cases, noise amplification occurs and the estimated solution diverges if the algorithm is permitted to iterate too long. From simulation and experimental results with exponential noise, both the two-channel, polarimetric phase retrieval algorithm presented here and Schulz and Snyder’s single channel phase retrieval algorithm [38] diverge due to noise amplification after too many iterations. Even with the noise amplification, the Poisson model offers attractive properties as detailed in Refs. [38, 39] and produces satisfactory object estimates with the optimal number of iterations.

Throughout the literature, few algorithms are presented with stopping criteria based on the statistical properties of the data. However, Phillips provides a simple and compelling approach to this problem [33]. Phillips proposes a dampening routine based on the statistics of the data by comparing the variance of the predicted object to the variance of the data for each subsequent iteration such that

$$K^{-1} \sum_{k=1}^K [d_k(\mathbf{x}) - R_o^{\text{old}}(\mathbf{x})]^2 < \beta \cdot s^2(\mathbf{x}), \quad (4.58)$$

where $\beta \in \{\mathbb{R} > 1\}$ is a user chosen parameter determining the degree of dampening and s^2 is the sample variance computed from the observed data. If the variance of the predicted object is within the variance of the observed data, the pixel should be damped by setting the ratio of the measured object autocorrelation to the estimated object autocorrelation equal to one,

$$\frac{\tilde{R}_o(\mathbf{x})}{R_o^{\text{old}}(\mathbf{x})} \mapsto 1. \quad (4.59)$$

The algorithm is then allowed to iterate as long as operationally feasible. Phillips did not propose a method for selecting the optimal β as this parameter is data dependent. When applying the pixel dampening criteria for this problem with exponential noise, divergence still occurred after the optimal iteration number was exceeded. Therefore, a global stopping criteria was selected to achieve the iteration number near the optimal number in terms of mean-square error. If the criteria found in Eqn. 4.58 is reached on average throughout the entire data image, the algorithm is stopped. Selecting $[1.01 < \beta < 1.3]$ produced satisfactory results for the simulated data set.

$$(N \cdot K)^{-1} \sum_{x=1}^N \sum_{k=1}^K [d_k(\mathbf{x}) - R_o^{\text{old}}(\mathbf{x})]^2 < \beta \cdot \sum_x \sigma^2(\mathbf{x}) \quad (4.60)$$

Summary

This chapter provided a detailed development for two new phase retrieval algorithms for the correlography problem presented in Chapter II. Employing the EM method and using the Poisson noise model and a polarimetric data model two iterative phase retrieval algorithms were developed. Both MAP and ML methods were presented as well as computational considerations. Finally, a statistically based stopping criteria was detailed.

V. *Cramer-Rao Lower Bound on Spatial Resolution*

This chapter provides a statistical analysis of the theoretical bound on resolution for reconstructed images computed in the phase retrieval problem presented in this research. A statistical model is presented along with a simplistic object model. It is often postulated how well a particular approach performs as compared to another. A theoretical bound, independent of the computational algorithm used is a measure of “best” possible performance given the underlying measurements and data statistics. The Cramer-Rao Lower Bound (CRLB) is often used as a such a measure. The CRLB provides a lower bound on the error covariance matrix for any unbiased estimator [36].

Of interest with image reconstruction is how well the image reconstructed compares to the original. An analysis of phase-retrieval error is provided by Cederquist and Wackerman [5], with Gaussian noise statistics assumed. Here the variance of the estimate of object intensity is bounded, not resolution. In addition to overall reconstruction error, resolution or differentiation of image detail is often measured or studied. Resolution measures how well two distinct but adjacent objects or sources may be individually distinguishable [8, 22].

A theoretical bound on resolution for a lens-based imaging system was presented by Shahram and Milanfar [41]. Shahram and Milanfar used a two point source model for demonstrating resolution. Strong provided a similar theoretical bound for imaging resolution using a two point source model and polarimetric data [43]. In this research, a similar approach is applied to the non-imaging, correlography case. A theoretical resolution bound is developed for three cases: (1) a single channel, unpolarized system, (2) a two-channel, polarimetric system, and (3) a dual-channel polarimetric system. The second and third cases will be compared to the first case in order describe the improvement in performance with the addition of polarization diversity in the remote sensor system.

5.1 Object Model

The object, o , consists of two point sources separated by an unknown distance, Δ . The viewing of this simple object's autocorrelation function is blurred by a known point spread function (PSF) defined by the observing aperture. The two-dimensional object geometry considered here is manipulated in one dimension to simplify analysis and computation as well as maintain a well-conditioned problem. The number of nuisance parameters are minimized. Adding additional, unknown nuisance parameters (e.g. spatial location and brightness) only increases the error bound [36]. Thus, a lower bound is computed when the number of parameters is minimized. Figure 5.1 depicts the geometry of the object model.

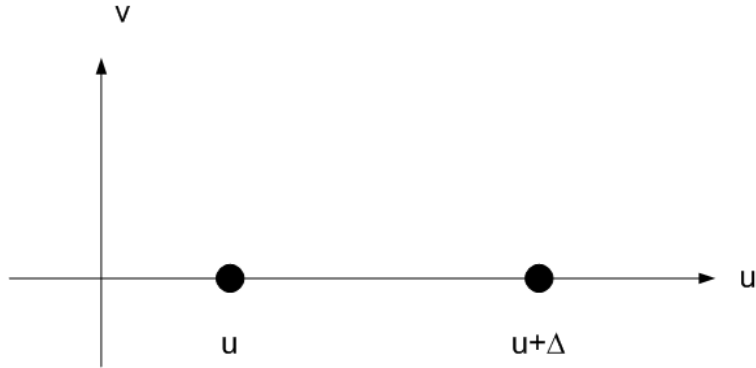


Figure 5.1: Two Point Source Object Model Geometry

The object model is mathematically described by,

$$o(u, v) = o_1\delta(u) + o_2\delta(u - \Delta), \quad (5.1)$$

where $\delta(u)$ is the Dirac delta function. For this development, it is assumed the point source intensities are equal, $o_1 = o_2$ with different polarization characteristics. This development is easily extended to a more complex case where the point sources are unknown and unequal; more unknowns to be estimated and a larger Fisher Information matrix. However, this increases the number of nuisance parameters and moves this towards an ill-conditioned problem; especially when polarization is considered.

Problem stabilization, or regularization, must be introduced to overcome the under-determined nature of the problem or the Fisher Information (FI) matrix becomes non-invertible. For computational algorithms, this is overcome in practice with the introduction of *a priori* information such as object constraints (positivity, spatial bound, etc.) as described in Chapter II. For the theoretical bound computation in this development, the problem is kept relatively well-conditioned by limiting the number of nuisance parameters in the FI matrix.

This simple, two-point object model would not physically create laser speckle at the observation plane as a large number of scatterers are required to create the speckle phenomenon. However, this object model is identical to the framework established in the imaging case [41, 43]. Also, this theoretical development employs the statistical model described in Chapter III. This simple, two point source, model is repeated here for the purpose of showing relative improvement provided by adding polarization diversity. With demonstrated improvement using polarization diversity in the simple case, it is postulated the improvement is similarly obtained in the case of a complex object with large number of polarization diverse scatterers.

The autocorrelation of this object, blurred by a known PSF and corrupted with exponential noise, is used to depict a theoretical resolution bound with and without polarization. In the correlography case, the PSF is known with no atmospheric corruption observed (see Chapter 1.2.2). However, the PSF does limit the resolution of the estimated object as only a spatially limited and discrete sample of the speckle intensity is collected. The detection array is modeled with a square, uniform aperture with width, S , or equivalently a rectangular (*rect*) function,

$$\text{rect}\left(\frac{\mathbf{v}}{S}\right) = \begin{cases} 0, & |\mathbf{v}| > \frac{S}{2}, \\ \frac{1}{2}, & |\mathbf{v}| = \frac{S}{2}, \\ 1, & |\mathbf{v}| < \frac{S}{2}, \end{cases} \quad (5.2)$$

where \mathbf{v} is the two-dimensional coordinate vector in the detector plane. Without additional corruption such as atmospheric distortion, the PSF of the detector array, $g(\mathbf{x})$, is the Fourier transform of the array aperture function, $A(\mathbf{v})$, magnitude squared,

$$\begin{aligned} g(\mathbf{x}) &= |\mathcal{F}\{A(\mathbf{v})\}|^2 \\ &= S^2 \text{sinc}^2\left(\frac{S\mathbf{t}}{2}\right), \end{aligned} \quad (5.3)$$

where \mathcal{F} represents the two-dimensional Fourier Transform and \mathbf{x} and \mathbf{v} are two-dimensional coordinate vectors.

Let $d_k(\mathbf{x})$ denote the k th frame of observed data (a single autocorrelation corrupted by exponential noise). The expected value, $R_o(\mathbf{x})$, of the observed data will be the autocorrelation of the object convolved with the PSF, g :

$$\begin{aligned} R_o(\mathbf{x}) &= \iint_{-\infty}^{\infty} o(\mathbf{u})o(\mathbf{v} + \mathbf{u})g(\mathbf{x} - \mathbf{v})d\mathbf{u}d\mathbf{v}, \\ &= \iint_{-\infty}^{\infty} [o_1\delta(\mathbf{u}) + o_2\delta(\mathbf{u} - \Delta)] [o_1\delta(\mathbf{v} + \mathbf{u}) + o_2\delta(\mathbf{v} + \mathbf{u} - \Delta)] g(\mathbf{x} - \mathbf{v})d\mathbf{u}d\mathbf{v} \\ &= (o_1^2 + o_2^2)g(\mathbf{x}) + o_1o_2 [g(\mathbf{x} - \Delta) + g(\mathbf{x} + \Delta)]. \end{aligned} \quad (5.4)$$

It is assumed each noisy autocorrelation frame is statistically independent and the noise in each frame is statistically independent at every sampled data point. Therefore, the joint probability density function is formed and detailed as

$$P[d_1(\mathbf{x}), \dots, d_K(\mathbf{x})] = \prod_k \prod_x \frac{1}{R_o(\mathbf{x})} \exp\left[\frac{-d_k(\mathbf{x})}{R_o(\mathbf{x})}\right]. \quad (5.5)$$

5.2 Resolution Criterion

Resolution criterion must be defined in order to draw any meaningful conclusions or make reasonable comparisons. “Two-point resolution, which is defined as the system’s ability to resolve two point sources of equal intensity, is a widely used measure of the overall resolving capabilities of an imaging system [8].” Using statistical analysis, the two-point resolution model is adopted here.

Let σ_{Δ}^2 denote the lower bound on the mean-squared error for any unbiased estimator of Δ . Equivalently, σ_{Δ} is the lower bound on standard deviation, or root mean square deviation, for an unbiased estimator. For this research, two closely-spaced point sources are considered resolved (e.g. distinguishable from a single point) if the separation, Δ , is greater than one standard deviation, σ_{Δ} , of the estimate error:

$$\Delta > \sigma_{\Delta}. \tag{5.6}$$

If the two points are separated by less than one standard deviation, the uncertainty of the estimate is large. In this case, the uncertainty of the estimated separation, on average, tends larger than or approximates the actual separation. If the two points are separated by greater than one standard deviation of estimate error, the uncertainty of the estimate, on average, tends to be much less than the actual separation. This criterion appears somewhat arbitrary: two standard deviations could reasonably be chosen. However, this criterion is selected for comparing correlography systems with and without polarization. This criterion is identical to the imaging case found in Strong [43].

5.3 Bound for Single, Unpolarized Channel

First, a CRLB is computed for a single-channel, unpolarized system. For computing the lower bound, consider the case where $o_1 = o_2$. The data, $d_k(\mathbf{x})$, is observed

without a polarizing reference or analyzer. The log-likelihood function, L , is detailed as

$$L(\Delta, o_1) = \sum_k \sum_x \left[-\ln R_o(\mathbf{x}) - \frac{d_k(\mathbf{x})}{R_o(\mathbf{x})} \right]. \quad (5.7)$$

The FI matrix, J , is calculated by

$$J_{ij} = -E \left[\frac{\partial^2 L}{\partial L_i \partial L_j} \right], \quad (5.8)$$

where $E[\cdot]$ is the Expected Value operator. Evaluating Eqn. 5.8 yields:

$$\begin{aligned} J_{ij} &= -E \left[\frac{\partial}{\partial L_i} \frac{\partial}{\partial L_j} \sum_k \sum_x \left[-\ln R_o(\mathbf{x}) - \frac{d_k(\mathbf{x})}{R_o(\mathbf{x})} \right] \right] \\ &= -E \left[\frac{\partial}{\partial L_i} \left[-K \sum_x \frac{1}{R_o(\mathbf{x})} \frac{\partial R_o(\mathbf{x})}{\partial L_j} + \sum_k \sum_x \frac{d_k(\mathbf{x})}{R_o^2(\mathbf{x})} \frac{\partial R_o(\mathbf{x})}{\partial L_j} \right] \right] \\ &= -E \left[K \sum_x \left[\frac{1}{R_o^2(\mathbf{x})} \frac{\partial R_o(\mathbf{x})}{\partial L_i} \frac{\partial R_o(\mathbf{x})}{\partial L_j} - \frac{1}{R_o(\mathbf{x})} \frac{\partial^2 R_o(\mathbf{x})}{\partial L_i \partial L_j} \right] \right. \\ &\quad \left. + \sum_k \sum_x \left[\frac{-2d_k(\mathbf{x})}{R_o^3(\mathbf{x})} \frac{\partial R_o(\mathbf{x})}{\partial L_i} \frac{\partial R_o(\mathbf{x})}{\partial L_j} + \frac{d_k(\mathbf{x})}{R_o^2(\mathbf{x})} \frac{\partial^2 R_o(\mathbf{x})}{\partial L_i \partial L_j} \right] \right] \\ &= \left[K \sum_x \left[\frac{-1}{R_o^2(\mathbf{x})} \frac{\partial R_o(\mathbf{x})}{\partial L_i} \frac{\partial R_o(\mathbf{x})}{\partial L_j} + \frac{1}{R_o(\mathbf{x})} \frac{\partial^2 R_o(\mathbf{x})}{\partial L_i \partial L_j} \right] \right. \\ &\quad \left. + \sum_k \sum_x \left[\frac{2R_o(\mathbf{x})}{R_o^3(\mathbf{x})} \frac{\partial R_o(\mathbf{x})}{\partial L_i} \frac{\partial R_o(\mathbf{x})}{\partial L_j} - \frac{R_o(\mathbf{x})}{R_o^2(\mathbf{x})} \frac{\partial^2 R_o(\mathbf{x})}{\partial L_i \partial L_j} \right] \right] \\ &= K \sum_x \frac{1}{R_o^2(\mathbf{x})} \frac{\partial R_o(\mathbf{x})}{\partial L_i} \frac{\partial R_o(\mathbf{x})}{\partial L_j}. \quad (5.9) \end{aligned}$$

Evaluating the partial derivatives of the autocorrelation

$$\begin{aligned}
\frac{\partial R_o(\mathbf{x})}{\partial \Delta} &= \frac{\partial}{\partial \Delta} \left\{ 2o_1^2 g(\mathbf{x}) + o_1^2 (g(\mathbf{x} - \Delta) + g(\mathbf{x} + \Delta)) \right\} \\
&= o_1^2 \left[\frac{d}{d\mathbf{x}} g(\mathbf{x} + \Delta) - \frac{d}{d\mathbf{x}} g(\mathbf{x} - \Delta) \right]
\end{aligned} \tag{5.10}$$

$$\begin{aligned}
\frac{\partial R_o(\mathbf{x})}{\partial o_1} &= \frac{\partial}{\partial o_1} \left\{ 2o_1^2 g(\mathbf{x}) + o_1^2 (g(\mathbf{x} - \Delta) + g(\mathbf{x} + \Delta)) \right\} \\
&= 4o_1 g(\mathbf{x}) + 2o_1 [g(\mathbf{x} - \Delta) + g(\mathbf{x} + \Delta)]
\end{aligned} \tag{5.11}$$

As stated previously, the bound with point source intensity $o_1 = o_2$ is computed. In this case, one must jointly estimate two parameters: Δ and o_1 . This produces a 2×2 Fisher Information matrix. Because this is an ill-posed problem, there are multiple solutions possible and the Fisher Information matrix may be ill-conditioned. Adding more than four unknowns causes the Fisher Information matrix to be highly ill-conditioned and approach singularity. The math is easily extended to more unknowns (e.g. $o_1 \neq o_2$, two-dimensional separation); however, the addition of nuisance parameters when including polarization produces a highly ill-conditioned matrix where its inverse is not meaningful. Throughout this development, to include comparison to cases with polarization, the Fisher Information matrix is kept as small as possible to create a reasonably conditioned matrix. Computing the elements of the Fisher Information matrix yields the following:

$$\begin{aligned}
J_{\Delta\Delta} &= K \sum_x \frac{1}{R_o^2(\mathbf{x})} \left(\frac{\partial R_o(\mathbf{x})}{\partial \Delta} \right)^2 \\
&= K \sum_x \frac{o_1^4}{R_o^2(\mathbf{x})} \left[\frac{d}{d\mathbf{x}} g(\mathbf{x} + \Delta) - \frac{d}{d\mathbf{x}} g(\mathbf{x} - \Delta) \right]^2
\end{aligned} \tag{5.12}$$

$$\begin{aligned}
J_{o_1 o_1} &= K \sum_x \frac{1}{R_o^2(\mathbf{x})} \left(\frac{\partial R_o(\mathbf{x})}{\partial o_1} \right)^2 \\
&= K \sum_x \frac{1}{R_o^2(\mathbf{x})} \left[4o_1 g(\mathbf{x}) + 2o_1 [g(\mathbf{x} - \Delta) + g(\mathbf{x} + \Delta)] \right]^2 \\
J_{\Delta o_1} &= K \sum_x \frac{1}{R_o^2(\mathbf{x})} \frac{\partial R_o(\mathbf{x})}{\partial o_1} \frac{\partial R_o(\mathbf{x})}{\partial \Delta} \\
&= K \sum_x \frac{1}{R_o^2(\mathbf{x})} \left\{ 4o_1^3 g(\mathbf{x}) [g'(\mathbf{x} + \Delta) - g'(\mathbf{x} - \Delta)] \right. \\
&\quad \left. + 2o_1^3 [g(\mathbf{x} - \Delta) + g(\mathbf{x} + \Delta)] \left[g'(\mathbf{x} + \Delta) - g'(\mathbf{x} - \Delta) \right] \right\}
\end{aligned} \tag{5.13}$$

$$J_{o_1 \Delta} = J_{\Delta o_1} \tag{5.14}$$

The Fisher Information matrix is constructed as

$$J = \begin{bmatrix} J_{\Delta\Delta} & J_{\Delta o_1} \\ J_{o_1 \Delta} & J_{o_1 o_1} \end{bmatrix}. \tag{5.15}$$

The lower bound on the error Covariance matrix, \mathbf{C} , is found by taking the inverse of the Fisher Information matrix:

$$\mathbf{C} \geq \mathbf{J}^{-1}, \tag{5.16}$$

and the CRLB for the separation parameter, Δ , is [36]

$$\sigma_{\Delta}^2 \geq \left[\mathbf{J}^{-1} \right]_{(1,1)}. \quad (5.17)$$

The two point sources are considered resolved if

$$\Delta \geq \sqrt{\left[\mathbf{J}^{-1} \right]_{(1,1)}}. \quad (5.18)$$

This simple case is considered the baseline and will be used comparatively with polarimetric cases.

5.4 Bound for Two-Channel, Polarimetric Estimator

Next, the resolution bound for a two-channel polarimetric estimator is calculated. A two-channel system observes both polarized and unpolarized data in two independent channels. If the data observed in the polarized and unpolarized channels are statistically independent, the joint probability density function can be expressed as a product of the marginal density functions. The joint PDF is

$$P[d_k(\mathbf{x}), d_l(\mathbf{x})] = \prod_k \prod_l \prod_x \frac{1}{R_{o1}(\mathbf{x})R_{o2}(\mathbf{x})} \exp \left[\frac{-d_k(\mathbf{x})}{R_{o1}(\mathbf{x})} + \frac{-d_l(\mathbf{x})}{R_{o2}(\mathbf{x})} \right], \quad (5.19)$$

where R_{o1} is the expected value of the data observed in the unpolarized channel and R_{o2} is the expected value of the data observed in the polarized channel. The polarized channel observes the autocorrelation of the object as viewed through the polarizer. The polarized object, o_p , is described by

$$\begin{aligned}
o_p(\mathbf{u}) &= p(\mathbf{u})o(\mathbf{u}) \\
&= o_1p_1\delta(\mathbf{u}) + o_2p_2\delta(\mathbf{u} - \Delta).
\end{aligned} \tag{5.20}$$

The expected value of the observed data in the unpolarized channel remains as detailed in Eqn. 5.4. The expected value of the observed data in the polarized channel is

$$\begin{aligned}
R_{o_2}(\mathbf{x}) &= \iint_{-\infty}^{\infty} o_p(\mathbf{u})o_p(\mathbf{v} + \mathbf{u})g(\mathbf{x} - \mathbf{v})d\mathbf{u}d\mathbf{v} \\
&= \iint_{-\infty}^{\infty} \left[o_1p_1\delta(\mathbf{u}) + o_2p_2\delta(\mathbf{u} - \Delta) \right] \\
&\quad \cdot \left[o_1p_1\delta(\mathbf{u} + \mathbf{v}) + o_2p_2\delta(\mathbf{u} + \mathbf{v} - \Delta) \right] g(\mathbf{x} - \mathbf{v})d\mathbf{u}d\mathbf{v} \\
&= \iint_{-\infty}^{\infty} \left[o_1^2p_1^2\delta(\mathbf{u})\delta(\mathbf{u} + \mathbf{v}) + o_1p_1o_2p_2\delta(\mathbf{u})\delta(\mathbf{u} + \mathbf{v} - \Delta) \right. \\
&\quad \left. + o_1p_1o_2p_2\delta(\mathbf{u} - \Delta)\delta(\mathbf{u} + \mathbf{v}) + o_2^2p_2^2\delta(\mathbf{u} - \Delta)\delta(\mathbf{u} + \mathbf{v} - \Delta) \right] g(\mathbf{x} - \mathbf{v})d\mathbf{u}d\mathbf{v} \\
&= \int_{-\infty}^{\infty} \left[o_1^2p_1^2\delta(\mathbf{v}) + o_1p_1o_2p_2\delta(\mathbf{v} - \Delta) + o_1p_1o_2p_2\delta(\mathbf{v} + \Delta) \right. \\
&\quad \left. + o_2^2p_2^2\delta(\mathbf{v}) \right] g(\mathbf{x} - \mathbf{v})d\mathbf{v} \\
&= [o_1^2p_1^2 + o_2^2p_2^2]g(\mathbf{x}) + o_1p_1o_2p_2[g(\mathbf{x} - \Delta) + g(\mathbf{x} + \Delta)].
\end{aligned} \tag{5.21}$$

If $o_1 = o_2$ then the expected values in the unpolarized and polarized channels simplify to

$$R_{o1}(\mathbf{x}) = 2o_1^2 g(\mathbf{x}) + o_1^2 [g(\mathbf{x} - \Delta) + g(\mathbf{x} + \Delta)] \quad (5.22)$$

$$R_{o2}(\mathbf{x}) = o_1^2 [p_1^2 + p_2^2] g(\mathbf{x}) + o_1^2 p_1 p_2 [g(\mathbf{x} - \Delta) + g(\mathbf{x} + \Delta)]. \quad (5.23)$$

The log-likelihood function, L is detailed as

$$L(\Delta, o_1, p_1, p_2) = \sum_k \sum_l \sum_x \left\{ -\ln R_{o1}(\mathbf{x}) - \ln R_{o2}(\mathbf{x}) - \frac{d_k(\mathbf{x})}{R_{o1}(\mathbf{x})} - \frac{d_l(\mathbf{x})}{R_{o2}(\mathbf{x})} \right\}. \quad (5.24)$$

Computing the Fisher Information matrix yields

$$\begin{aligned} J_{ij} &= -E \left[\frac{\partial^2 L(\Delta, o_1, p_1, p_2)}{\partial L_i \partial L_j} \right] \\ &= K^2 \sum_x \left\{ \frac{1}{R_{o1}^2(\mathbf{x})} \frac{\partial R_{o1}(\mathbf{x})}{\partial L_i} \frac{\partial R_{o1}(\mathbf{x})}{\partial L_j} + \frac{1}{R_{o2}^2(\mathbf{x})} \frac{\partial R_{o2}(\mathbf{x})}{\partial L_i} \frac{\partial R_{o2}(\mathbf{x})}{\partial L_j} \right\}. \end{aligned} \quad (5.25)$$

Evaluating the partial derivatives of the autocorrelation in the polarized channel yields

$$\begin{aligned} \frac{\partial R_{o2}(\mathbf{x})}{\partial \Delta} &= \frac{\partial}{\partial \Delta} \left\{ o_1^2 [p_1^2 + p_2^2] g(\mathbf{x}) + o_1^2 p_1 p_2 [g(\mathbf{x} - \Delta) + g(\mathbf{x} + \Delta)] \right\} \\ &= o_1^2 p_1 p_2 \left[g'(\mathbf{x} + \Delta) - g'(\mathbf{x} - \Delta) \right], \end{aligned} \quad (5.26)$$

$$\frac{\partial R_{o2}(y)}{\partial o_1} = 2o_1 [p_1^2 + p_2^2] g(\mathbf{x}) + 2o_1 p_1 p_2 [g(\mathbf{x} - \Delta) + g(\mathbf{x} + \Delta)], \quad (5.27)$$

$$\frac{\partial R_{o2}(y)}{\partial p_1} = 2o_1^2 p_1 g(\mathbf{x}) + o_1^2 p_2 [g(\mathbf{x} - \Delta) + g(\mathbf{x} + \Delta)], \quad (5.28)$$

$$\frac{\partial R_{o2}(y)}{\partial p_2} = 2o_1^2 p_2 g(\mathbf{x}) + o_1^2 p_1 [g(\mathbf{x} - \Delta) + g(\mathbf{x} + \Delta)]. \quad (5.29)$$

For comparison to the single-channel, unpolarized case the bound with point source intensity $o_1 = o_2$ is computed. The two point sources may not have the same degree of polarization and will produce different intensities as viewed through a polarizer. The unknown parameters consist of the separation parameter, Δ , the point source intensity, o_1 , and the polarization ratio, p . Again, the number of nuisance parameters is minimized to avoid an ill-conditioned matrix. The elements of the Fisher Information matrix are calculated next.

$$\begin{aligned}
J_{\Delta\Delta} &= K^2 \sum_x \left\{ \frac{1}{R_{o1}^2(\mathbf{x})} \left(\frac{\partial R_{o1}(\mathbf{x})}{\partial \Delta} \right)^2 + \frac{1}{R_{o2}^2(\mathbf{x})} \left(\frac{\partial R_{o2}(\mathbf{x})}{\partial \Delta} \right)^2 \right\} \\
&= K^2 \sum_x \frac{o_1^4}{R_{o1}^2(\mathbf{x})} \left[g'(\mathbf{x} + \Delta) - g'(\mathbf{x} - \Delta) \right]^2 \\
&\quad + K^2 \sum_x \frac{o_1^4 p_1^2 p_2^2}{R_{o2}^2(\mathbf{x})} \left[g'(\mathbf{x} + \Delta) - g'(\mathbf{x} - \Delta) \right]^2
\end{aligned} \tag{5.30}$$

$$\begin{aligned}
J_{o_1 o_1} &= K^2 \sum_x \left\{ \frac{1}{R_{o1}^2(\mathbf{x})} \left(\frac{\partial R_{o1}(\mathbf{x})}{\partial o_1} \right)^2 + \frac{1}{R_{o2}^2(\mathbf{x})} \left(\frac{\partial R_{o2}(\mathbf{x})}{\partial o_1} \right)^2 \right\} \\
&= K^2 \sum_x \frac{1}{R_{o1}^2(\mathbf{x})} \left\{ 4o_1 g(\mathbf{x}) + 2o_1 \left[g(\mathbf{x} - \Delta) + g(\mathbf{x} + \Delta) \right] \right\}^2 \\
&\quad + K^2 \sum_x \frac{1}{R_{o2}^2(\mathbf{x})} \left\{ 2o_1 [p_1^2 + p_2^2] g(\mathbf{x}) + 2o_1 p_1 p_2 \left[g(\mathbf{x} - \Delta) + g(\mathbf{x} + \Delta) \right] \right\}^2
\end{aligned} \tag{5.31}$$

$$\begin{aligned}
J_{p_1 p_1} &= K^2 \sum_x \left\{ \frac{1}{R_{o1}^2(\mathbf{x})} \left(\frac{\partial R_{o1}(\mathbf{x})}{\partial p_1} \right)^2 + \frac{1}{R_{o2}^2(\mathbf{x})} \left(\frac{\partial R_{o2}(\mathbf{x})}{\partial p_1} \right)^2 \right\} \\
&= K^2 \sum_x \frac{1}{R_{o2}^2(\mathbf{x})} \left\{ 2o_1^2 p_1 g(\mathbf{x}) + o_1^2 p_2 \left[g(\mathbf{x} - \Delta) + g(\mathbf{x} + \Delta) \right] \right\}^2
\end{aligned} \tag{5.32}$$

$$\begin{aligned}
J_{p_2 p_2} &= K^2 \sum_x \left\{ \frac{1}{R_{o1}^2(\mathbf{x})} \left(\frac{\partial R_{o1}(\mathbf{x})}{\partial p_2} \right)^2 + \frac{1}{R_{o2}^2(\mathbf{x})} \left(\frac{\partial R_{o2}(\mathbf{x})}{\partial p_2} \right)^2 \right\} \\
&= K^2 \sum_x \frac{1}{R_{o2}^2(\mathbf{x})} \left\{ 2o_1^2 p_2 g(\mathbf{x}) + o_1^2 p_1 \left[g(\mathbf{x} - \Delta) + g(\mathbf{x} + \Delta) \right] \right\}^2
\end{aligned} \tag{5.33}$$

$$\begin{aligned}
J_{\Delta o_1} &= K^2 \sum_x \left\{ \frac{1}{R_{o1}^2(\mathbf{x})} \frac{\partial R_{o1}(\mathbf{x})}{\partial \Delta} \frac{\partial R_{o1}(\mathbf{x})}{\partial o_1} + \frac{1}{R_{o2}^2(\mathbf{x})} \frac{\partial R_{o2}(\mathbf{x})}{\partial \Delta} \frac{\partial R_{o2}(\mathbf{x})}{\partial o_1} \right\} \\
&= K^2 \sum_x \frac{1}{R_{o1}^2(\mathbf{x})} \left\{ 4o_1^3 g(\mathbf{x}) \left[g'(\mathbf{x} + \Delta) - g'(\mathbf{x} - \Delta) \right] \right. \\
&\quad \left. + 2o_1^3 \left[g(\mathbf{x} - \Delta) + g(\mathbf{x} + \Delta) \right] \left[g'(\mathbf{x} + \Delta) - g'(\mathbf{x} - \Delta) \right] \right\} \\
&\quad + K^2 \sum_x \frac{1}{R_{o2}^2(\mathbf{x})} \left\{ 2o_1^3 p_1 p_2 [p_1^2 + p_2^2] g(\mathbf{x}) \left[g'(\mathbf{x} + \Delta) - g'(\mathbf{x} - \Delta) \right] \right. \\
&\quad \left. + 2o_1^3 p_1^2 p_2^2 \left[g(\mathbf{x} - \Delta) + g(\mathbf{x} + \Delta) \right] \left[g'(\mathbf{x} + \Delta) - g'(\mathbf{x} - \Delta) \right] \right\}
\end{aligned} \tag{5.34}$$

$$\begin{aligned}
J_{\Delta p_1} &= K^2 \sum_x \left\{ \frac{1}{R_{o_2}^2(\mathbf{x})} \frac{\partial R_{o_2}(\mathbf{x})}{\partial \Delta} \frac{\partial R_{o_2}(\mathbf{x})}{\partial p_1} \right\} \\
&= K^2 \sum_x \frac{1}{R_{o_2}^2(\mathbf{x})} \left\{ 2o_1^4 p_1^2 p_2 g(\mathbf{x}) \left[g'(\mathbf{x} + \Delta) - g'(\mathbf{x} - \Delta) \right] \right. \\
&\quad \left. + o_1^4 p_1 p_2^2 \left[g(\mathbf{x} - \Delta) + g'(\mathbf{x} + \Delta) \right] \left[g'(\mathbf{x} + \Delta) - g'(\mathbf{x} - \Delta) \right] \right\} \quad (5.35)
\end{aligned}$$

$$\begin{aligned}
J_{\Delta p_2} &= K^2 \sum_x \left\{ \frac{1}{R_{o_2}^2(\mathbf{x})} \frac{\partial R_{o_2}(\mathbf{x})}{\partial \Delta} \frac{\partial R_{o_2}(\mathbf{x})}{\partial p_2} \right\} \\
&= K^2 \sum_x \frac{1}{R_{o_2}^2(\mathbf{x})} \left\{ 2o_1^4 p_1 p_2^2 g(\mathbf{x}) \left[g'(\mathbf{x} + \Delta) - g'(\mathbf{x} - \Delta) \right] \right. \\
&\quad \left. + o_1^4 p_1^2 p_2 \left[g(\mathbf{x} - \Delta) + g'(\mathbf{x} + \Delta) \right] \left[g'(\mathbf{x} + \Delta) - g'(\mathbf{x} - \Delta) \right] \right\} \quad (5.36)
\end{aligned}$$

$$J_{o_1 \Delta} = J_{\Delta o_1} \quad (5.37)$$

$$\begin{aligned}
J_{o_1 p_1} &= K^2 \sum_x \left\{ \frac{1}{R_{o_2}^2(\mathbf{x})} \frac{\partial R_{o_2}(\mathbf{x})}{\partial o_1} \frac{\partial R_{o_2}(\mathbf{x})}{\partial p_1} \right\} \\
&= K^2 \sum_x \frac{1}{R_{o_2}^2(\mathbf{x})} \left\{ 4o_1^3 p_1 [p_1^2 + p_2^2] g^2(\mathbf{x}) + 4o_1^3 p_1^2 p_2 g(\mathbf{x}) \left[g(\mathbf{x} - \Delta) + g(\mathbf{x} + \Delta) \right] \right. \\
&\quad \left. + 2o_1^3 p_2 [p_1^2 + p_2^2] g(\mathbf{x}) \left[g(\mathbf{x} - \Delta) + g(\mathbf{x} + \Delta) \right] \right. \\
&\quad \left. + 2o_1^3 p_1 p_2^2 \left[g(\mathbf{x} - \Delta) + g(\mathbf{x} + \Delta) \right]^2 \right\} \quad (5.38)
\end{aligned}$$

$$\begin{aligned}
J_{o_1 p_2} &= K^2 \sum_x \left\{ \frac{1}{R_{o_2}^2(\mathbf{x})} \frac{\partial R_{o_2}(\mathbf{x})}{\partial o_1} \frac{\partial R_{o_2}(\mathbf{x})}{\partial p_2} \right\} \\
&= K^2 \sum_x \frac{1}{R_{o_2}^2(\mathbf{x})} \left\{ 4o_1^3 p_2 [p_1^2 + p_2^2] g^2(\mathbf{x}) + 4o_1^3 p_1 p_2^2 g(\mathbf{x}) \left[g(\mathbf{x} - \Delta) + g(\mathbf{x} + \Delta) \right] \right. \\
&\quad \left. + 2o_1^3 p_1 [p_1^2 + p_2^2] g(\mathbf{x}) \left[g(\mathbf{x} - \Delta) + g(\mathbf{x} + \Delta) \right] \right. \\
&\quad \left. + 2o_1^3 p_1^2 p_2 \left[g(\mathbf{x} - \Delta) + g(\mathbf{x} + \Delta) \right]^2 \right\} \quad (5.39)
\end{aligned}$$

$$J_{p_1 \Delta} = J_{\Delta p_1} \quad (5.40)$$

$$J_{p_1 o_1} = J_{o_1 p_1} \quad (5.41)$$

$$\begin{aligned}
J_{p_1 p_2} &= K^2 \sum_x \left\{ \frac{1}{R_{o_2}^2(\mathbf{x})} \frac{\partial R_{o_2}(\mathbf{x})}{\partial p_1} \frac{\partial R_{o_2}(\mathbf{x})}{\partial p_2} \right\} \\
&= K^2 \sum_x \frac{1}{R_{o_2}^2(\mathbf{x})} \left\{ 4o_1^4 p_1 p_2 g^2(\mathbf{x}) + 2o_1^4 p_1^2 g(\mathbf{x}) \left[g(\mathbf{x} - \Delta) + g(\mathbf{x} + \Delta) \right] \right. \\
&\quad + 2o_1^4 p_2^2 g(\mathbf{x}) \left[g(\mathbf{x} - \Delta) + g(\mathbf{x} + \Delta) \right] \\
&\quad \left. + o_1^4 p_1 p_2 \left[g(\mathbf{x} - \Delta) + g(\mathbf{x} + \Delta) \right]^2 \right\} \tag{5.42}
\end{aligned}$$

$$J_{p_2 \Delta} = J_{\Delta p_2} \tag{5.43}$$

$$J_{p_2 o_1} = J_{o_1 p_2} \tag{5.44}$$

$$J_{p_2 p_1} = J_{p_1 p_2} \tag{5.45}$$

$$\tag{5.46}$$

As stated previously, the error bound or smallest possible variances of the estimated parameters are calculated by taking the inverse of the Fisher Information matrix. The bound for each unknown parameter is found along the diagonal of the inverted matrix. The lower bound (variance) on the separation parameter Δ , is detailed by

$$\sigma_{\Delta}^2 \geq \left[\mathbf{J}^{-1} \right]_{(1,1)}. \tag{5.47}$$

5.5 Bound for Dual-Channel, Polarimetric Estimator

Next, the resolution bound for a dual-channel polarimetric estimator is calculated. A dual-channel system observes polarized and data in two independent channels. The polarizer in channel one is orthogonal to the polarizer in channel two. If the data observed in the two channels are statistically independent, the joint probability

density function is identical to Eqn. 5.19 with the expected values of the two channels formulated differently. The joint PDF is

$$P[d_k(\mathbf{x}), d_l(\mathbf{x})] = \prod_k \prod_l \prod_x \frac{1}{R_{o1}(\mathbf{x})R_{o2}(\mathbf{x})} \exp \left[\frac{-d_k(\mathbf{x})}{R_{o1}(\mathbf{x})} + \frac{-d_l(\mathbf{x})}{R_{o2}(\mathbf{x})} \right], \quad (5.48)$$

where R_{o1} is the expected value of the polarized data observed in the channel one and R_{o2} is the expected value of the polarized data observed in the second channel. With the dual-channel system, the two channels of observed data are related by the following equation:

$$p_2 = 1 - p_1, \quad (5.49)$$

where p_1 represents the polarization ratio of channel one and p_2 represents the polarization ratio of channel two. In each channel, a noisy object autocorrelation is observed as viewed through the polarizer. The polarized object as viewed in channels one and two respectively are described by

$$o_{p1}(\mathbf{u}) = p_1(\mathbf{u})o(\mathbf{u}), \quad (5.50)$$

$$o_{p2}(\mathbf{u}) = p_2(\mathbf{u})o(\mathbf{u}). \quad (5.51)$$

Substituting Eqn. 5.1 and Eqn. 5.49, into the above equations for the polarized object yields

$$o_{p1}(\mathbf{u}) = o_1 p_{11} \delta(\mathbf{u}) + o_2 p_{12} \delta(\mathbf{u} - \Delta), \quad (5.52)$$

$$\begin{aligned} o_{p2}(\mathbf{u}) &= o_1 p_{21} \delta(\mathbf{u}) + o_2 p_{22} \delta(\mathbf{u} - \Delta), \\ &= o_1 [1 - p_{11}] \delta(\mathbf{u}) + o_2 [1 - p_{12}] \delta(\mathbf{u} - \Delta), \end{aligned} \quad (5.53)$$

where the subscripts on the polarization ratio $(_{11})$ and $(_{12})$ represent channel one and object point source one and two respectively. In order to harmonize with previous developments, it is assumed the point source intensities are identical, $o_1 = o_2$; however, each point source may have a different polarization response, $p_{11} \neq p_{12}$. With the polarized object described, the expected value of the observed data in the two channels are related to the polarized object autocorrelation:

$$R_{o1}(\mathbf{x}) = o_1^2 [p_{11}^2 + p_{12}^2] g(\mathbf{x}) + o_1^2 p_{11} p_{12} [g(\mathbf{x} - \Delta) + g(\mathbf{x} + \Delta)], \quad (5.54)$$

$$\begin{aligned} R_{o2}(\mathbf{x}) &= o_1^2 [(1 - p_{11})^2 + (1 - p_{12})^2] g(\mathbf{x}) \\ &\quad + o_1^2 (1 - p_{11})(1 - p_{12}) [g(\mathbf{x} - \Delta) + g(\mathbf{x} + \Delta)]. \end{aligned} \quad (5.55)$$

The log-likelihood function and the Fisher Information matrix is constructed identical to Eqns. 5.24 and 5.25. Evaluating the partial derivatives of the polarized autocorrelations is similar to the polarized channel found in two-channel case. The elements of the Fisher Information matrix are calculated next.

$$\begin{aligned}
J_{\Delta\Delta} &= K^2 \sum_x \left\{ \frac{1}{R_{o1}^2(\mathbf{x})} \left(\frac{\partial R_{o1}(\mathbf{x})}{\partial \Delta} \right)^2 + \frac{1}{R_{o2}^2(\mathbf{x})} \left(\frac{\partial R_{o2}(\mathbf{x})}{\partial \Delta} \right)^2 \right\} \\
&= K^2 \sum_x \frac{o_1^4 p_{11}^2 p_{12}^2}{R_{o1}^2(\mathbf{x})} \left[g'(\mathbf{x} + \Delta) - g'(\mathbf{x} - \Delta) \right]^2 \\
&\quad + K^2 \sum_x \frac{o_1^4 (1 - p_{11})^2 (1 - p_{12})^2}{R_{o2}^2(\mathbf{x})} \left[g'(\mathbf{x} + \Delta) - g'(\mathbf{x} - \Delta) \right]^2 \tag{5.56}
\end{aligned}$$

$$\begin{aligned}
J_{o_1 o_1} &= K^2 \sum_x \left\{ \frac{1}{R_{o1}^2(\mathbf{x})} \left(\frac{\partial R_{o1}(\mathbf{x})}{\partial o_1} \right)^2 + \frac{1}{R_{o2}^2(\mathbf{x})} \left(\frac{\partial R_{o2}(\mathbf{x})}{\partial o_1} \right)^2 \right\} \\
&= K^2 \sum_x \frac{1}{R_{o1}^2(\mathbf{x})} \left\{ 2o_1 [p_{11}^2 + p_{12}^2] g(\mathbf{x}) + 2o_1 p_{11} p_{12} \left[g(\mathbf{x} - \Delta) + g(\mathbf{x} + \Delta) \right] \right\}^2 \\
&\quad + K^2 \sum_x \frac{1}{R_{o2}^2(\mathbf{x})} \left\{ 2o_1 [(1 - p_{11})^2 + (1 - p_{12})^2] g(\mathbf{x}) \right. \\
&\quad \left. + 2o_1 (1 - p_{11})(1 - p_{12}) \left[g(\mathbf{x} - \Delta) + g(\mathbf{x} + \Delta) \right] \right\}^2 \tag{5.57}
\end{aligned}$$

$$\begin{aligned}
J_{p_{11} p_{11}} &= K^2 \sum_x \left\{ \frac{1}{R_{o1}^2(\mathbf{x})} \left(\frac{\partial R_{o1}(\mathbf{x})}{\partial p_{11}} \right)^2 + \frac{1}{R_{o2}^2(\mathbf{x})} \left(\frac{\partial R_{o2}(\mathbf{x})}{\partial p_{11}} \right)^2 \right\} \\
&= K^2 \sum_x \frac{1}{R_{o1}^2(\mathbf{x})} \left\{ 2o_1^2 p_{11} g(\mathbf{x}) + o_1^2 p_{12} \left[g(\mathbf{x} - \Delta) + g(\mathbf{x} + \Delta) \right] \right\}^2 \\
&\quad + K^2 \sum_x \frac{1}{R_{o2}^2(\mathbf{x})} \left\{ 2o_1^2 (p_{11} - 1) g(\mathbf{x}) + o_1^2 (p_{12} - 1) \left[g(\mathbf{x} - \Delta) + g(\mathbf{x} + \Delta) \right] \right\}^2 \tag{5.58}
\end{aligned}$$

$$\begin{aligned}
J_{p_{12} p_{12}} &= K^2 \sum_x \left\{ \frac{1}{R_{o1}^2(\mathbf{x})} \left(\frac{\partial R_{o1}(\mathbf{x})}{\partial p_{12}} \right)^2 + \frac{1}{R_{o2}^2(\mathbf{x})} \left(\frac{\partial R_{o2}(\mathbf{x})}{\partial p_{12}} \right)^2 \right\} \\
&= K^2 \sum_x \frac{1}{R_{o1}^2(\mathbf{x})} \left\{ 2o_1^2 p_{12} g(\mathbf{x}) + o_1^2 p_{11} \left[g(\mathbf{x} - \Delta) + g(\mathbf{x} + \Delta) \right] \right\}^2 \\
&\quad + K^2 \sum_x \frac{1}{R_{o2}^2(\mathbf{x})} \left\{ 2o_1^2 (p_{12} - 1) g(\mathbf{x}) + o_1^2 (p_{11} - 1) \left[g(\mathbf{x} - \Delta) + g(\mathbf{x} + \Delta) \right] \right\}^2 \tag{5.59}
\end{aligned}$$

$$\begin{aligned}
J_{\Delta o_1} &= K^2 \sum_x \left\{ \frac{1}{R_{o_1}^2(\mathbf{x})} \frac{\partial R_{o_1}(\mathbf{x})}{\partial \Delta} \frac{\partial R_{o_1}(\mathbf{x})}{\partial o_1} + \frac{1}{R_{o_2}^2(\mathbf{x})} \frac{\partial R_{o_2}(\mathbf{x})}{\partial \Delta} \frac{\partial R_{o_2}(\mathbf{x})}{\partial o_1} \right\} \\
&= K^2 \sum_x \frac{1}{R_{o_1}^2(\mathbf{x})} \left\{ 2o_1^3 p_{11} p_{12} [p_{11}^2 + p_{12}^2] g(\mathbf{x}) \left[g'(\mathbf{x} + \Delta) - g'(\mathbf{x} - \Delta) \right] \right. \\
&\quad \left. + 2o_1^3 p_{11}^2 p_{12}^2 \left[g(\mathbf{x} - \Delta) + g(\mathbf{x} + \Delta) \right] \left[g'(\mathbf{x} + \Delta) - g'(\mathbf{x} - \Delta) \right] \right\} \\
&\quad + K^2 \sum_x \frac{1}{R_{o_2}^2(\mathbf{x})} \left\{ 2o_1^3 (1 - p_{11})(1 - p_{12}) [(1 - p_{11})^2 + (1 - p_{12})^2] g(\mathbf{x}) \left[g'(\mathbf{x} + \Delta) - g'(\mathbf{x} - \Delta) \right] \right. \\
&\quad \left. + 2o_1^3 (1 - p_{11})^2 (1 - p_{12})^2 \left[g(\mathbf{x} - \Delta) + g(\mathbf{x} + \Delta) \right] \left[g'(\mathbf{x} + \Delta) - g'(\mathbf{x} - \Delta) \right] \right\}
\end{aligned} \tag{5.60}$$

$$\begin{aligned}
J_{\Delta p_{11}} &= K^2 \sum_x \left\{ \frac{1}{R_{o_1}^2(\mathbf{x})} \frac{\partial R_{o_1}(\mathbf{x})}{\partial \Delta} \frac{\partial R_{o_1}(\mathbf{x})}{\partial p_{11}} + \frac{1}{R_{o_2}^2(\mathbf{x})} \frac{\partial R_{o_2}(\mathbf{x})}{\partial \Delta} \frac{\partial R_{o_2}(\mathbf{x})}{\partial p_{11}} \right\} \\
&= K^2 \sum_x \frac{1}{R_{o_1}^2(\mathbf{x})} \left\{ 2o_1^4 p_{11}^2 p_{12} g(\mathbf{x}) \left[g'(\mathbf{x} + \Delta) - g'(\mathbf{x} - \Delta) \right] \right. \\
&\quad \left. + o_1^4 p_{11} p_{12}^2 \left[g(\mathbf{x} - \Delta) + g(\mathbf{x} + \Delta) \right] \left[g'(\mathbf{x} + \Delta) - g'(\mathbf{x} - \Delta) \right] \right\} \\
&\quad + K^2 \sum_x \frac{1}{R_{o_2}^2(\mathbf{x})} \left\{ 2o_1^4 (1 - p_{11})(p_{11} - 1)(1 - p_{12}) g(\mathbf{x}) \left[g'(\mathbf{x} + \Delta) - g'(\mathbf{x} - \Delta) \right] \right. \\
&\quad \left. + o_1^4 (1 - p_{11})(1 - p_{12})(p_{12} - 1) \left[g(\mathbf{x} - \Delta) + g(\mathbf{x} + \Delta) \right] \left[g'(\mathbf{x} + \Delta) - g'(\mathbf{x} - \Delta) \right] \right\}
\end{aligned} \tag{5.61}$$

$$\begin{aligned}
J_{\Delta p_{12}} &= K^2 \sum_x \left\{ \frac{1}{R_{o_1}^2(\mathbf{x})} \frac{\partial R_{o_1}(\mathbf{x})}{\partial \Delta} \frac{\partial R_{o_1}(\mathbf{x})}{\partial p_{12}} + \frac{1}{R_{o_2}^2(\mathbf{x})} \frac{\partial R_{o_2}(\mathbf{x})}{\partial \Delta} \frac{\partial R_{o_2}(\mathbf{x})}{\partial p_{12}} \right\} \\
&= K^2 \sum_x \frac{1}{R_{o_1}^2(\mathbf{x})} \left\{ 2o_1^4 p_{11} p_{12}^2 g(\mathbf{x}) \left[g'(\mathbf{x} + \Delta) - g'(\mathbf{x} - \Delta) \right] \right. \\
&\quad \left. + o_1^4 p_{11}^2 p_{12} \left[g(\mathbf{x} - \Delta) + g(\mathbf{x} + \Delta) \right] \left[g'(\mathbf{x} + \Delta) - g'(\mathbf{x} - \Delta) \right] \right\} \\
&\quad + K^2 \sum_x \frac{1}{R_{o_2}^2(\mathbf{x})} \left\{ 2o_1^4 (1 - p_{11})(1 - p_{12})(p_{12} - 1) g(\mathbf{x}) \left[g'(\mathbf{x} + \Delta) - g'(\mathbf{x} - \Delta) \right] \right. \\
&\quad \left. + o_1^4 (1 - p_{11})(p_{11} - 1)(1 - p_{12}) \left[g(\mathbf{x} - \Delta) + g(\mathbf{x} + \Delta) \right] \left[g'(\mathbf{x} + \Delta) - g'(\mathbf{x} - \Delta) \right] \right\}
\end{aligned} \tag{5.62}$$

$$J_{o_1\Delta} = J_{\Delta o_1} \quad (5.63)$$

$$\begin{aligned}
J_{o_1 p_{11}} &= K^2 \sum_x \left\{ \frac{1}{R_{o_1}^2(\mathbf{x})} \frac{\partial R_{o_1}(\mathbf{x})}{\partial o_1} \frac{\partial R_{o_1}(\mathbf{x})}{\partial p_{11}} + \frac{1}{R_{o_2}^2(\mathbf{x})} \frac{\partial R_{o_2}(\mathbf{x})}{\partial o_1} \frac{\partial R_{o_2}(\mathbf{x})}{\partial p_{11}} \right\} \\
&= K^2 \sum_x \frac{1}{R_{o_1}^2(\mathbf{x})} \left\{ 4o_1^3 p_{11} [p_{11}^2 + p_{12}^2] g^2(\mathbf{x}) + 2o_1^3 p_{12} [p_{11}^2 + p_{12}^2] g(\mathbf{x}) \left[g(\mathbf{x} - \Delta) + g(\mathbf{x} + \Delta) \right] \right. \\
&\quad \left. + 4o_1^3 p_{11}^2 p_{12} g(\mathbf{x}) \left[g(\mathbf{x} - \Delta) + g(\mathbf{x} + \Delta) \right] + 2o_1^3 p_{11} p_{12}^2 \left[g(\mathbf{x} - \Delta) + g(\mathbf{x} + \Delta) \right]^2 \right\} \\
&\quad + K^2 \sum_x \frac{1}{R_{o_2}^2(\mathbf{x})} \left\{ 4o_1^3 (p_{11} - 1) [(1 - p_{11})^2 + (1 - p_{12})^2] g^2(\mathbf{x}) \right. \\
&\quad \left. + 2o_1^3 (p_{12} - 1) [(1 - p_{11})^2 + (1 - p_{12})^2] g(\mathbf{x}) \left[g(\mathbf{x} - \Delta) + g(\mathbf{x} + \Delta) \right] \right. \\
&\quad \left. + 4o_1^3 (p_{11} - 1) (1 - p_{11}) (1 - p_{12}) g(\mathbf{x}) \left[g(\mathbf{x} - \Delta) + g(\mathbf{x} + \Delta) \right] \right. \\
&\quad \left. + 2o_1^3 (1 - p_{11}) (p_{12} - 1) (1 - p_{12}) \left[g(\mathbf{x} - \Delta) + g(\mathbf{x} + \Delta) \right]^2 \right\} \quad (5.64)
\end{aligned}$$

$$\begin{aligned}
J_{o_1 p_{12}} &= K^2 \sum_x \left\{ \frac{1}{R_{o_1}^2(\mathbf{x})} \frac{\partial R_{o_1}(\mathbf{x})}{\partial o_1} \frac{\partial R_{o_1}(\mathbf{x})}{\partial p_{12}} + \frac{1}{R_{o_2}^2(\mathbf{x})} \frac{\partial R_{o_2}(\mathbf{x})}{\partial o_1} \frac{\partial R_{o_2}(\mathbf{x})}{\partial p_{12}} \right\} \\
&= K^2 \sum_x \frac{1}{R_{o_1}^2(\mathbf{x})} \left\{ 4o_1^3 p_{12} [p_{11}^2 + p_{12}^2] g^2(\mathbf{x}) + 2o_1^3 p_{11} [p_{11}^2 + p_{12}^2] g(\mathbf{x}) \left[g(\mathbf{x} - \Delta) + g(\mathbf{x} + \Delta) \right] \right. \\
&\quad \left. + 4o_1^3 p_{11} p_{12}^2 g(\mathbf{x}) \left[g(\mathbf{x} - \Delta) + g(\mathbf{x} + \Delta) \right] + 2o_1^3 p_{11}^2 p_{12} \left[g(\mathbf{x} - \Delta) + g(\mathbf{x} + \Delta) \right]^2 \right\} \\
&\quad + K^2 \sum_x \frac{1}{R_{o_2}^2(\mathbf{x})} \left\{ 4o_1^3 (p_{12} - 1) [(1 - p_{11})^2 + (1 - p_{12})^2] g^2(\mathbf{x}) \right. \\
&\quad \left. + 2o_1^3 (p_{11} - 1) [(1 - p_{11})^2 + (1 - p_{12})^2] g(\mathbf{x}) \left[g(\mathbf{x} - \Delta) + g(\mathbf{x} + \Delta) \right] \right. \\
&\quad \left. + 4o_1^3 (p_{12} - 1) (1 - p_{11}) (1 - p_{12}) g(\mathbf{x}) \left[g(\mathbf{x} - \Delta) + g(\mathbf{x} + \Delta) \right] \right. \\
&\quad \left. + 2o_1^3 (1 - p_{11}) (p_{11} - 1) (1 - p_{12}) \left[g(\mathbf{x} - \Delta) + g(\mathbf{x} + \Delta) \right]^2 \right\} \quad (5.65)
\end{aligned}$$

$$J_{p_{11}\Delta} = J_{\Delta p_{11}} \quad (5.66)$$

$$J_{p_{11}o_1} = J_{o_1 p_{11}} \quad (5.67)$$

$$\begin{aligned} J_{p_{11}p_{12}} &= K^2 \sum_x \left\{ \frac{1}{R_{o_1}^2(\mathbf{x})} \frac{\partial R_{o_1}(\mathbf{x})}{\partial p_{11}} \frac{\partial R_{o_1}(\mathbf{x})}{\partial p_{12}} + \frac{1}{R_{o_2}^2(\mathbf{x})} \frac{\partial R_{o_2}(\mathbf{x})}{\partial p_{11}} \frac{\partial R_{o_2}(\mathbf{x})}{\partial p_{12}} \right\} \\ &= K^2 \sum_x \frac{1}{R_{o_1}^2(\mathbf{x})} \left\{ 4o_1^4 p_{11} p_{12} g^2(\mathbf{x}) + 2o_1^4 p_{11}^2 g(\mathbf{x}) \left[g(\mathbf{x} - \Delta) + g(\mathbf{x} + \Delta) \right] \right. \\ &\quad \left. + 2o_1^4 p_{12}^2 g(\mathbf{x}) \left[g(\mathbf{x} - \Delta) + g(\mathbf{x} + \Delta) \right] + o_1^4 p_{11} p_{12} \left[g(\mathbf{x} - \Delta) + g(\mathbf{x} + \Delta) \right]^2 \right\} \\ &\quad + K^2 \sum_x \frac{1}{R_{o_2}^2(\mathbf{x})} \left\{ 4o_1^4 (p_{11} - 1)(p_{12} - 1) g^2(\mathbf{x}) \right. \\ &\quad \left. + 2o_1^4 (p_{11} - 1)^2 g(\mathbf{x}) \left[g(\mathbf{x} - \Delta) + g(\mathbf{x} + \Delta) \right] \right. \\ &\quad \left. + 2o_1^4 (p_{12} - 1)^2 g(\mathbf{x}) \left[g(\mathbf{x} - \Delta) + g(\mathbf{x} + \Delta) \right] \right. \\ &\quad \left. + o_1^4 (p_{11} - 1)(p_{12} - 1) \left[g(\mathbf{x} - \Delta) + g(\mathbf{x} + \Delta) \right]^2 \right\} \end{aligned} \quad (5.68)$$

$$J_{p_{12}\Delta} = J_{\Delta p_{12}} \quad (5.69)$$

$$J_{p_{12}o_1} = J_{o_1 p_{12}} \quad (5.70)$$

$$J_{p_{12}p_{11}} = J_{p_{11}p_{12}} \quad (5.71)$$

$$(5.72)$$

The lower bound on the separation parameter is computed identical to the previous cases, inverting the above Fisher Information matrix.

5.6 Bound Results and Comparison

For this problem, there are challenges associated with computing the Fisher Information matrix and its inverse. First, from the exponential distribution, division by the mean squared term produces numeric challenges. The sinc-squared PSF introduces extreme nulls as it tapers to zero causing division by very small numbers.

As the separation parameter is varied, the nulls of the mean squared term vary. The numerator also tapers to zero in a similar manner; however, without modification, the resulting division produces erratic oscillations in the computed variance as Δ is varied. This challenge was eliminated by a computational mask. FI matrix values where division by very a small number occurs (below a threshold) are set to zero. This computational mask eliminated the oscillations in the data allowing for the variance to decrease without discontinuity as Δ increases. The computational mask was identical for all scenarios allowing comparisons.

Second, there are a myriad of possible parameter conditions producing varying results. The computational scenarios are minimized by keeping select values constant throughout the bound computations. For various bound computations, the parameter values shown in Table 5.1 were chosen to aid in computation, comparison and analysis. For simplicity, the polarization ratio, p_1 , of the first point source is chosen to be aligned with the polarizer (e.g. $p_1 = 1$). For the dual-channel case, p_{11} is aligned with the polarizer in channel one and orthogonal to channel two. The polarization ratio of the second point source, p_2 (or p_{12}) is varied to allow for several diversity scenarios.

Table 5.1: Parameter Values for Bound Computation

Parameter	Value
o_1	1
o_2	1
p_1	1
p_2	0.25, 0.5, 0.75
K Number of Frames	100
Matrix Size (pixels)	512×512
Aperture Size (pixels)	128×128

The units for the various parameter values are briefly considered. The object parameter, o , is considered a brightness or intensity normally described in photon counts when measured with optical detectors. However, the photo count unit is dropped due to the transformation from laser speckle images to an autocorrelation image. The transformation changes the positive integer data set, \mathbb{N} to positive rational numbers, \mathbb{Q}^+ . The estimated object strength is related to the original object via a

scale factor that is a function of LADAR range equation (laser power, distance, etc.), detector integration time, aperture size, etc. Because of the transformation, photo count is dropped and (scaled) intensity is considered. In any experimental detection scenario, sufficient photo counts must be detected to produce fully formed speckle with the appropriate distribution related to the illuminated object surface. This is assumed to be properly accounted in system design. Extremely low light levels or partially formed speckle conditions are not considered. The polarization ratio is, of course, unitless since it is formed by a ratio of polarized and unpolarized object intensities. The aperture size is detailed in number of pixels. Sample size may be computed from matrix size and detection geometry. For resolution bound computations, matrix and aperture size is selected without geometry consideration. It is assumed the sample size is sufficient to meet critical sampling requirements for applicable geometries.

The last computation consideration is a separation (or matrix shift) value of less than one pixel. This was accomplished using a MATLAB[®] subroutine that implemented a sub-pixel shift performed with the two-dimensional Digital Fourier Transform. The routine implemented a digital representation of the Fourier Shift Theorem [18]. A phase shift of less than one, ($0 < a < 1$), was introduced in the Fourier domain producing a sub-pixel shift in spatial domain. This is essentially restated as

$$g(x - a, y - b) = \mathcal{F}^{-1} \left\{ G(f_x, f_y) \exp[-j2\pi(f_x a + f_y b)] \right\}. \quad (5.73)$$

5.6.1 Single-Channel, Unpolarized System. Figure 5.2 depicts the computed lower bound versus separation for the single channel case using the exponential statistics model. The aperture size is maintained constant and only the separation parameter is varied. This is the baseline for comparison with polarization diversity cases.

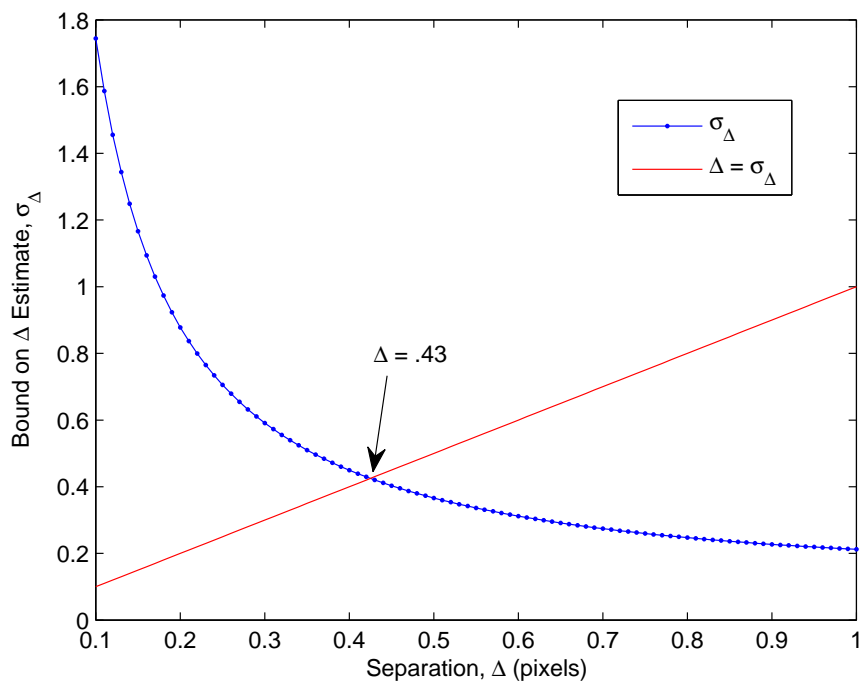


Figure 5.2: Resolution Bound vs. Separation for Single Channel Case

Correlography and phase retrieval performance does depend upon observing aperture size. A larger aperture (and all other factors constant) provides smaller sample size directly impacting resolution performance. Figure 5.3 demonstrates the effect of changing the aperture size (in pixels). As depicted, the bound computation performs as expected.

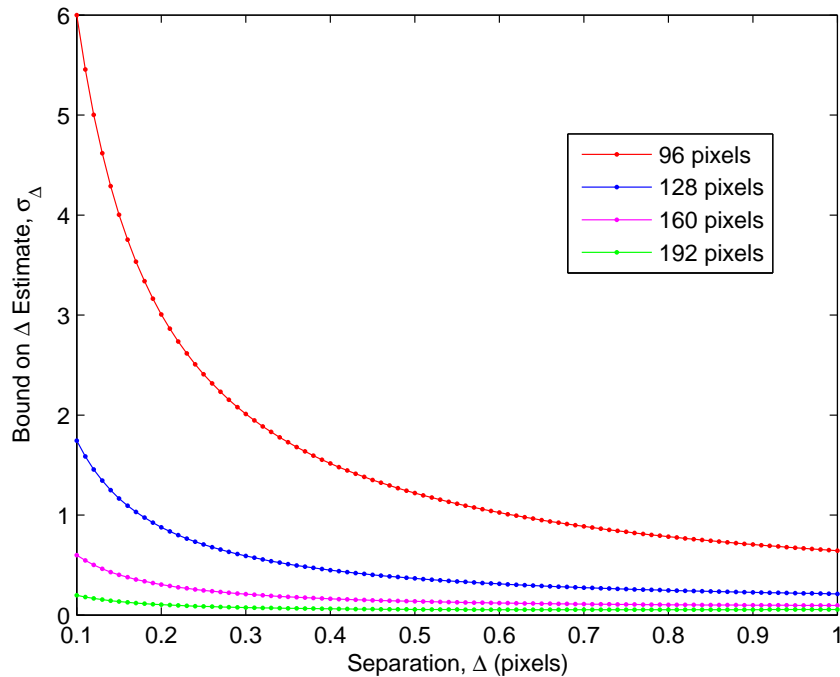


Figure 5.3: Resolution Bound vs. Separation for Various Aperture Sizes

5.6.2 *Two-Channel, Polarimetric System.* Next, the resolution bound for the two-channel system is computed and compared with the single channel system. First, it will be assumed the unpolarized channel in the two-channel system has the identical light level compared to what is collected in the single-channel system. Figure 5.4 depicts the computed bound for the two cases as a function of the separation parameter, Δ . Note, the improvement demonstrated in the two-channel case is exactly 10 times the bound of the single channel case. Because the computation was performed with $K = 100$ frames, the improvement is exactly \sqrt{K} . This improvement is directly related to the independence of the the two channels and the multiplicative $1/K$ factor in the variance computation. No significant change in performance was observed by changing the polarization difference between the two point sources in the two channel system. Therefore, the conclusion drawn from this result is the secondary channel provides significant improvement if statistical independence is observed. It

can be surmised that partial dependence or correlation between the two channels impedes the improvement and may be a subject of future research.

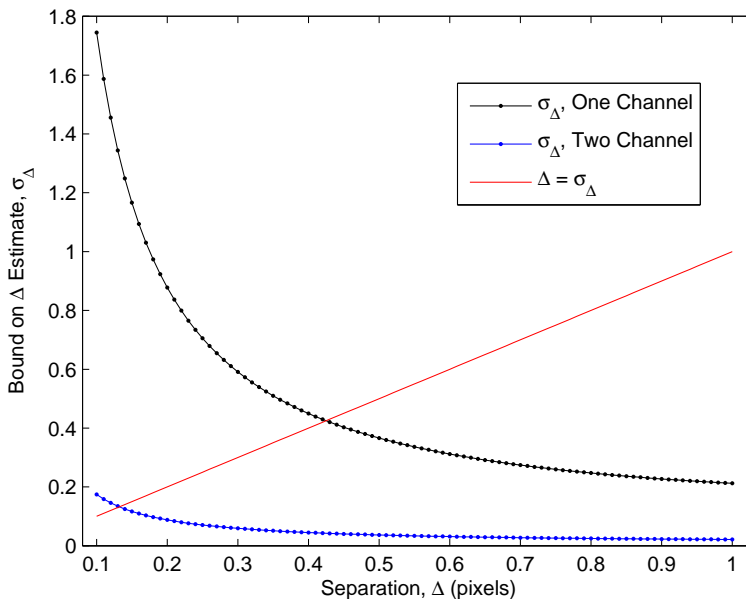


Figure 5.4: Resolution Bound vs. Separation for One and Two Channel Cases

Only minute differences ($\sim 10^{-7}$) are observed by changing the polarization ratio of the second point. The minute changes do demonstrate slight improvement when more light is observed (less suppression due to polarimeter effects). Due to only very small computational differences, it is concluded polarization differences in the object scene are not important for this simple two-point object model and the two-channel system.

As detailed in Section 3.1.1, $S + P$ results in a data set not statistically independent from either S or P channel data. Therefore, the same bound computation was repeated for the two-channel case with one-half the light level representative of collection with a non-polarizing beam splitter and polarization analyzer. The polarization difference in the two points was maintained the same. The resulting bound curve was found to be identical to Figure 5.4 as expected with an exponential noise model. The SNR for an exponential noise model is exactly one (mean equal to standard de-

viation); therefore, resulting bound computations are expected to be independent of signal strength.

5.6.3 Dual-Channel, Polarimetric System. Figure 5.5 depicts the resolution bound for the dual-channel system as a function of the separation parameter. Multiple curves are shown with three different cases of polarization difference between the point sources. Of important note, the closer the two point sources are in polarization ratio, the more light is collected and the bound is improved (lower). It is clear from this result, the polarization diversity scheme depends mostly upon statistical independence in the data channels and less so on polarization difference between the point sources. This result is specific to the two point source model; however, generalized conclusions can be surmised. For complex objects, statistical independence in the data channels is of primary importance in designing a polarimetric correlography system. Also, detection schemes should be designed to maximize light levels. For example, a PBS is superior to a standard, non-polarizing beam splitter with polarization analyzer due to transmitted light levels.

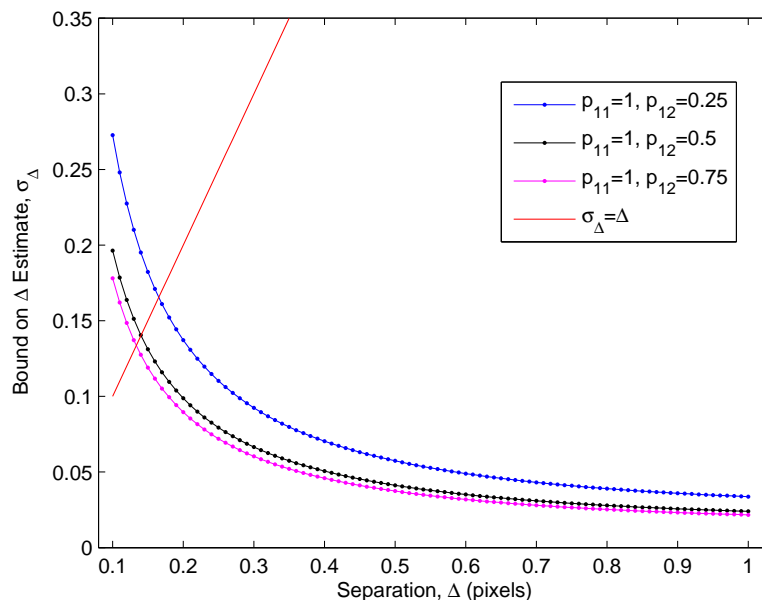


Figure 5.5: Resolution Bound vs. Separation for Dual Channel with Various Polarization States

Figure 5.6 compares the performance of the two-channel system to the dual-channel system for the same polarization difference. The two-channel system demonstrates slightly better performance; however, this can be attributed to less amplitude suppression due to the polarimeter effects in the observed data.

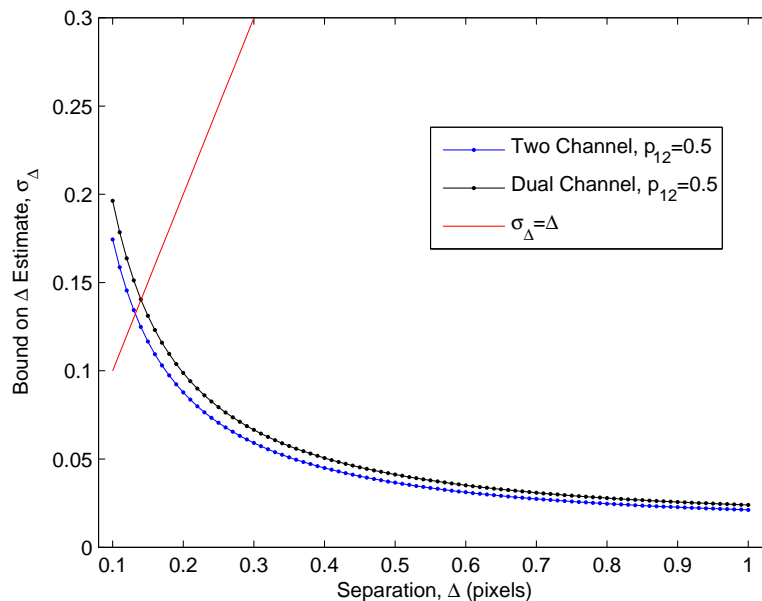


Figure 5.6: Resolution Bound vs. Separation for Two Channel and Dual Channel Cases ($p_{11} = 1, p_{12} = 0.5$)

The bound computations demonstrate both polarimetric systems outperform the unpolarized system by a factor approximately equal to \sqrt{K} . This is primarily due to statistical independence of the two observed data channels. Also, the bound computations for the simple, two-point model demonstrate scene diversity (polarization difference) is not an important factor for reducing the variance of an unbiased estimator. The phase retrieval problem is inherently ill-posed and estimators designed to solve it may be biased. Quantifying bias remains an important area of study in the field of phase retrieval.

VI. Results and Analysis

This chapter provides simulation and experimental results generated using the algorithms detailed in Chapter IV. An analysis of the results is provided with comparison to a previously published algorithm [38].

6.1 Simulation Results

This section details the results of testing the Polarimetric EM Phase Retrieval algorithm using simulated data. The simulated data consists of 100 frames per channel of the object autocorrelations corrupted with statistically independent exponential noise (see Appendix A). With the data formed in this manner, the signal-to-noise ratio (SNR) for each individual frame is approximately one. The simulated object was stored in a 128×128 discrete array with the object embedded within the support region defined as the central 64×64 portion of the array.

The simulated object consisted of three horizontal bars of different strength with each bar assigned a distinct polarization angle: bar one is zero degrees ($\theta_1 = 0^\circ$), bar two is 45 degrees ($\theta_2 = 45^\circ$), and bar three is 60 degrees ($\theta_3 = 60^\circ$). The distinct angle, θ , represents fully polarized light oriented along the described angle measured from the vertical axis. Figure 6.1 depicts the three bars with the described polarization angles.

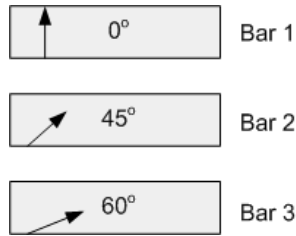


Figure 6.1: Simulated Object Polarization: 3 Bars with Various Polarization Angles

The object autocorrelation was formed and then subjected to a random exponential number generator for 100 statistically independent realizations of the noisy autocorrelation. The data for the polarization channel was formed identically to the unpolarized channel after computing the polarized version of the object, $o_p = p \times o$. The simulated polarization ratio was computed using the following equation:

$$p = \cos^2(\phi - \theta), \quad (6.1)$$

where ϕ is the orientation angle of the polarizer and θ is the orientation angle of the object element. Example data, with the polarizer transmission angle set to 90° , is pictured in Fig. 6.2.

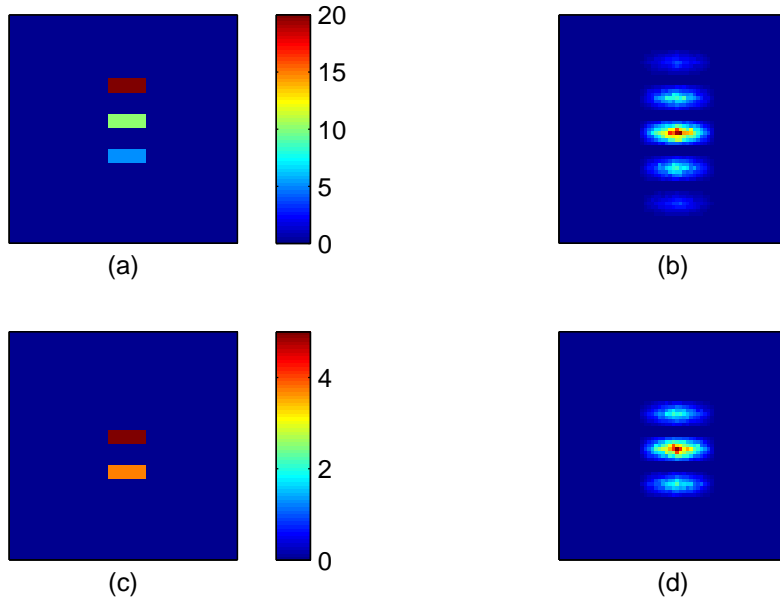


Figure 6.2: Example Simulation Data: True Object (a),(c) and Average Autocorrelation (b),(d) ($K=100$) for unpolarized channel and polarized channel $[90^\circ]$

The Polarimetric EM algorithm and Schulz and Snyder's single-channel, ML phase retrieval algorithm [38] were both run under identical conditions for comparison. The only difference being the addition of the polarized channel data and the initial guess for the p matrix needed for the Polarimetric EM algorithm. The two algorithms were run for 50 independent trials with randomly drawn initial guesses as described in Section 4.3. Total image mean-squared error (MSE) [36] of the estimate, \hat{o} , is the metric of choice for comparing simulated performance:

$$\begin{aligned}
 MSE(\hat{o}) &= E[(o - \hat{o})^2] \\
 &\cong N^{-1} \sum_x [o(\mathbf{x}) - \hat{o}(\mathbf{x})]^2,
 \end{aligned} \tag{6.2}$$

where N is the total number of pixels.

The iterative algorithm estimate is dependent upon the initial guess. Comparing with identical iteration number, a slightly different estimate is provided for every different initial guess. Because the autocorrelation is symmetric and bounded (image goes to zero at boundary), the allowed solution set includes estimates related by translation and 180° rotation. Therefore, registration of the recovered object with the original object was performed before computing error measures. This effort used a vector-based, energy-normalized, non-circular cross correlation technique for image registration [2]. The error results from the 50 trials were averaged to form a final MSE result. Each algorithm was allowed to run for a specified number of iterations before stopping. The polarimetric EM algorithm was also run with the global stopping criteria described in Section 4.4.

Figure 6.3 depicts the results of the MSE versus iteration number for both algorithms with the polarizer transmission axis set to 90° . The EM polarimetric algorithm converges faster and to a smaller MSE as compared to the ML single channel algorithm. Figure 6.3 also depicts the need for the stopping criteria. By adding polarization sensitivity to the sensor array, improvement in excess of 12 percent is observed. Similar results were observed with the polarizer transmission axis rotated to other angles.

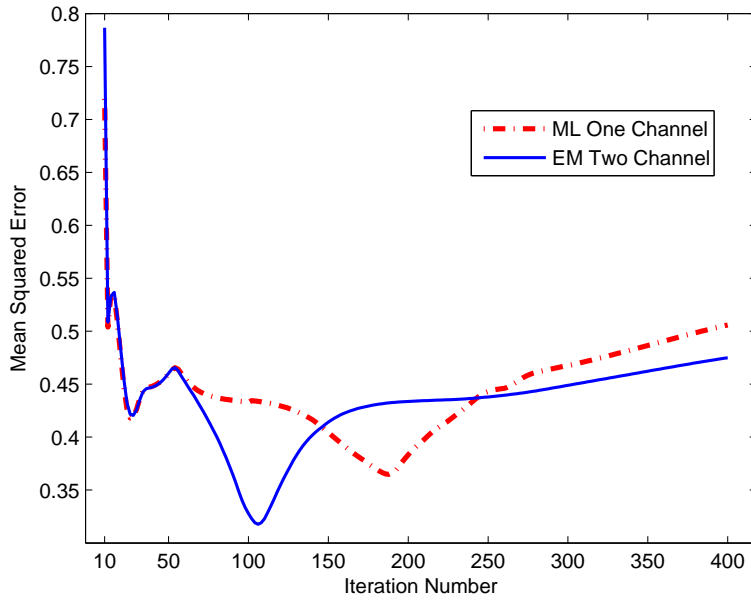


Figure 6.3: Simulated Error Results for Two Algorithms per Iteration Number (K=100 frames)

Figure 6.4 shows performance versus number of laser speckle frames, K , related to operational collection time. For the comparison in Fig. 6.4, the ML single-channel algorithm was stopped after exactly 150 iterations and the polarimetric EM algorithm stopped prior to 150 iterations near the optimum with $\beta = 1.025$. The stopping mechanism can successfully stop the algorithm near the optimum iteration number.

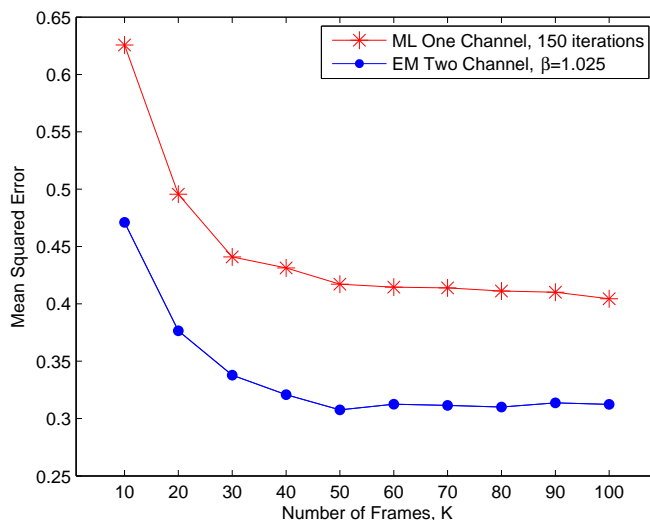


Figure 6.4: Simulated Error Results for Two Algorithms per Frame Number, K

The dual-channel algorithm is very similar but both observation channels are polarized. Both channels provide polarized data but the transmission axis of the two channels are orthogonal (90° rotation). The dual-channel algorithm was also tested with simulated data and compared to the single-channel, ML algorithm and the two-channel EM algorithm. Figure 6.5 depicts the simulated results as a function of iteration number. For the simple, 3 bar object, the dual-channel algorithm also provided improvement over the single-channel non-polarized ML algorithm. The dual-channel algorithm estimated the two-dimensional object with less MSE and fewer iterations. The stopping criteria was also successfully implemented with the dual channel algorithm. With proper selection of the dampening parameter, β , the algorithm can be stopped near the optimum iteration number or prior to the fixed 150 iterations. Figure 6.6 depicts the simulated error results as a function of frame number, K . Comparison to the single-channel, ML algorithm was accomplished with a fixed iteration number of 150. The stopping mechanism is very sensitive to the selection of β and further analysis is needed to determine a method for selecting the optimum β .

The dual-channel algorithm averages the estimator results for each channel (see Eqn. 4.56). This fusion of the two separate data sets can be problematic if the data

sets are not aligned or registered. A simple image registration routine was employed prior to adding the estimates in the two channels. Further improvement may be obtained with better data fusion techniques.

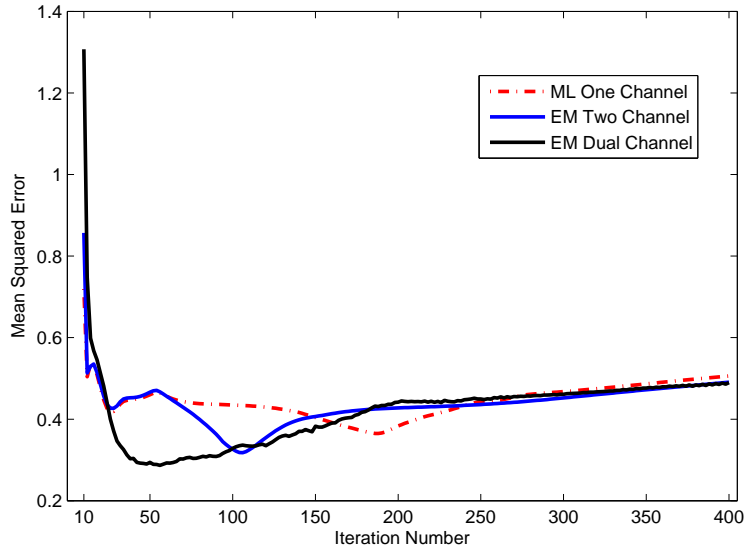


Figure 6.5: Simulated Error Results for Three Algorithms per Iteration Number (K=100 frames)

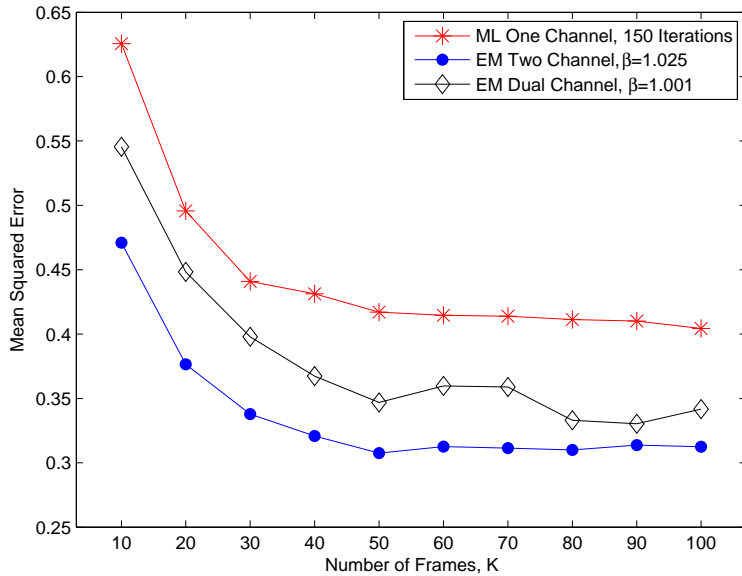


Figure 6.6: Simulated Error Results for Three Algorithms per Frame Number, K

6.2 Experimental Results

In order to validate the theoretical work and computer simulations, a simple laser speckle experiment was performed. The polarimetric phase retrieval algorithm successfully recovered a three bar object from a series of noisy autocorrelations formed from collected laser speckle images.

The laboratory experiment was conducted with available laboratory hardware. The laboratory experiment is not completely representative of the (proposed) large-scale system designed to recover remote satellite images; however, it does serve to reinforce the theory and development presented in this research. The choice of laboratory hardware was purely out of convenience and availability. Much improvement in experimental performance is available via hardware and experimental design. Even so, the chosen laboratory hardware does perform reasonably similar in function to the proposed sensor system.

A traditional charge-coupled device (CCD) camera and polarizing film was used to observe two channels of data from a coherently illuminated object. For this lab-

oratory experiment, the hardware configuration is simplified by using a continuous wave (CW) source vice a pulsed laser source. Sufficient light level is achieved by appropriate integration time at the camera.

The laboratory setup is depicted in Fig. 6.7. The test sensor consists of a Photometrics Cascade 512B camera without a lens, with removable polarization analyzer placed in front of the camera aperture. The camera is an electron-multiplying charge-coupled device sensor. The camera array is 512×512 pixels with a $16\mu\text{m}$ pitch. A spatially coherent source at 630 nm was used to back illuminate a target set. A laser line filter at 630 nm was inserted at the camera aperture to minimize background light.

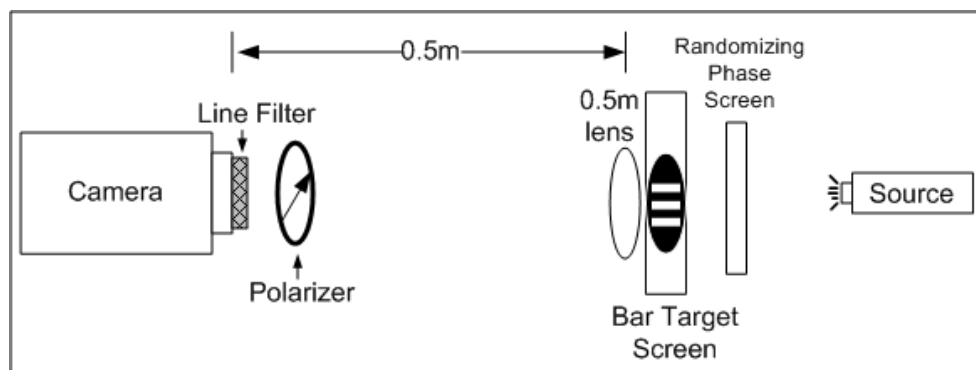


Figure 6.7: Diagram of Laboratory Setup

The target set consists of a glass plate completely opaque where no object exists and transparent where the object exists. The experimental object consisted of three identically sized bars. To emulate polarization effects, the side opposite illumination of two of the bars were covered with polarizing film aligned to the same axis. To emulate random surface roughness, a randomizing phase screen was placed between the source and the bar target consisting of highly fibrous, white paper. The paper phase screen was moved for each collection frame to emulate random phase perturbations and produce statistically independent laser speckle images.

The propagation path included a 0.5m lens at the target plane to emulate far-field (or Fraunhofer) propagation to the camera array plane. Laser power was not

a consideration as the source was placed near the target plane. Camera integration time was selected after several preliminary tests and then held constant throughout the experiment.

For extremely remote sensing such as imaging of space-borne objects, the overall path length is very large compared to distance where atmosphere turbulence is encountered enabling us to consider the atmospheric turbulence as a single, uniformly distributed phase screen. In this research, a layered atmosphere and scintillation are not considered. Experimentally, a small path length is used to ensure only uniform atmosphere is encountered.

In an operational system with LADAR backscatter, the target geometry, surface roughness and propagation distances typically produce the desired laser speckle effects. For the laboratory experiment, the paper phase screen enabled experimentation using back illumination and simplified the overall experiment. See Ref. [44] for experimentation with a backscatter setup. The paper phase screen produced low light-levels where read noise dominates the detection process, though sufficient for the experiment. However, the paper did exhibit spatially dependent surface roughness for the spatial sampling size produced by the camera. The correlography technique assumes spatially independent surface roughness (see Sec. 1.2.1). To overcome the effects of spatially dependent surface roughness and low-light levels, each 512×512 laser speckle image was segmented into 16, 128×128 laser speckle images. Each 128×128 laser speckle image contains the statistical nature of the target and can be processed independently. Target spatial resolution is lost but SNR is improved by a factor of four and spatially independent surface roughness is gained due to coarser sampling in the target plane. In order to minimize reflections from lab equipment and background light, the propagation path was enclosed in a light baffle. An image of the back illuminated target taken with the test camera (with lens and without polarizer) of the bar target is shown in Fig. 6.8. The image depicts the bright center bar and the two side bars with reduced brightness due to the effects of the polarizing film.

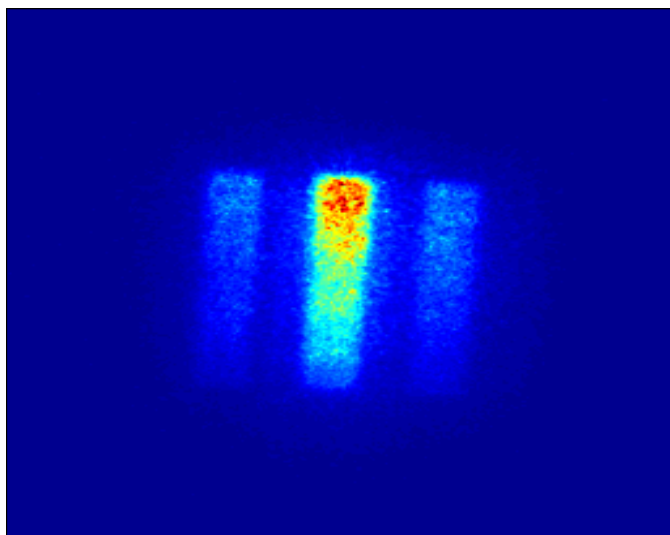


Figure 6.8: Image of Back Illuminated Bar Target Set

Figure 6.9 depicts the recovered image using the polarimetric phase retrieval algorithm. The recovered image was produced after 28 iterations. The three bar target set is clearly depicted with the side bars reduced in intensity compared to the center bar. Figure 6.10 depicts the recovered image using the single-channel algorithm developed by Schulz and Snyder [38]. For visual comparison, this image was 28 iterations and using the same starting guess as the two-channel solution. For the single-channel, Schulz-Snyder algorithm and the same iteration number, three bars are clearly discernable; however, the bar shape is more rounded and less defined compared to the two-channel polarimetric algorithm.

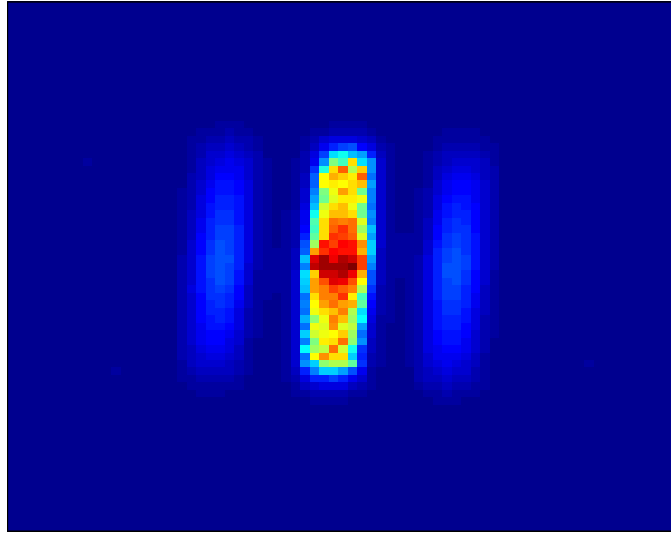


Figure 6.9: Recovered Image From Experimental Data; Two-Channel Algorithm, 28 Iterations

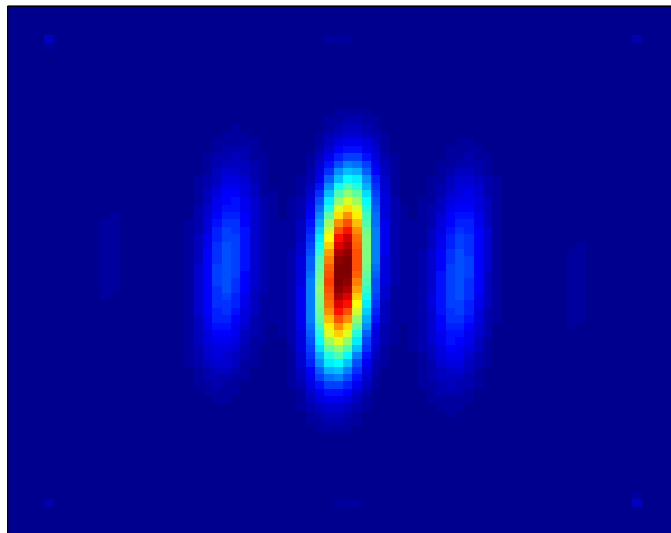


Figure 6.10: Recovered Image From Experimental Data; Single-Channel Algorithm, 28 Iterations

VII. Conclusion

Previous chapters presented a detailed background and motivation for correlography and phase retrieval that may be employed in a specific remote sensing scenario. This research is primarily motivated by the need to produce two-dimensional images of remote satellites from earth-bound sensors. For satellites located at geosynchronous orbit, traditional imaging schemes are inadequate to overcome distance and atmospheric distortion. Additionally, remote sensing of the earth's surface from spaceborne systems may also be improved. The primary motivation for considering pupil plane imaging is that very large apertures can be synthesized with a large collection of simple, inexpensive detector elements without a monolithic lens. The correlography technique using pupil plane imaging coupled with appropriate phase retrieval algorithms has shown potential to provide cost effective systems for defeating distance and atmospheric hurdles. This research provided a new investigative initiative to solve this difficult problem. This chapter concludes the main document by providing an overall summary of research activities, a summary of key findings, and recommendations for subsequent research.

7.1 Research Summary

This dissertation provides three new research contributions. First, this research demonstrated an appropriate statistical model for the transformed or processed pupil plane data. Pupil plane laser speckle is transformed by computer processing to produce images related to noisy object autocorrelations. The statistics of the non-imaged laser speckle is well studied and understood; however, the Fourier-transform, magnitude squared operation produces the noisy autocorrelation data with different statistics. This document provides an appropriate mathematical model and associated analysis demonstrating the exponential distribution either exactly describes or well approximates the statistics of the two-dimensional, transformed data image. This result has not been published prior to this research. This is an important result if a

statistical based estimation effort is to be considered for this particular phase retrieval problem. Also, the exponential noise model has implications for system design, primarily related to SNR. With each observed data frame having an SNR approximately equal to one, SNR is improved most directly by increasing observations requiring more operational collection time required. The negative exponential noise model for the noisy autocorrelation data is used throughout this dissertation to include producing data for simulation efforts. An iterative algorithm using the exponential model was explored without success in Chapter III. However, the model was successfully used throughout the research to include a theoretical lower bound on resolution for phase retrieval from correlography data.

Secondly, this research provides a new correlography and phase retrieval method using polarization diversity. Image recovery using polarization diversity has been accomplished previously with traditional imaging systems. Employing multi-channel diversity in pupil plane imaging and correlography systems has been previously suggested [23, 24]; however, this research demonstrated a novel approach. Also, a case was made here for a simpler detection system compared with previously suggested systems. Only direct-detected intensity measurements are required rather than difficult field cross products. Using active illumination with polarized laser-light, man-made object scenes can produce polarization diverse reflections and scattering. Observing these effects provides additional information about the object scene enabling improved estimation efforts in the ill-posed phase retrieval problem. Adding a secondary observation channel with polarization sensitivity demonstrates improvement over single channel, polarization insensitive schemes. Two different collection schemes were investigated for polarization sensitivity.

The two collection schemes motivated two iterative algorithms developed using an EM approach. A new technique for correlography, borrowed from traditional image recovery [43], used a polarization parameter to relate polarimetric data to non-polarized data. This added, unknown parameter, has the potential for improving the ratio of equations to unknown variables because the relationship between the object

and the polarized object data is known via the chosen mathematical model. The EM algorithm method provides a maximum-likelihood solution with the associated convergence properties. Two separate EM algorithms were presented and investigated with simulation and laboratory data. The first algorithm coupled unpolarized channel data and polarized channel data. The first algorithm employed a prior distribution for the polarization ratio to aid the solution for the unknown object estimate. The second algorithm employed two channels both sensitive to polarization but related by 90° or orthogonal in orientation. A previously published idea for algorithm stopping [31] was demonstrated to successfully stop both algorithms near an optimum iteration number. A laboratory experiment was used to demonstrate the validity of approach. Experimental results were obtained from a basic laboratory setup for the first, two-channel algorithm. The phase-retrieval problem still remains ill-posed and computationally difficult; however, adding polarization sensitivity can provide significant (greater than 10%) improvement over polarization insensitive schemes. An operational system may be developed with available, off-the-shelf technology.

The third research contribution, a lower bound on resolution was demonstrated for phase retrieval with both polarization sensitive and insensitive systems. Previous to this research, bounds on recovered image resolution have been demonstrated for traditional imaging systems obscured by atmospheric distortion; however, this has not previously been done for non-imaging, pupil plane systems. A lower bound on object intensity error for phase retrieval has been demonstrated for a generic, Gaussian model [5]; however, this research used a more accurate statistical model and provides resolution as a measure of goodness for prospective phase retrieval systems. The computed lower bound on resolution enables comparison between polarization sensitive and insensitive systems. Comparing the computed lower bound on resolution for a simple object model, this research demonstrated theoretical improvement with the introduction of polarization sensitive channel(s). Statistical independence or statistical diversity is of primary concern for multiple data channels.

7.2 *Recommendations for Future Research*

The addition of polarization diversity is shown to improve the phase retrieval problem. Additional research efforts may further improve this difficult problem leading to a cost effective system for imaging remote satellites at geosynchronous orbit. Suggested follow-on efforts include:

- Investigate additional object scene diversity such as range. Range diversity data would require a three-dimensional LADAR system. Data collection in a third dimension may possibly transform this effort to a well-posed, or even an over-determined problem.
- Investigate a three-channel polarimetric system in hopes of improving performance with additional statistical diversity. A three channel system may include an unpolarized data channel coupled with two orthogonally polarized data channels.
- Further investigation into solving the conditional expectation step in the EM process for the exponential distribution is warranted. Providing an EM algorithm with the exponential density function may provide additional improvement over the Poisson model.

7.3 *Sponsor Acknowledgement*

This research was sponsored in part by the Directed Energy Directorate of the Air Force Research Laboratory (AFRL/RD), Kirtland AFB, New Mexico, and supports their ongoing research in optical remote sensing technology. The Optics Division, AFRL/RDSA, and the Defense Advanced Research Projects Agency (DARPA) continue to actively pursue optical technology for imaging remote satellites from Earth-based sensors.

Appendix A. Proof of Equation 2.1

The development found in this appendix is primarily from [4]. This appendix provides the proof of Eqn. 2.1. A question arises: **Does averaging the non-imaged laser speckle intensity data over many independent realizations achieve useful information about the object?** This development demonstrates that no useful information is obtained by averaging nonimaged laser speckle patterns. This development ignores photon noise, detector read noise, and dark current noise dealing only with speckled intensity data.

Theorem:

$$\lim_{K \rightarrow \infty} K^{-1} \sum_{k=1}^K I_k(\mathbf{u}) = C \quad (\text{a constant}) \quad (\text{A.1})$$

where K is the number of collected frames, \mathbf{u} is the two-dimensional coordinate vector in the observation or pupil plane, and I_k is k th frame of the observed laser-speckle intensity or pupil-plane data.

Proof:

As previously stated, the intensity at the observation plane is described by

$$I(\mathbf{u}) = | \mathcal{F}^{\lambda z} \{f(\mathbf{x})\} |^2 \quad (\text{A.2})$$

and the complex field at the object plane, $f(\mathbf{x})$, is modelled by

$$f(\mathbf{x}) = a(\mathbf{x})e^{j\phi(\mathbf{x})}. \quad (\text{A.3})$$

where ϕ is random object phase uniformly distributed, $U \sim [-\pi, \pi]$ and \mathbf{x} is a two-dimensional coordinate vector in the observation or pupil plane. With the scaled Fourier Transform for Fraunhofer propagation and A.3, the field at the pupil plane is

$$F(\mathbf{u}) = \int_{-\infty}^{\infty} a(\mathbf{x}) e^{j\phi(\mathbf{x})} e^{-j2\pi\mathbf{u}\mathbf{x}/\lambda z} d\mathbf{x}, \quad (\text{A.4})$$

where λ is the optical wavelength of the illuminating field and z is the perpendicular propagation distance. Taking the magnitude squared of Eqn. A.4, produces the observation plane intensity:

$$I(\mathbf{u}) = \int_{-\infty}^{\infty} \int_{-\infty}^{\infty} a(\mathbf{x}_1) a(\mathbf{x}_2) e^{j\phi(\mathbf{x}_1)} e^{-j\phi(\mathbf{x}_2)} e^{-j2\pi\mathbf{u}(\mathbf{x}_1 - \mathbf{x}_2)/\lambda z} d\mathbf{x}_1 d\mathbf{x}_2, \quad (\text{A.5})$$

where \mathbf{x}_1 and \mathbf{x}_2 are independently indexed two-dimensional coordinate vectors. To satisfy Equation A.1, the ensemble average of Equation A.5 is taken and with a large number of independent laser speckle patterns is equal to the Expected Value operator.

$$\lim_{K \rightarrow \infty} K^{-1} \sum_{k=1}^K I_k(\mathbf{u}) = E[I_k(\mathbf{u})] \quad (\text{A.6})$$

It is assumed independent speckle realizations are produced by minute changes in the angle or phase of the illumination for each laser pulse. Taking the expected value of the intensity yields the following:

$$E[I(\mathbf{u})] = E \left[\int_{-\infty}^{\infty} \int_{-\infty}^{\infty} a(\mathbf{x}_1) a(\mathbf{x}_2) e^{j\phi(\mathbf{x}_1)} e^{-j\phi(\mathbf{x}_2)} e^{-j2\pi\mathbf{u}(\mathbf{x}_1 - \mathbf{x}_2)/\lambda z} d\mathbf{x}_1 d\mathbf{x}_2 \right]. \quad (\text{A.7})$$

Using linearity, the expected value operator is carried inside the double integral operation. Also, the amplitude of the reflected field, a is not random and is not included within the Expectation operator.

$$E[I(\mathbf{u})] = \int_{-\infty}^{\infty} \int_{-\infty}^{\infty} a(\mathbf{x}_1) a(\mathbf{x}_2) E [e^{j\phi(\mathbf{x}_1)} e^{-j\phi(\mathbf{x}_2)}] e^{-j2\pi\mathbf{u}(\mathbf{x}_1 - \mathbf{x}_2)/\lambda z} d\mathbf{x}_1 d\mathbf{x}_2 \quad (\text{A.8})$$

Analyzing just the expected value operation, this is easily computed. It is assumed the surface roughness at one point on the object surface is independent from every other point on the object surface. Because of this assumption, $\phi(\mathbf{x}_1)$ and $\phi(\mathbf{x}_2)$ are statistically independent when $\mathbf{x}_1 \neq \mathbf{x}_2$. The Expected Value Operation becomes:

$$E[e^{j\phi(\mathbf{x}_1)}] \cdot E[e^{-j\phi(\mathbf{x}_2)}], \quad \text{when } \mathbf{x}_1 \neq \mathbf{x}_2 \quad (\text{Case 1}) \quad (\text{A.9})$$

$$E[e^{j(\phi(\mathbf{x},t)-\phi(\mathbf{x},t))}] = E[e^{j0}] = 1, \quad \text{when } \mathbf{x}_1 = \mathbf{x}_2 \quad (\text{Case 2}). \quad (\text{A.10})$$

Further analysis on *Case 1* above and the use of Euler's identity yields the following relationship:

$$E[e^{j\phi}] = E[\cos(\phi) + j \sin(\phi)] = E[\cos(\phi)] + jE[\sin(\phi)]. \quad (\text{A.11})$$

Finally, assuming the random surface roughness of the object imparts a uniformly distributed phase, $\phi(\mathbf{x}) \sim U(-\pi, \pi)$, we can compute the result of *Case 1*.

$$E[\cos(\phi)] = \int_{-\pi}^{\pi} \left(\frac{1}{2\pi} \right) \cos(\phi) d\phi = 0 \quad (\text{A.12})$$

$$E[\sin(\phi)] = \int_{-\pi}^{\pi} \left(\frac{1}{2\pi} \right) \sin(\phi) d\phi = 0 \quad (\text{A.13})$$

Therefore, *Case 1* results in zero and *Case 2* results in exactly one. This can be denoted with the Dirac delta function, δ . Substituting the Expected Value result back into Equation A.8 results in

$$E[I(\mathbf{u})] = \int_{-\infty}^{\infty} \int_{-\infty}^{\infty} \delta(\mathbf{x}_1 - \mathbf{x}_2) a(\mathbf{x}_1) a(\mathbf{x}_2) e^{-j2\pi\mathbf{u}(\mathbf{x}_1 - \mathbf{x}_2)/\lambda z} d\mathbf{x}_1 d\mathbf{x}_2. \quad (\text{A.14})$$

Using the sifting property of the delta function simplifies Equation A.14 to the following:

$$\begin{aligned} E[I(\mathbf{u})] &= \int_{-\infty}^{\infty} a^2(\mathbf{x}_1) e^{-j2\pi\mathbf{u}\cdot(0)} d\mathbf{x}_1 \\ &= \int_{-\infty}^{\infty} a^2(\mathbf{x}_1) d\mathbf{x}_1. \end{aligned} \quad (\text{A.15})$$

Analyzing the Equation A.15, the integral is carried out only over the finite region $\hat{\varepsilon}$, illuminated by the laser beam (this is the beam limited scenario):

$$\int_{\hat{\varepsilon}} a^2(\mathbf{x}) d\mathbf{x} = C. \quad (\text{A.16})$$

C is a constant equal to the object intensity or brightness function summed up within the region of laser illumination. Therefore concluding the proof, it is determined that Eqn. A.1 is true.

$$\lim_{K \rightarrow \infty} K^{-1} \sum_{k=1}^K I_k(\mathbf{u}) = C, \quad (\text{a constant}) \quad (\text{A.17})$$

From this proof of Equation 2.1, it is determined that averaging nonimaged laser speckle data collected at the pupil plane over many pulses yields a constant value. The processed data will report no information related to the remote object as the resulting image will be completely washed out.

With an ergodicity assumption, this result is also achieved if one performs a time average of a single speckled intensity collected over a very long integration

period. This would be achieved with a long exposure detection and illumination with a Continuous Wave laser with a very short coherence time.

Appendix B. Proof of Equation 2.2

This appendix provides the proof of Eqn. 2.2. This result first appeared in [25] with a formal proof documented in [31]. Schulz also briefly develops this result [39]. Both [31] and [39] are missing a term in the solution; therefore, the constants are incorrectly estimated. The published results also ignore the photon noise generated during detection and is included in this appendix. The development found here is primarily from Phillips [31]. This proof includes photon noise, provides the missing mathematical steps not found in Ref. [31] and includes the missing term.

Theorem:

$$\lim_{K \rightarrow \infty} K^{-1} \sum_{k=1}^K [|\mathcal{F}^{-1}\{I_{o_k}(\mathbf{u})\}|^2] = b|h(\mathbf{x})|^2 + c[R_O(\mathbf{x}) * |h(\mathbf{x})|^2] \quad (\text{B.1})$$

\mathcal{F}^{-1} is the inverse Digital Fourier Transform (DFT) that is performed in the computer on each realization of the observed, speckled Intensity data, I_o . With a large number of laser speckle patterns, we replace the average operation with the expected value operator.

$$\lim_{K \rightarrow \infty} K^{-1} \sum_{k=1}^K [|\mathcal{F}^{-1}\{I_o(\mathbf{u})\}|^2] \equiv E[|\mathcal{F}^{-1}\{I_o(\mathbf{u})\}|^2] \quad (\text{B.2})$$

Proof:

The electric field at the object plane is described as

$$f(\mathbf{x}, t) = a(\mathbf{x}, t) \cdot e^{j\phi(\mathbf{x})} \quad (\text{B.3})$$

where t is the time parameter, $\mathbf{x} = (x, y)$ is a two dimensional spatial vector in the object plane, $\phi(\mathbf{x})$ is the phase directly related to the object surface, and $a(\mathbf{x})$

is the field amplitude. We are assuming the field amplitude is unknown but not random; however, the phase is a random function dependent upon the object surface height profile. The phase produced by each laser pulse is assumed to be statistically independent pulse to pulse due to minute changes in the laser illuminating source (angle, position, etc.) and environment (atmosphere).

The instantaneous intensity at the observation plane without noise is described by

$$I(\mathbf{u}) = | \mathcal{F}^{\lambda z} \{ f(\mathbf{x}) \} |^2 \quad (\text{B.4})$$

where $\mathcal{F}^{\lambda z}$ is a continuous, scaled Fourier Transform representing Fraunhofer propagation of the object field to the observation plane. The observed intensity (measured through optical detection devices) is formed by a doubly stochastic process distributed as negative binomial (see Section 3.4). The observed Intensity data is modeled as

$$I_o(\mathbf{u}) = [I(\mathbf{u}) + n(\mathbf{u})] \cdot A(\mathbf{u}) \quad (\text{B.5})$$

where $A(\mathbf{u})$ is the aperture function denoting the region where the speckle pattern is physically recorded; $A(\mathbf{u}) = 1$ for the points within the measurement aperture and $A(\mathbf{u}) = 0$ elsewhere. This is a real function with no complex phase term. Also, $n(\mathbf{u})$ represents photon or shot noise, a zero mean noise such that the observed intensity (conditioned on the average photon values) has a Poisson distribution with a mean equal to the intensity without photon noise. The probability density function of the noise function, n , is unknown. However, the noise is caused by the random arrival of the photons as they emerge from the optical wavefront onto the detector device. The previously published work on proving Eqn. 2.2 does not include this noise term. We include it here for completeness. This development does ignore other system noise such as pre-amplifier (read) noise and dark current noise.

$$\begin{aligned}
E[|\mathcal{F}^{-1}\{I_o(\mathbf{u})\}|^2] &= E[| \mathcal{F}^{-1}\{A(\mathbf{u})[I(\mathbf{u}) + n(\mathbf{u})]\} |^2] \\
&= E[\mathcal{F}^{-1}\{A(\mathbf{u}_1)[I(\mathbf{u}_1) + n(\mathbf{u}_1)]\} \\
&\quad \times \mathcal{F}\{A(\mathbf{u}_2)[I^*(\mathbf{u}_2) + n^*(\mathbf{u}_2)]\}] \quad (\text{B.6})
\end{aligned}$$

Taking the DFT, multiplying the two terms, and distributing the expected value Operator leads to the next equation.

$$\begin{aligned}
E[|\mathcal{F}^{-1}\{I_o(\mathbf{u})\}|^2] &= \sum_{\mathbf{u}_1=0}^{N-1} \sum_{\mathbf{u}_2=0}^{N-1} A(\mathbf{u}_1)A(\mathbf{u}_2)E[I(\mathbf{u}_1)I^*(\mathbf{u}_2)] \exp\{j2\pi\mathbf{w}(\mathbf{u}_1 - \mathbf{u}_2)/N\} \\
&\quad + \sum_{\mathbf{u}_1=0}^{N-1} \sum_{\mathbf{u}_2=0}^{N-1} A(\mathbf{u}_1)A(\mathbf{u}_2)E[I(\mathbf{u}_1)n^*(\mathbf{u}_2)] \exp\{j2\pi\mathbf{w}(\mathbf{u}_1 - \mathbf{u}_2)/N\} \\
&\quad + \sum_{\mathbf{u}_1=0}^{N-1} \sum_{\mathbf{u}_2=0}^{N-1} A(\mathbf{u}_1)A(\mathbf{u}_2)E[I^*(\mathbf{u}_2)n(\mathbf{u}_1)] \exp\{j2\pi\mathbf{w}(\mathbf{u}_1 - \mathbf{u}_2)/N\} \\
&\quad + \sum_{\mathbf{u}_1=0}^{N-1} \sum_{\mathbf{u}_2=0}^{N-1} A(\mathbf{u}_1)A(\mathbf{u}_2)E[n(\mathbf{u}_1)n^*(\mathbf{u}_2)] \exp\{j2\pi\mathbf{w}(\mathbf{u}_1 - \mathbf{u}_2)/N\} \quad (\text{B.7})
\end{aligned}$$

We will first investigate the last three terms of Eqn. B.7 involving noise. The cross terms are equal and exactly zero because the noise, $n(\mathbf{u})$ is independent of the intensity, $I(\mathbf{u})$ and the noise is zero mean. The noise, $n(\mathbf{u})$, is generated by the random arrival of the photons at the detector surface and the intensity, $I(\mathbf{u})$ is random due to the uniformly random height profile of the object surface. Because of this, we can state unequivocally the photon noise is independent of the random phase.

$$E[I(\mathbf{u}_1)n^*(\mathbf{u}_2)] = E[I(\mathbf{u}_1)]E[n^*(\mathbf{u}_2)] = 0 \quad (\text{B.8})$$

$$E[I^*(\mathbf{u}_2)n(\mathbf{u}_1)] = E[I^*(\mathbf{u}_2)]E[n(\mathbf{u}_1)] = 0 \quad (\text{B.9})$$

The last term of Eqn. B.7 involves the autocorrelation of the noise. Assuming the noise at each detector element is statistically independent from the noise at all other detector elements, leads to the result in Eqn. B.10 where, δ is the Dirac delta function and σ_n^2 is the noise power or noise variance.

$$E[n(\mathbf{u}_1)n^*(\mathbf{u}_2)] = \sigma_n^2 \cdot \delta(\mathbf{u}_1) \quad (\text{B.10})$$

Substituting the result in Eqn. B.10 back into the last term of Eqn. B.7 produces the contribution due to photon noise. The sifting property of the Dirac delta function simplifies the equation. Also, the Fourier Transform of the aperture function is a Dirac function at the origin.

$$\begin{aligned} \sum_{\mathbf{u}_1=0}^{N-1} \sum_{\mathbf{u}_2=0}^{N-1} A(\mathbf{u}_1)A(\mathbf{u}_2)\sigma_n^2\delta(\mathbf{u}_1) \exp(j2\pi\mathbf{w}(\mathbf{u}_1 - \mathbf{u}_2)/N) \\ = \sigma_n^2 \sum_{\mathbf{u}_2=0}^{N-1} A(\mathbf{u}_2) \exp(-j2\pi\mathbf{w}\mathbf{u}_2/N) \\ = \sigma_n^2\delta(\mathbf{u}) \end{aligned} \quad (\text{B.11})$$

The above simplifications of the noise terms simplifies Eqn. B.7 to the following equation.

$$E[|\mathcal{F}^{-1}\{I_o(\mathbf{u})\}|^2] = \sum_{\mathbf{u}_1=0}^{N-1} \sum_{\mathbf{u}_2=0}^{N-1} A(\mathbf{u}_1)A(\mathbf{u}_2)E[I(\mathbf{u}_1)I^*(\mathbf{u}_2)] \exp(j2\pi\mathbf{w}(\mathbf{u}_1 - \mathbf{u}_2)/N) + \sigma_n^2\delta(\mathbf{u}) \quad (\text{B.12})$$

Most of the previously published work ignores the added noise term. To complete our analysis of the Idell function, the noise term is temporarily put aside to

compute the first term without noise. We will first compute the autocorrelation of the speckle intensity without photon noise.

$$R_I(u) = E[I(\mathbf{u}_1)I^*(\mathbf{u}_2)] \quad (\text{B.13})$$

We will begin expanding the equation by analyzing the intensity at the observation plane.

$$I(\mathbf{u}) = \left| \int_{-\infty}^{\infty} a(\mathbf{x}) \cdot e^{j\phi(\mathbf{x})} \cdot e^{-j2\pi\frac{\mathbf{x}\mathbf{u}}{\lambda z}} d\mathbf{x} \right|^2 \quad (\text{B.14})$$

where $\mathbf{u} = (u, v)$ is a two dimensional spatial vector in the observation plane, λ is the wavelength, and z is the propagation distance from object to the observation plane. Expanding Equation B.13 enables one to exchange the order of integration and distribute the Expected value operator inside the Fourier integrals. Only the phase term of the reflected field is random and subject to the expected value operator.

$$R_I(u) = \int_{-\infty}^{\infty} \int_{-\infty}^{\infty} \int_{-\infty}^{\infty} \int_{-\infty}^{\infty} a(\mathbf{x}_1)a(\mathbf{x}_2)a(\mathbf{x}'_1)a(\mathbf{x}'_2)E[e^{j\phi(\mathbf{x}_1)}e^{-j\phi(\mathbf{x}_2)}e^{-j\phi(\mathbf{x}'_1)}e^{j\phi(\mathbf{x}'_2)}] \\ \times e^{-j2\pi\frac{\mathbf{x}_1\mathbf{u}_1}{\lambda z}} e^{j2\pi\frac{\mathbf{x}_2\mathbf{u}_1}{\lambda z}} e^{j2\pi\frac{\mathbf{x}'_1\mathbf{u}_2}{\lambda z}} e^{-j2\pi\frac{\mathbf{x}'_2\mathbf{u}_2}{\lambda z}} d\mathbf{x}_1d\mathbf{x}_2d\mathbf{x}'_1d\mathbf{x}'_2 \quad (\text{B.15})$$

Analyzing just the expected value operation within Equation B.15, yields the term Ψ defined as:

$$\Psi(\mathbf{x}_1, \mathbf{x}_2, \mathbf{x}'_1, \mathbf{x}'_2) = E[e^{j\phi(\mathbf{x}_1)}e^{-j\phi(\mathbf{x}_2)}e^{-j\phi(\mathbf{x}'_1)}e^{j\phi(\mathbf{x}'_2)}]. \quad (\text{B.16})$$

There are 5 cases for evaluating Ψ .

1. $\mathbf{x}_1 \neq \mathbf{x}_2 \neq \mathbf{x}'_1 \neq \mathbf{x}'_2$
2. $\mathbf{x}_1 = \mathbf{x}_2 = \mathbf{x}'_1 = \mathbf{x}'_2$

3. $\mathbf{x}_1 = \mathbf{x}'_2$ and $\mathbf{x}_2 = \mathbf{x}'_1$ and $\mathbf{x}_1 \neq \mathbf{x}_2$
4. $\mathbf{x}_1 = \mathbf{x}'_1$ and $\mathbf{x}_2 = \mathbf{x}'_2$ and $\mathbf{x}_1 \neq \mathbf{x}_2$
5. $\mathbf{x}_1 = \mathbf{x}_2$ and $\mathbf{x}'_1 = \mathbf{x}'_2$ and $\mathbf{x}_1 \neq \mathbf{x}'_1$

Case 1. If all spatial vectors are not equal, then we assume the phase terms are statistically independent. Because the four phase terms are independent, Ψ becomes Eqn. B.17. Because the phase, ϕ , of this random process is assumed to be uniformly distributed, $\sim U[-\pi, \pi]$, $E[e^{jc\phi}]$ is exactly zero (c is any integer).

$$\Psi_1 = E[e^{j\phi(\mathbf{x}_1)}] \cdot E[e^{-j\phi(\mathbf{x}_2)}] \cdot E[e^{-j\phi(\mathbf{x}'_1)}] \cdot E[e^{j\phi(\mathbf{x}'_2)}] = 0 \quad (\text{B.17})$$

Case 2. If all spatial vectors are equal, then the exponents add to zero and the expected value operator yields one, denoted with the Dirac delta function for the specific condition.

$$\begin{aligned} \Psi_2 &= E[e^{(j\phi(\mathbf{x}_1)-j\phi(\mathbf{x}_1)-j\phi(\mathbf{x}_1)+j\phi(\mathbf{x}_1))}] \\ &= E[e^{j \cdot 0}] \\ &= \delta(x_1 = x_2 = x'_1 = x'_2) \end{aligned} \quad (\text{B.18})$$

Case 3. For the spatial vectors that are equal, the exponents add together. For the spatial vectors not equal, the expected value operator can be factored into a product of two separate expected value operations due to statistical independence. Again, $E[e^{cj\phi}] = 0$.

$$\begin{aligned}
\Psi_3 &= E[e^{(j2\phi(\mathbf{x}_1)-j2\phi(\mathbf{x}_2))}] \\
&= E[e^{j2\phi(\mathbf{x}_1)}] \cdot E[e^{-j2\phi(\mathbf{x}_2)}] \\
&= 0
\end{aligned} \tag{B.19}$$

Case 4. This case is similar to **Case 3** as it factors into two separate expected value operations; however, the result of the expected value operator is one, as in **Case 2**. This is also denoted with the Dirac delta function; however, we must be careful to ensure we do not mathematically duplicate **Case 2**.

$$\begin{aligned}
\Psi_4 &= E[e^{(j\phi(\mathbf{x}_1)-j\phi(\mathbf{x}_2)-j\phi(\mathbf{x}_1)+j\phi(\mathbf{x}_2))}] \\
&= E[e^{j\cdot 0}] \cdot E[e^{j\cdot 0}] \\
&= \delta(x_1 - x'_1, x_2 - x'_2), \quad (x_1 \neq x_2)
\end{aligned} \tag{B.20}$$

Case 5. This case is the same as **Case 4**. This is also denoted with the Dirac delta function. We must be careful to ensure no duplication with **Case 2**.

$$\begin{aligned}
\Psi_5 &= E[e^{(j\phi(\mathbf{x}_1)-j\phi(\mathbf{x}_1)-j\phi(\mathbf{x}'_1)+j\phi(\mathbf{x}'_1))}] \\
&= E[e^{j\cdot 0}] \cdot E[e^{j\cdot 0}] \\
&= \delta(x_1 - x_2, x'_1 - x'_2), \quad (x_1 \neq x'_1)
\end{aligned} \tag{B.21}$$

Non-zero results are obtained from **Cases 2, 4, and 5**. **Cases 1 and 2** do not contribute to the equation. Substituting the Dirac delta functions back into Equation B.15 will enable some simplifications. The sifting property of the Dirac delta function will reduce variables and integrands.

$$\begin{aligned}
R_I(\mathbf{u}) = & \int_{-\infty}^{\infty} \int_{-\infty}^{\infty} a^2(\mathbf{x}_1) a^2(\mathbf{x}_2) e^{-j2\pi\mathbf{x}_1 \frac{(\mathbf{u}_1 - \mathbf{u}_2)}{\lambda_z}} e^{j2\pi\mathbf{x}_2 \frac{(\mathbf{u}_1 - \mathbf{u}_2)}{\lambda_z}} d\mathbf{x}_1 d\mathbf{x}_2 \\
& + \int_{-\infty}^{\infty} \int_{-\infty}^{\infty} a^2(\mathbf{x}_1) a^2(\mathbf{x}'_1) d\mathbf{x}_1 d\mathbf{x}'_1 - \int_{-\infty}^{\infty} a^4(\mathbf{x}_1) d\mathbf{x}_1 \quad (\text{B.22})
\end{aligned}$$

The first two terms in Equation B.22 are from **Cases 4** and **5**, respectively. The third term is from **Case 2** and must be subtracted once because it appears as a special case in both the first and second terms. The results from **Cases 2, 4, and 5** are now accounted for without duplication. Note, Term 3 is the missing term not found in previously published papers. Now that we have Equation B.22, the autocorrelation of the intensity, we substitute this result back into Eqn. B.12. We will ignore the noise term temporarily and add it back in at the end of this proof. Each term is dealt with separately.

$$\begin{aligned}
E[|\mathcal{F}^{-1}\{\widehat{I}_o(\mathbf{u})\}|^2] = & \sum_{\mathbf{u}_1=0}^{N-1} \sum_{\mathbf{u}_2=0}^{N-1} \int_{-\infty}^{\infty} \int_{-\infty}^{\infty} A(\mathbf{u}_1) A(\mathbf{u}_2) a^2(\mathbf{x}_1) a^2(\mathbf{x}_2) \\
& \times e^{-j2\pi\mathbf{x}_1 \frac{(\mathbf{u}_1 - \mathbf{u}_2)}{\lambda_z}} e^{j2\pi\mathbf{x}_2 \frac{(\mathbf{u}_1 - \mathbf{u}_2)}{\lambda_z}} \exp(j2\pi\mathbf{w}(\mathbf{u}_1 - \mathbf{u}_2)/N) d\mathbf{x}_1 d\mathbf{x}_2 \\
+ & \sum_{\mathbf{u}_1=0}^{N-1} \sum_{\mathbf{u}_2=0}^{N-1} \int_{-\infty}^{\infty} \int_{-\infty}^{\infty} A(\mathbf{u}_1) A(\mathbf{u}_2) a^2(\mathbf{x}_1) a^2(\mathbf{x}'_1) \exp(j2\pi\mathbf{w}(\mathbf{u}_1 - \mathbf{u}_2)/N) d\mathbf{x}_1 d\mathbf{x}'_1 \\
& - \sum_{\mathbf{u}_1=0}^{N-1} \sum_{\mathbf{u}_2=0}^{N-1} \int_{-\infty}^{\infty} A(\mathbf{u}_1) A(\mathbf{u}_2) a^4(\mathbf{x}_1) \exp(j2\pi\mathbf{w}(\mathbf{u}_1 - \mathbf{u}_2)/N) d\mathbf{x}_1 \quad (\text{B.23})
\end{aligned}$$

Term 1. We will simplify the integral with substitution of variables. If we let $x_0 = x_1 - x_2$, **Term 1** becomes

$$\begin{aligned}
T_1 = & \sum_{\mathbf{u}_1=0}^{N-1} \sum_{\mathbf{u}_2=0}^{N-1} \int_{-\infty}^{\infty} \int_{-\infty}^{\infty} A(\mathbf{u}_1) A(\mathbf{u}_2) a^2(\mathbf{x}_0 + \mathbf{x}_2) a^2(\mathbf{x}_2) e^{-j2\pi\mathbf{x}_0 \frac{(\mathbf{u}_1 - \mathbf{u}_2)}{\lambda_z}} \\
& \times \exp(j2\pi\mathbf{w}(\mathbf{u}_1 - \mathbf{u}_2)/N) d\mathbf{x}_0 d\mathbf{x}_2
\end{aligned}$$

$$\begin{aligned}
&= \sum_{\mathbf{u}_1=0}^{N-1} \sum_{\mathbf{u}_2=0}^{N-1} \int_{-\infty}^{\infty} \left[\int_{-\infty}^{\infty} a^2(\mathbf{x}_0 + \mathbf{x}_2) a^2(\mathbf{x}_2) d\mathbf{x}_2 \right] A(\mathbf{u}_1) A(\mathbf{u}_2) e^{-j2\pi\mathbf{x}_0 \frac{(\mathbf{u}_1 - \mathbf{u}_2)}{\lambda z}} \\
&\quad \times \exp(j2\pi\mathbf{w}(\mathbf{u}_1 - \mathbf{u}_2)/N) d\mathbf{x}_0 \\
&= \sum_{\mathbf{u}_1=0}^{N-1} \sum_{\mathbf{u}_2=0}^{N-1} \int_{-\infty}^{\infty} R_o(\mathbf{x}_0) A(\mathbf{u}_1) A(\mathbf{u}_2) e^{-j2\pi\mathbf{x}_0 \frac{(\mathbf{u}_1 - \mathbf{u}_2)}{\lambda z}} \\
&\quad \times \exp(j2\pi\mathbf{w}(\mathbf{u}_1 - \mathbf{u}_2)/N) d\mathbf{x}_0 \tag{B.24}
\end{aligned}$$

where $R_o(\mathbf{x}_0)$ is considered the autocorrelation of the object intensity with a spatial difference, \mathbf{x}_0 . We will continue to group terms and simplify.

$$\begin{aligned}
T_1 &= \sum_{\mathbf{u}_1=0}^{N-1} \sum_{\mathbf{u}_2=0}^{N-1} \left[\int_{-\infty}^{\infty} R_o(\mathbf{x}_0) e^{-j2\pi\mathbf{x}_0 \frac{(\mathbf{u}_1 - \mathbf{u}_2)}{\lambda z}} d\mathbf{x}_0 \right] A(\mathbf{u}_1) A(\mathbf{u}_2) \\
&\quad \times \exp(j2\pi\mathbf{w}(\mathbf{u}_1 - \mathbf{u}_2)/N) \tag{B.25}
\end{aligned}$$

Analyzing just the term in brackets, it is a scaled Fourier Transform of the intensity autocorrelation which is defined as $|F_o(\xi)|^2$. Note, since R_o is a symmetric function about the origin, its Fourier Transform is symmetric.

$$\int_{-\infty}^{\infty} R_o(\mathbf{x}_0) e^{-j2\pi\mathbf{x}_0 \frac{(\mathbf{u}_1 - \mathbf{u}_2)}{\lambda z}} d\mathbf{x}_0 \equiv \left| F_o \left(\frac{\mathbf{u}_1 - \mathbf{u}_2}{\lambda z} \right) \right|^2 \tag{B.26}$$

Plugging this result back into Term 1 yields

$$T_1 = \sum_{\mathbf{u}_1=0}^{N-1} \sum_{\mathbf{u}_2=0}^{N-1} A(\mathbf{u}_1) A(\mathbf{u}_2) \left| F_o \left(\frac{\mathbf{u}_1 - \mathbf{u}_2}{\lambda z} \right) \right|^2 \exp(j2\pi\mathbf{w}(\mathbf{u}_1 - \mathbf{u}_2)/n). \tag{B.27}$$

Using variable substitution, let $\mathbf{u}_0 = \mathbf{u}_1 - \mathbf{u}_2$.

$$T_1 = \sum_{\mathbf{u}_1=0}^{N-1} \sum_{\mathbf{u}_2=0}^{N-1} A(\mathbf{u}_0 + \mathbf{u}_2)A(\mathbf{u}_2) \left| F_o \left(\frac{\mathbf{u}_0}{\lambda z} \right) \right|^2 \exp(j2\pi\mathbf{w}\mathbf{u}_0/N) \quad (\text{B.28})$$

Next, group terms as we have previously done.

$$\begin{aligned} T_1 &= \sum_{\mathbf{u}_1=0}^{N-1} \left[\sum_{\mathbf{u}_2=0}^{N-1} A(\mathbf{u}_0 + \mathbf{u}_2)A(\mathbf{u}_2) \right] \left| F_o \left(\frac{\mathbf{u}_0}{\lambda z} \right) \right|^2 \exp(j2\pi\mathbf{w}\mathbf{u}_0/N) \\ &= \sum_{\mathbf{u}_1=0}^{N-1} R_A(\mathbf{u}_0) \left| F_o \left(\frac{\mathbf{u}_0}{\lambda z} \right) \right|^2 \exp(j2\pi\mathbf{w}\mathbf{u}_0/N) \end{aligned} \quad (\text{B.29})$$

where $R_A(\mathbf{u}_0)$ is the autocorrelation of the aperture function with a spatial difference of \mathbf{u}_0 . If we ignore the normalization constant, this is recognized as the diffraction-limited Optical Transfer Function (OTF), \mathcal{H} . Also, after ignoring the normalization constant, the inverse Fourier Transform of the OTF is the Point Spread Function (PSF) or impulse response multiplied by a constant [18].

$$\mathcal{H}(\nu) = \int_{-\infty}^{\infty} A(\mathbf{u})A(\mathbf{u}_0 + \mathbf{u})d\mathbf{u} = R_A(\mathbf{u}_0) \quad (\text{B.30})$$

$$|h(\mathbf{w})|^2 = \frac{1}{(\lambda z)^2} \int_{-\infty}^{\infty} R_A(\mathbf{u}_o) \exp(-j\frac{2\pi}{\lambda z}\mathbf{w}\mathbf{u}_o)d\mathbf{u}_o \quad (\text{B.31})$$

$$\mathcal{F}^{-1}\{\mathcal{H}(\nu)\} = (\lambda z)^2 |h(\lambda z\mathbf{w})|^2 \quad (\text{B.32})$$

Finally, for Term 1, we recognize that Equation B.29 is an inverse Fourier Transform of the product of two symmetric functions. Applying symmetry and the convolution theorem of the Fourier Transform yields Eqn. B.33. We have the autocorrelation of the object brightness function imbedded within our result.

$$\begin{aligned}
T_1 &= (\lambda z)^2 R_o(\lambda z \mathbf{w}) * |h(\lambda z \mathbf{w})|^2 \\
&= c R_o(\mathbf{x}) * |h(\mathbf{x})|^2
\end{aligned} \tag{B.33}$$

Here in this result, $c = (\lambda z)^2$ and $\mathbf{x} = \lambda z \mathbf{w}$. Therefore, Term 1 is a constant factor times the impulse response convolved with the scaled autocorrelation of the object intensity.

Term 2. We can simplify the integration by using another substitution of variables, similar to what was done for Term 1. Let $\mathbf{x}_0 = \mathbf{x}_1 - \mathbf{x}'_1$.

$$\begin{aligned}
T_2 &= \sum_{\mathbf{u}_1=0}^{N-1} \sum_{\mathbf{u}_2=0}^{N-1} \int_{-\infty}^{\infty} \int_{-\infty}^{\infty} A(\mathbf{u}_1) A(\mathbf{u}_2) a^2(\mathbf{x}_1) a^2(\mathbf{x}'_1) \exp(j2\pi \mathbf{w}(\mathbf{u}_1 - \mathbf{u}_2)/N) d\mathbf{x}_1 d\mathbf{x}'_1 \\
&= \sum_{\mathbf{u}_1=0}^{N-1} \sum_{\mathbf{u}_2=0}^{N-1} \int_{-\infty}^{\infty} \left[\int_{-\infty}^{\infty} a^2(\mathbf{x}_0 + \mathbf{x}'_1) a^2(\mathbf{x}'_1) d\mathbf{x}'_1 \right] A(\mathbf{u}_1) A(\mathbf{u}_2) \exp(j2\pi \mathbf{w}(\mathbf{u}_1 - \mathbf{u}_2)/N) d\mathbf{x}_0 \\
&= \sum_{\mathbf{u}_1=0}^{N-1} \sum_{\mathbf{u}_2=0}^{N-1} \int_{-\infty}^{\infty} R_o(\mathbf{x}_0) A(\mathbf{u}_1) A(\mathbf{u}_2) \exp(j2\pi \mathbf{w}(\mathbf{u}_1 - \mathbf{u}_2)/N) d\mathbf{x}_0
\end{aligned} \tag{B.34}$$

Again, $R_o(\mathbf{x}_0)$ is the autocorrelation of the object intensity with spatial difference, \mathbf{x}_0 . Using another substitution of variables, let $\mathbf{u}_0 = \mathbf{u}_1 - \mathbf{u}_2$ and group terms.

$$\begin{aligned}
T_2 &= \sum_{\mathbf{u}_0=-\mathbf{u}_2}^{N-1-\mathbf{u}_2} \sum_{\mathbf{u}_2=0}^{N-1} \int_{-\infty}^{\infty} R_o(\mathbf{x}_0) A(\mathbf{u}_0 + \mathbf{u}_2) A(\mathbf{u}_2) \exp(j2\pi \mathbf{w} \mathbf{u}_0/N) d\mathbf{x}_0 \\
&= \int_{-\infty}^{\infty} R_o(\mathbf{x}_0) d\mathbf{x}_0 \sum_{\mathbf{u}_0=-\mathbf{u}_2}^{N-1-\mathbf{u}_2} \sum_{\mathbf{u}_2=0}^{N-1} A(\mathbf{u}_0 + \mathbf{u}_2) A(\mathbf{u}_2) \exp(j2\pi \mathbf{w} \mathbf{u}_0/N) \\
&= \int_{-\infty}^{\infty} R_o(\mathbf{x}_0) d\mathbf{x}_0 \left[\sum_{\mathbf{u}_0=0}^{N-1} R_A(\mathbf{u}_0) \exp(j2\pi \mathbf{w} \mathbf{u}_0/N) \right]
\end{aligned} \tag{B.35}$$

where $R_A(\mathbf{u}_0)$ is the autocorrelation of the aperture function with a spatial difference of \mathbf{u}_0 . Again, this is recognized as the diffraction-limited Optical Transfer Function (OTF), \mathcal{H} , ignoring the normalization factor. As stated previously, the inverse Fourier transform of the OTF is the scaled impulse response. Next we will define S_R as the total sum of the object intensity autocorrelation. This is a constant value since the object intensity is finite in extent due to the beam limited scenario.

$$S_R = \int_{-\infty}^{\infty} R_o(\mathbf{x}_0) d\mathbf{x}_0 \quad (\text{B.36})$$

Finally, for Term 2, we are able to simplify to an easily described equation.

$$\begin{aligned} T_2 &= S_R \cdot (\lambda z)^2 |h(\lambda z \mathbf{w})|^2 \\ &= S_R \cdot c |h(\mathbf{x})|^2 \end{aligned} \quad (\text{B.37})$$

Term 3. Term 3 is the missing term not found in published literature. We will simplify Term 3 by first defining a term of summed object intensity squared, S_{I^2} .

$$S_{I^2} = \int_{-\infty}^{\infty} a^4(\mathbf{x}) d\mathbf{x} \quad (\text{B.38})$$

This is a constant term and can be factored outside any remaining integrands. We realize this quantity is finite since we are in a beam limited scenario. Returning to Term 3 and rearranging terms to identify the summed intensity squared term we find the following:

$$\begin{aligned}
T_3 &= - \sum_{\mathbf{u}_1=0}^{N-1} \sum_{\mathbf{u}_2=0}^{N-1} \int_{-\infty}^{\infty} A(\mathbf{u}_1)A(\mathbf{u}_2)a^4(\mathbf{x}_1) \exp(j2\pi\mathbf{w}(\mathbf{u}_1 - \mathbf{u}_2)/N)d\mathbf{x}_1 \\
&= - \sum_{\mathbf{u}_1=0}^{N-1} \sum_{\mathbf{u}_2=0}^{N-1} \left[\int_{-\infty}^{\infty} a^4(\mathbf{x}_1)d\mathbf{x}_1 \right] A(\mathbf{u}_1)A(\mathbf{u}_2) \exp(j2\pi\mathbf{w}(\mathbf{u}_1 - \mathbf{u}_2)/N) \\
&= - S_{I^2} \sum_{\mathbf{u}_1=0}^{N-1} \sum_{\mathbf{u}_2=0}^{N-1} A(\mathbf{u}_1)A(\mathbf{u}_2) \exp(j2\pi\mathbf{w}(\mathbf{u}_1 - \mathbf{u}_2)/N) \tag{B.39}
\end{aligned}$$

We will continue the simplification with a substitution of variables by letting $\mathbf{u}_0 = \mathbf{u}_1 - \mathbf{u}_2$ and rearranging terms.

$$\begin{aligned}
T_3 &= -S_{I^2} \sum_{\mathbf{u}_0=-u_2}^{N-1-u_2} \sum_{\mathbf{u}_2=0}^{N-1} A(\mathbf{u}_0 + \mathbf{u}_2)A(\mathbf{u}_2) \exp(j2\pi\mathbf{w}\mathbf{u}_0/N) \\
&= -S_{I^2} \sum_{\mathbf{u}_0=0}^{N-1} R_A(\mathbf{u}_0) \exp(j2\pi\mathbf{w}(\mathbf{u}_0)/N) \tag{B.40}
\end{aligned}$$

Again, $R_A(\mathbf{u}_0)$ is the autocorrelation of the aperture function with a spatial difference of \mathbf{u}_0 or the diffraction-limited OTF without the normalization factor. Recognizing the last equation is an inverse Fourier Transform of the OTF, Term 3 simplifies to

$$\begin{aligned}
T_3 &= -S_{I^2} \cdot (\lambda z)^2 |h(\lambda z \mathbf{w})|^2 \\
&= -S_{I^2} \cdot c |h(\mathbf{x})|^2. \tag{B.41}
\end{aligned}$$

The constants from Terms 2 and 3 can be combined into a single constant, b .

$$b = c \left[\int_{-\infty}^{\infty} R_o(\mathbf{x})d\mathbf{x} - \int_{-\infty}^{\infty} a^4(\mathbf{x})d\mathbf{x} \right] \tag{B.42}$$

Finalizing the Idell Function. Combining the three terms together to yield the final result for $E[|\mathcal{F}^{-1}\{I_o(\mathbf{u})\}|^2]$ (ignoring photon noise) produces the final equation.

$$E[|\mathcal{F}^{-1}\{I_o(\mathbf{u})\}|^2] = b|h(\mathbf{x})|^2 + c[R_o(\mathbf{x})] * |h(\mathbf{x})|^2 \quad (\text{B.43})$$

Therefore, the published result is proven. However, the constant, b , is not defined correctly in previous literature due to the missing term defined above.

Adding the noise term due to photon noise, the final result is given by

$$E[|\mathcal{F}^{-1}\{I_o(\mathbf{u})\}|^2] = b|h(\mathbf{x})|^2 + c[R_o(\mathbf{x})] * |h(\mathbf{x})|^2 + \sigma_n^2\delta(\mathbf{x}). \quad (\text{B.44})$$

Appendix C. Proof of Exponential Statistics for the Processed Data

This appendix details the proof for the transformed laser speckle data or noisy auto-correlations distributed as exponential with a mean equal to the autocorrelation of the true object. This proof assumes each laser speckle image is statistically independent spatially.

A single image of laser speckle data is approximated very well to be distributed as negative binomial [17]. In most detection schemes, the speckle will exhibit small, localized correlation; however, for this proof we will assume that each point in the laser speckle image is statistically independent. To form the autocorrelation data, each of the observed laser speckle intensity images are post-processed by DFT and magnitude squared operations. To prove the statistics of the processed data, this section follows Goodman's treatment of random phasor sums [17].

Each point in the intensity data is a real-valued but random number (phase equal to zero). The Fourier Transform kernel provides a complex but known phasor. For this analysis we will assume the two-dimensional data image is $N \times N$ with N sufficiently large to utilize the Central Limit Theorem. The sum of a large number of independent random variables (in this case, the random intensity values) is asymptotically Gaussian as $N \rightarrow \infty$ [17].

$$\mathcal{F}^{-1}\{I_o(u)\} = \sum_{u=0}^{N-1} I_o(u) \exp\left[\frac{j2\pi}{N}(uw)\right] \quad (\text{C.1})$$

Equation C.1 is essentially equivalent to a random phasor sum. The intensity I_o is a collection of random variables where the phase is known (exactly zero) and the magnitude is random but statistically independent of each other. To discover the statistics of the transformation produced by Eqn. C.1, we will execute Goodman's random phasor sum procedures [17]. The real and imaginary parts of the Fourier transformed data are defined as r and i , respectively.

$$r(w) = \text{Re}[\mathcal{F}^{-1}\{I_o\}] = \sum_{u=0}^{N-1} I_o(u) \cos\left[\frac{2\pi uw}{N}\right] \quad (\text{C.2})$$

$$i(w) = \text{Im}[\mathcal{F}^{-1}\{I_o\}] = \sum_{u=0}^{N-1} I_o(u) \sin\left[\frac{2\pi uw}{N}\right] \quad (\text{C.3})$$

Next, the mean of the real and imaginary parts are computed. Because the expected value of laser speckle is a constant (e.g. $E[I_o] = C$), the expected value of the real and imaginary parts, are two-dimensional Cosine and Sine transforms, respectively, of a constant value. The mean of the real and imaginary parts are equal except at $w = 0$,

$$E[r(w)] = CN^2\delta(w), \quad (\text{C.4})$$

$$E[i(w)] = 0 \quad \forall w. \quad (\text{C.5})$$

The variance of the real and imaginary parts are similarly computed. The autocorrelation of the laser speckle is approximated by a delta function plus a constant, due to assumed statistical independence and the second moment of the speckle also equal to a constant (e.g. $E[I_o^2] = B$),

$$E[I_o(u)I_o(v)] = C^2 + B\delta(u - v). \quad (\text{C.6})$$

The variance of the real and imaginary parts are computed to be:

$$\begin{aligned}
\text{var}[r(w_1, w_2)] &= \sum_{u=0}^{N-1} \sum_{v=0}^{N-1} E[I_o(u)I_o(v)] \cos\left(\frac{2\pi uw}{N}\right) \cos\left(\frac{2\pi vw}{N}\right) - C^2 N^4 \delta(w), \\
&= \begin{cases} BN^2 & \text{for } w_1 \in \{0, N/2\} \wedge w_2 \in \{0, N/2\}, \\ \frac{BN^2}{2} & \text{for } w_1 \in \{0, N/2\} \oplus w_2 \in \{0, N/2\}, \\ \frac{BN^2}{4} & \text{else;} \end{cases} \quad (\text{C.7})
\end{aligned}$$

$$\begin{aligned}
\text{var}[i(w_1, w_2)] &= \sum_{u=0}^{N-1} \sum_{v=0}^{N-1} E[I_o(u)I_o(v)] \sin\left(\frac{2\pi uw}{N}\right) \sin\left(\frac{2\pi vw}{N}\right), \\
&= \begin{cases} 0 & \text{for } w_1 \in \{0, N/2\} \vee w_2 \in \{0, N/2\}, \\ \frac{BN^2}{4} & \text{else.} \end{cases} \quad (\text{C.8})
\end{aligned}$$

Therefore, the variances of the real and imaginary parts are equal except for a small number of points in the image,

$$\text{var}[r(w)] = \text{var}[i(w)] \quad \forall w \ni \{0, N/2\}. \quad (\text{C.9})$$

Next, the correlation coefficient, ρ_{ri} , for the real and imaginary parts is computed to be zero everywhere due to orthogonality and are uncorrelated,

$$\begin{aligned}
\rho_{ri}(w) &= E[r(u)i(v)] = \sum_{u=0}^{N-1} \sum_{v=0}^{N-1} E[I_o(u)I_o(v)] \cos\left(\frac{2\pi uw}{N}\right) \sin\left(\frac{2\pi vw}{N}\right) \\
&= 0. \quad (\text{C.10})
\end{aligned}$$

Therefore, a majority of the Fourier transformed image points ($\forall w \ni \{0, N/2\}$) are jointly distributed as circular complex Gaussian random variables. After the DFT is taken on the laser speckle data, a second operation, magnitude squared, is performed to finalize the transformation from laser speckle to noisy autocorrelation

data. The magnitude squared operation transforms the circular complex Gaussian random variables to an intensity distribution. The intensity distribution of circular complex Gaussian random variables obey exponential statistics [17]. The mean of these exponential random variables is the autocorrelation of the true object as discussed in Section 3.2. The few pixels in the image where the imaginary part disappears is less than ten percent of the image. With the assumptions made above and ignoring the center pixel where the peak of the autocorrelation occurs, a single frame of noisy autocorrelation data can be well approximated as exponentially distributed random variables.

Appendix D. Single Channel, EM Phase Retrieval Algorithm

This appendix details the single channel, EM phase retrieval algorithm using Poisson statistics. The result is nearly identical to the ML algorithm presented by Schulz and Snyder [38] only differing by a scale factor. This algorithm is re-derived here for completeness and comparison to the multi-channel EM algorithms developed in Chapter IV.

The complete data, $\tilde{d}_k(y, x)$, is chosen such that it is related to the incomplete data, $d_k(x)$ by

$$d_k(x) = \sum_y \tilde{d}_k(y, x), \quad (\text{D.1})$$

where k denotes the data frame, x and y are two-dimensional spatial variables, and the complete data is assumed to be independent and identically distributed Poisson random variables. Knowing information about the observed, incomplete data, we choose the mean of the complete data to be

$$E[\tilde{d}_k(y, x)] = o(y)o(y + x). \quad (\text{D.2})$$

Because the complete data is chosen to be a Poisson random variable with a known mean, we can completely describe the probability mass function of the complete data.

$$P \left[\tilde{d}_k(y, x) \right] = \prod_k \prod_x \prod_y \frac{[o(y)o(y + x)]^{\tilde{d}_k(y, x)}}{\tilde{d}_k(y, x)!} \exp\{-o(y)o(y + x)\} \quad (\text{D.3})$$

The observed incomplete data is described by its mean

$$\begin{aligned}
E[d_k(x)] &= \sum_y E[\tilde{d}_k(y, x)] \\
&= \sum_y o(y)o(y+x)
\end{aligned} \tag{D.4}$$

The log-likelihood function of the complete data, L_{cd} , is found by taking the natural log of the probability mass function in Eqn. D.3.

$$L_{cd}(o) = \sum_k \sum_x \sum_y \left\{ \tilde{d}_k(y, x) \log [o(y)o(y+x)] - o(y)o(y+x) + \text{A.T.} \right\} \tag{D.5}$$

Expectation Step. The expectation step of the EM algorithm is defined as the expectation of the complete data log-likelihood function conditioned on the old object estimate (from the previous iteration), $o^{\text{old}}(y)$, and the incomplete data, $d_k(x)$.

$$\begin{aligned}
Q &\stackrel{\text{def}}{=} E[L_{cd} \mid o^{\text{old}}, d_k(x)] \\
&= \sum_k \sum_y \sum_x \left\{ E^{\text{old}}[\tilde{d}_k(y, x)] \log [o(y)o(y+x)] - o(y)o(y+x) + \text{A.T.} \right\}
\end{aligned} \tag{D.6}$$

where E^{old} is the conditional expectation conditioned on the old estimates of o and the incomplete data. K is the total number of frames and A.T. denotes another term not a function of o .

For Poisson statistics, the conditional expectation on the complete data given the incomplete data is detailed by Shepp and Vardi [42]:

$$\begin{aligned}\mu(y_0, x) &\stackrel{\text{def}}{=} E^{\text{old}}[\tilde{d}_k(y_0, x)] \\ &= \frac{o^{\text{old}}(y_0)o^{\text{old}}(y_0 + x)d_k(x)}{\sum_y o^{\text{old}}(y)o^{\text{old}}(y + x)}.\end{aligned}\tag{D.7}$$

Maximization Step. The maximization step involves maximizing the Q function with respect to the unknown parameter, o . We take the partial derivative of $Q(o|o^{\text{old}})$, set it equal to zero and solve for the object, o .

$$\begin{aligned}\frac{\partial Q(o|o^{\text{old}})}{\partial o(y_0)} &= \frac{\partial}{\partial o(y_0)} \sum_k \sum_x \sum_y \left\{ \mu(y, x) \log[o(y)o(y + x)] - o(y)o(y + x) \right\} \\ &= \sum_k \sum_x \sum_y \left\{ \mu(y, x) \frac{\partial}{\partial o(y_0)} \log[o(y)o(y + x)] - \frac{\partial}{\partial o(y_0)} o(y)o(y + x) \right\} \\ &= \sum_k \sum_x \left\{ \frac{\mu(y_0, x)}{o(y_0)} + \frac{\mu(y_0 - x, x)}{o(y_0)} - [o(y_0 + x) + o(y_0 - x)] \right\} \\ &= \frac{1}{o(y_0)} \sum_k \sum_x \left\{ \mu(y_0, x) + \mu(y_0 - x, x) \right\} - 2K S_o^{\text{new}}\end{aligned}\tag{D.8}$$

where S_o^{new} is the sum of the new object estimate defined as

$$S_o^{\text{new}} = \sum_x o^{\text{new}}(x).\tag{D.9}$$

Setting Eqn. D.8 equal to zero and solving for the object, o , yields

$$o^{\text{new}}(y_0) = \frac{1}{2K S_o^{\text{new}}} \sum_k \sum_x \left\{ \mu(y_0, x) + \mu(y_0 - x, x) \right\}.\tag{D.10}$$

In order to simplify this expression, a few new terms will be defined. We will let the average of the incomplete data be defined as the measured autocorrelation, \tilde{R}_o ,

$$\tilde{R}_o(x) = \frac{1}{K} \sum_{k=1}^K d_k(x). \quad (\text{D.11})$$

The autocorrelation of the old object estimate from the previous iteration will be defined as

$$R_o^{\text{old}}(x) = \sum_y o^{\text{old}}(y) o^{\text{old}}(y+x). \quad (\text{D.12})$$

Also, we will define the following parameter

$$\begin{aligned} \Psi(y_0) &\stackrel{\text{def}}{=} \frac{1}{K} \sum_k \sum_x \left\{ \mu(y_0, x) + \mu(y_0 - x, x) \right\} \\ &= \frac{1}{K} \sum_k \sum_x \left\{ \frac{o^{\text{old}}(y_0) o^{\text{old}}(y_0 + x) d_k(x)}{\sum_y o^{\text{old}}(y) o^{\text{old}}(y+x)} + \frac{o^{\text{old}}(y_0) o^{\text{old}}(y_0 - x) d_k(x)}{\sum_y o^{\text{old}}(y) o^{\text{old}}(y+x)} \right\} \\ &= o^{\text{old}} \cdot \left[o^{\text{old}} \star \frac{\tilde{R}_o}{R_o^{\text{old}}} + o^{\text{old}} \star \frac{\tilde{R}_o}{R_o^{\text{old}}} \right](y_0) \end{aligned} \quad (\text{D.13})$$

Substituting these parameters back into the expression for the object estimate produces the following equation.

$$o^{\text{new}}(y_0) = \frac{\Psi(y_0)}{2S_o^{\text{new}}} \quad (\text{D.14})$$

Here, the expression for the new object estimate, o^{new} , is a function of the old object estimate, o^{old} , and the incomplete data. Summing both sides of Eqn. D.14 provides an expression for S_o^{new}

$$S_o^{\text{new}} = \sqrt{\frac{1}{2} \sum_{y_0} \Psi(y_0)} \quad (\text{D.15})$$

The iterative solution restated is

$$o^{\text{new}}(y_0) = \frac{o^{\text{old}}}{2S_o^{\text{new}}} \cdot \left[o^{\text{old}} \star \frac{\tilde{R}_o}{R_o^{\text{old}}} + o^{\text{old}} * \frac{\tilde{R}_o}{R_o^{\text{old}}} \right] (y_0). \quad (\text{D.16})$$

This result, is identical to the original Schulz and Snyder ML algorithm [38] differing only by a scaling parameter, S_o^{new} . The Schulz and Snyder ML algorithm uses the S_o^{old} scale parameter. The Schulz and Snyder ML algorithm is detailed in Eqn. D.17.

$$o^{\text{new}}(y_0) = \frac{o^{\text{old}}}{2S_o^{\text{old}}} \cdot \left[o^{\text{old}} \star \frac{\tilde{R}_o}{R_o^{\text{old}}} + o^{\text{old}} * \frac{\tilde{R}_o}{R_o^{\text{old}}} \right] (y_0) \quad (\text{D.17})$$

Bibliography

1. Andrews, Larry C. and Ronald L. Phillips. *Laser Beam Propagation through Random Media*. SPIE, Bellingham, 2nd edition, 2005.
2. Cain, S., M. Hayat, and E. Armstrong. “An Efficient Projection Based Technique for Registering Images in the Presence of Fixed Pattern Noise”. *IEEE Trans. Image Processing*, 10(12):1860–1872, December 2001.
3. Cain, Stephen C. “Joint Blind Deconvolution and Image Correlography via a Bayesian Image Reconstruction Algorithm”. *IEEE Aerospace Conference Proceedings*, 2006.
4. Cain, Stephen C. “Instructor Notes”. Air Force Institute of Technology, 2008.
5. Cederquist, J. N. and C. C. Wackerman. “Phase-Retrieval Error: A Lower Bound”. *J. Opt. Soc. Am. A*, 4(9):1788–1792, September 1987.
6. Dainty, J. C. “Introduction”. J. C. Dainty (editor), *Laser Speckle and Related Phenomena*, volume 9 of *Topics in Applied Physics*. Springer-Verlag, 1975.
7. Dainty, J. C. and James R. Fienup. “Phase Retrieval and Image Reconstruction for Astronomy”. Henry Stark (editor), *Image Recovery: Theory and Application*. Academic Press, 1987.
8. den Dekker, A. J. and A. van den Bos. “Resolution: A Survey”. *J. Opt. Soc. Am. A*, 14(3):547–557, March 1997.
9. Dempster, A. P., N. M. Laird, and D. B. Rubin. “Maximum Likelihood From Incomplete Data Via the EM Algorithm”. *J.R. Stat. Soc. B*, 39(1), 1977.
10. Elbaum, M., M. King, and M. Greenebaum. *Laser Correlography: Transmission of High-Resolution Object Signatures Through the Turbulent Atmosphere*. Technical Report ADA013424, Riverside Research Institute, New York, Oct 1974.
11. Fienup, James R. “Reconstruction of an Object From the Modulus of its Fourier Transform”. *Optics Letters*, 3(1):27–29, 1978.
12. Fienup, James R. “Phase Retrieval Algorithms: A Comparison”. *Applied Optics*, 21(15):2758–2769, August 1982.
13. Fienup, James R. “Image Formation from Nonimaged Laser Speckle Patterns”. S. R. Robinson (editor), *The Infrared and Electro-Optical Systems Handbook*, volume 8. Environmental Research Institute of Michigan, 1993.
14. Fienup, James R. and Paul S. Idell. “Imaging Correlography with Sparse Arrays of Detectors”. *Optical Engineering*, 27(9):778–784, September 1988.
15. Gerchberg, R. W. and W. O. Saxton. “A Practical Algorithm for the Determination of Phase from Image and Diffraction Plane Pictures”. *Optik*, 35(2):237–246, 1972.

16. Goodman, Joseph W. “Statistical Properties of Laser Speckle Patterns”. J. C. Dainty (editor), *Laser Speckle and Related Phenomena*, volume 9 of *Topics in Applied Physics*. Springer-Verlag, 1975.
17. Goodman, Joseph W. *Statistical Optics*. John Wiley and Sons, New York, 2000.
18. Goodman, Joseph W. *Introduction to Fourier Optics*. Roberts & Co., Englewood, CO, 3rd edition, 2005.
19. Goodman, Joseph W. *Speckle Phenomena in Optics: Theory and Applications*. Roberts & Co., Englewood, CO, 2007.
20. Guizar-Sciarios, Manuel and James R. Fienup. “Phase Retrieval with Fourier-Weighted Projections”. *J. Opt. Soc. Am. A.*, 25(3):701–709, March 2008.
21. Hayes, Monson H. “The Unique Reconstruction of Multidimensional Sequences from Fourier Transform Magnitude or Phase”. Henry Stark (editor), *Image Recovery: Theory and Application*. Academic Press, 1987.
22. Hecht, Eugene. *Optics*. Addison Wesley, San Fransisco, 4th edition, 2002.
23. Holmes, R.B., K. Hughes, P. Fairchild, B. Spivey, and A. Smith. “Description and Simulation of an Active Imaging Technique Utilizing Two Speckle Fields: Iterative Reconstructors”. *J. Opt. Soc. Am. A.*, 19(3):458–471, March 2002.
24. Holmes, R.B., K. Hughes, P. Fairchild, B. Spivey, and A. Smith. “Description and Simulation of an Active Imaging Technique Utilizing Two Speckle Fields: Root Reconstructors”. *J. Opt. Soc. Am. A.*, 19(3):444–457, March 2002.
25. Idell, Paul S., James R. Fienup, and Ron S. Goodman. “Image Synthesis From Nonimaged Laser-Speckled Patterns”. *Optics Letters*, 12(11):858–860, November 1987.
26. James, S. P. *Blind Deconvolution Through Polarization Diversity of Long Exposure Imagery*. Master’s thesis, Air Force Institute of Technology, 2009.
27. Kehler, Gen C. Robert. “Air Force Association Speech”. <http://www.afspc.af.mil/library/speeches/speech.asp?id=356>, November 2007.
28. LeMaster, D. A. and S. C. Cain. “Multichannel Blind Deconvolution of Polarimetric Imagery”. *J. Opt. Soc. Am. A.*, 25(9):2170–2176, September 2008.
29. Lucy, L. B. “An Iterative Technique for the Rectification of Observed Distributions”. *Astronomical Journal*, 79(6):745754, June 1974.
30. Moon, Todd K. “The Expectation-Maximization Algorithm”. *IEEE Signal Processing Magazine*, 13(6):47–60, November 1996.
31. Phillips, James D. *Joint Image and Pupil Plane Reconstruction Algorithm based on Bayesian Techniques*. Ph.D. dissertation, Air Force Institute of Technology, Wright Patterson Air Force Base, Ohio, March 2008.

32. Phillips, James D. and Stephen C. Cain. “Image Synthesis From a Series of Coherent Frames of Pupil Intensity”. *Proc. of SPIE*, 6712(7), 2007.
33. Phillips, James D. and Stephen C. Cain. “Joint Maximum Likelihood Estimator From Pupil and Image Plane Data”. *Optical Engineering*, 47(2), February 2008.
34. Richardson, William Hadley. “Bayesian-Based Iterative Method of Image Restoration”. *J. Opt. Soc. Am.*, 62(1):55–59, January 1972.
35. Roggemann, Michael C. and Byron M. Welsh. *Imaging Through Turbulence*. CRC Press, Boca Raton, 1996.
36. Scharf, Louis L. *Statistical Signal Processing: Detection, Estimation, and Time Series Analysis*. Addison Wesley, 1991.
37. Schulz, Timothy J. “Multiframe Blind Deconvolution of Astronomical Images”. *Journal of the Optical Society of America A*, 10(5):1064–1073, 1993.
38. Schulz, Timothy J. and Donald L. Snyder. “Image Recovery From Correlations”. *J. Opt. Soc. Am. A.*, 9(8):1266–1272, August 1992.
39. Schulz, Timothy J. and David G. Voelz. “Signal Recovery from Autocorrelation and Cross-Correlation Data”. *J. Opt. Soc. Am. A.*, 22(4):616–624, April 2005.
40. Seldin, J.H. and James R. Fienup. “Iterative Blind Deconvolution Algorithm Applied to Phase Retrieval”. *J. Opt. Soc. Am. A.*, 7(3):428–433, March 1990.
41. Shahram, M. and P. Milanfar. “Imaging Below the Diffraction Limit: A Statistical Analysis”. *IEEE Trans Image Proc.*, 13(5):677–689, May 2004.
42. Shepp, L. A. and Y. Vardi. “Maximum Likelihood Reconstruction For Emission Tomography”. *IEEE Trans. Med. Imaging*, 1(2):113–122, October 1982.
43. Strong, David M. *Polarimeter Blind Deconvolution Using Image Diversity*. Ph.D. thesis, Air Force Institute of Technology, Wright Patterson Air Force Base, Ohio, September 2007.
44. Voelz, David G., John D. Gonglewski, and Paul S. Idell. “Image Synthesis From Nonimaged Laser-Speckle Patterns: Comparison of Theory, Computer Simulation, and Laboratory Results”. *Applied Optics*, 30(23):3333–3344, August 1991.
45. Wu, C. F. “On the Convergence Properties of the EM Algorithm”. *Ann.Statist.*, 11(1):95–103, 1983.

REPORT DOCUMENTATION PAGE

Form Approved
OMB No. 0704-0188

The public reporting burden for this collection of information is estimated to average 1 hour per response, including the time for reviewing instructions, searching existing data sources, gathering and maintaining the data needed, and completing and reviewing the collection of information. Send comments regarding this burden estimate or any other aspect of this collection of information, including suggestions for reducing this burden to Department of Defense, Washington Headquarters Services, Directorate for Information Operations and Reports (0704-0188), 1215 Jefferson Davis Highway, Suite 1204, Arlington, VA 22202-4302. Respondents should be aware that notwithstanding any other provision of law, no person shall be subject to any penalty for failing to comply with a collection of information if it does not display a currently valid OMB control number. **PLEASE DO NOT RETURN YOUR FORM TO THE ABOVE ADDRESS.**

1. REPORT DATE (DD-MM-YYYY) 03-09-2010	2. REPORT TYPE Doctoral Dissertation	3. DATES COVERED (From — To) September 2007-September 2010
--	--	--

4. TITLE AND SUBTITLE Statistical Image Recovery From Laser Speckle Patterns With Polarization Diversity	5a. CONTRACT NUMBER 5b. GRANT NUMBER 5c. PROGRAM ELEMENT NUMBER
---	--

6. AUTHOR(S) Dixon, Donald B., Lieutenant Colonel, USAF	5d. PROJECT NUMBER N/A 5e. TASK NUMBER 5f. WORK UNIT NUMBER
---	---

7. PERFORMING ORGANIZATION NAME(S) AND ADDRESS(ES) Air Force Institute of Technology Graduate School of Engineering and Management (AFIT/EN) 2950 Hobson Way WPAFB OH 45433-7765 DSN: 785-3636	8. PERFORMING ORGANIZATION REPORT NUMBER AFIT/DEO/ENG/10-11
---	---

9. SPONSORING / MONITORING AGENCY NAME(S) AND ADDRESS(ES) Air Force Research Laboratory AFRL/RDSA Attn: Dr. Victor Gamiz 3550 Aberdeen Ave SE Kirtland AFB NM 87117-5776 (505) 846-4846 Victor.Gamiz@Kirtland.af.mil	10. SPONSOR/MONITOR'S ACRONYM(S) AFRL/RDSA 11. SPONSOR/MONITOR'S REPORT NUMBER(S)
---	---

12. DISTRIBUTION / AVAILABILITY STATEMENT

APPROVED FOR PUBLIC RELEASE; DISTRIBUTION UNLIMITED

13. SUPPLEMENTARY NOTES

14. ABSTRACT

This research extends the theory and understanding of the laser speckle imaging technique. This non-traditional imaging technique may be employed to improve space situational awareness and image deep space objects from a ground-based sensor system. The use of this technique is motivated by the ability to overcome aperture size limitations and the distortion effects from Earth's atmosphere. Laser speckle imaging is a lensless, coherent method for forming two-dimensional images from their autocorrelation functions. Phase retrieval from autocorrelation data is an ill-posed problem where multiple solutions exist. This research introduces polarization diversity as a method for obtaining additional information so the structure of the object being reconstructed can be improved. Results show that in some cases the images restored using polarization diversity are superior to those reconstructed without it.

15. SUBJECT TERMS

polarization, phase-retrieval, EM algorithm, image recovery, laser speckle, statistical optics

16. SECURITY CLASSIFICATION OF:			17. LIMITATION OF ABSTRACT	18. NUMBER OF PAGES	19a. NAME OF RESPONSIBLE PERSON
a. REPORT	b. ABSTRACT	c. THIS PAGE			Dr. Stephen C. Cain (ENG)
U	U	U	UU	153	19b. TELEPHONE NUMBER (include area code) (937)255-3636, ext 4716; email:Stephen.Cain@afit.edu